A MULTI-SCALE TOOLBOX TO PREDICT STRUCTURE AND FUNCTION OF POLYSACCHARIDES AGGREGATES

vorgelegt von
Master of Science (M.Sc.)
Ankush Singhal

an der Fakultät II - Mathematik und Naturwissenschaften
der Technischen Universität Berlin
zur Erlangung des akademischen Grades

Doktor der Naturwissenschaften
Dr. rer. nat.

genehmigte Dissertation

Promotionsausschuss:

Vorsitzender: Prof. Dr. Michael Lehmann
Gutachterin: Dr. Andrea Grafmüller
Gutachterin: Prof. Dr. Sabina Klapp
Gutachterin: Prof. Dr. Maria Andrea Mroginski
Tag der wissenschaftlichen Aussprache: 18th February 2020

Berlin 2020

Abstract

Carbohydrates are class of biomolecules- their functions and properties covers a vast field that still needs to be explored. Many biological polysaccaharides form aggregates and their structures and properties are very versatile and depends on the aggregate structure and molecular interactions. Natural polysaccahrides can also form hydrogels, porous network of polymers, that can take up a high percentage of water. Their properties can be additionally tuned by the introductions of chemical modifications to a fraction of monomers. To make efficient use of their versatile properties, understanding the relation between the molecular structure and interactions of polysaccahrides and the properties of the aggregates formed is essential.

Computational modeling provides an efficient tool for understanding interactions at the molecular level, thus providing a qualitative direction for future experiments. Hence modeling offers a cost and time efficient method for their study. In this thesis, the aggregates and structures formed by different glucose and chitosan oligomers were simulated and the resulting solution or aggregates structures are characterized using all-atom and coarse-grained molecular dynamics. Usually, polymers have slow dynamics making all-atom simulation computationally inefficient. Therefore a coarse-grained model was developed to study the properties of the polysaccahrides at the required length and time scale.

Chitosan hydrogels with various hydrophobic modification were modeled. The transferability of short oligomers with respect to different water concentration, degree of polymerization and modification was explicitly established. Different morphological network structures of longer polymer were obtained corresponding to different degree, type, and pattern of modification. In particular, different morphological transition from a uniform polymer network to a structure containing dense hydrophobic cluster and large pores was found for certain conditions.

Finally, one of the principle applications of the chitosan hydrogel as a drug carrier was explored. The molecules Doxorubicin(DOX) and Gemicitabine(GEM) were chosen

as model drugs and their interactions with the different modified chitosan polymers have been thoroughly studied at all-atom and coarse-grained resolution. The diffusion of DOX and GEM through the different network morphologies formed by the hydrophobically-modified chitosan was found to show quite different, network dependent trends. Whereas GEM migrates through all chitosan hydrogels freely irrespective of type and degree of modification. Placing the drugs together in the networks affects the diffusion behavior of both. The results demonstrate the potential of this computational tool in the systematic development of drug-loaded hydrogels for pharmaceutical applications.

Zusammenfassung

Kohlenhydrate sind eine klasse von biomolekülen- ihre funktionen und eigenschaften umfassen ein weites feld, das noch nicht erforscht ist. Viele biologische polysaccaharide bilden aggregate und ihre strukturen und eigenschaften sind sehr vielseitig und hängen von der aggregatstruktur und den molekularen wechselwirkungen ab. Natürliche polysaccharide können auch hydrogele bilden, ein poröses netzwerk von polymeren, die einen hohen anteil an wasser aufnehmen können. Ihre eigenschaften können durch die einführung chemischer modifikationen an einem bruchteil der monomere zusätzlich optimiert werden. Um ihre vielseitigen eigenschaften effizient nutzen zu können, ist es unerlässlich, den zusammenhang zwischen der molekularstruktur und den wechselwirkungen von polysaccahriden und den eigenschaften der gebildeten aggregate zu verstehen.

Die rechnergestützte modellierung stellt ein effizientes werkzeug zum verständnis von wechselwirkungen auf molekularer ebene dar und liefert so eine qualitative orientierung für zukünftige experimente. Daher bietet die modellierung eine kosten- und zeiteffiziente methode für ihre Studie. In dieser arbeit wurden die aggregate und strukturen, die aus verschiedenen glukose- und chitosanoligomeren gebildet wurden, simuliert und die resultierenden lösungs- oder aggregatstrukturen werden durch eine vollatomige und grobkörnige molekulardynamik charakterisiert. Normalerweise weisen polymere eine langsame dynamik auf, was die simulation von atomen ineffizient macht. Daher wurde ein grobkörniges modell entwickelt, um die eigenschaften der polysaccharide in der erforderlichen länge und Zeit zu untersuchen maßstab.

Chitosan-hydrogele mit verschiedenen hydrophoben modifikationen wurden modelliert. Die ubertragbarkeit von kurzen oligomeren in bezug auf unterschiedliche wasserkonzentration, polymerisationsgrad und modifikation wurde explizit festgelegt. Verschiedene morphologische netzwerkstrukturen aus längerem polymer wurden erhalten, die unterschiedlichem grad, typ und muster der modifikation entsprechen. Insbesondere wurde unter bestimmten bedingungen ein unterschiedlicher morphologischer ubergang von einem einheitlichen polymernetzwerk zu einer Struktur mit dichtem hydrophoben cluster und

großen poren gefunden.

Schließlich wurde eine der hauptanwendungen des chitosan-hydrogels als wirkstoffträger untersucht. Die moleküle Doxorubicin(DOX) und Gemicitabin(GEM) wurden als modellmedikamente ausgewählt und ihre wechselwirkungen mit den verschiedenen modifizierten chitosanpolymeren wurden gründlich in atomarer und grobkörniger auflösung untersucht. Die diffusion von DOX und GEM durch die verschiedenen netzwerkmorphologien des hydrophob modifizierten chitosans zeigte ganz unterschiedliche, netzwerkabhängige Trends. Während GEM durch alle chitosan-hydrogele frei wandert, unabhängig von Art und Grad der modifikation. Das zusammenstellen der medikamente in den netzwerken beeinflusst das Diffusionsverhalten beider. Die ergebnisse zeigen das potenzial dieses rechenwerkzeugs für die systematische entwicklung von medikamentenbeladenen hydrogelen für pharmazeutische anwendungen.

Declaration

I declare that this thesis is an original report of my research, has been written by me and has not been submitted for any previous degree. I confirm that the work submitted is my own, except where work which has formed part of jointly-authored publications has been included. My contribution and those of the other authors to this work have been explicitly indicated below. I confirm that appropriate credit has been given within this thesis where reference has been made to the work of others.

The work presented in Chapter 2 was previously published in **Systematic hydrogen bond manipulations to establish polysaccharide structure-property correlations** published in *Angewandte Chemie* and a manuscript **Multi-scale modelling study of self-assembly of cellulose based derivatives** under preparation.

The work presented in Chapter 3 to 5 was previously published in **Tailoring the Chemical Modification of Chitosan Hydrogels to Fine Tune the Release of a Synergistic Combination of Chemotherapeutics** in *ACS Biomacromolecules* and a manuscript **Predicting Chitosan Hydrogel Properties with Multiscale Coarse-Grained Simulations** is about to be submitted in *Soft Matter*.

Ankush Singhal
Potsdam, 04 December 2019

Contents

Chapter 1

Introduction

1.1 Carbohydrates

Carbohydrates are a class of biologically significant compounds consisting of chemically bonded carbon, hydrogen, and oxygen, that, together with lipids, proteins and nucleic acids, belong to the fundamental building blocks of living systems. Their biological functions reach from structural stability[1] and energy storage[2,3] to cell communication[4,5] and interactions with bacteria and viruses. Some major examples of carbohydrates include sugar (glucose), starch[6] and cellulose[6] . Based on the number of sugar units, carbohydrates can be classified into sub-categories, namely mono-, di-, oligo- and polysaccharides. Polysaccharides are the most abundant organic matter on the earth. These have applications in textile manufacture[7] , food[8] , paper[9] and pharmaceutical industry[10] .

Despite their versatile biological functions, carbohydrates remain the least studied and understood class of biomolecules, owing to their complexity and a lack of appropriate experimental methods to study them systematically.

The basic building blocks of polysaccharides are monosaccharides, as the examples shown in Figure 1.1 a) and b). Most biologically relevant monosaccharides are pentoses or hexoses, containing five or six carbon atoms, respectively. They form rings in which the carbon atoms are typically labeled C1-C6 starting from the ring oxygen and counting in the clockwise direction. Monosaccharides can be classified as two stereoisomers, namely Levorotatory(L) and Dextrorotatory(D). They basically used to describe the rotation of plane polarized light around the chiral center. Each asymmetric carbon, e.g. linked to an OH group, is a chiral center. Based on the conformation of the -OH group

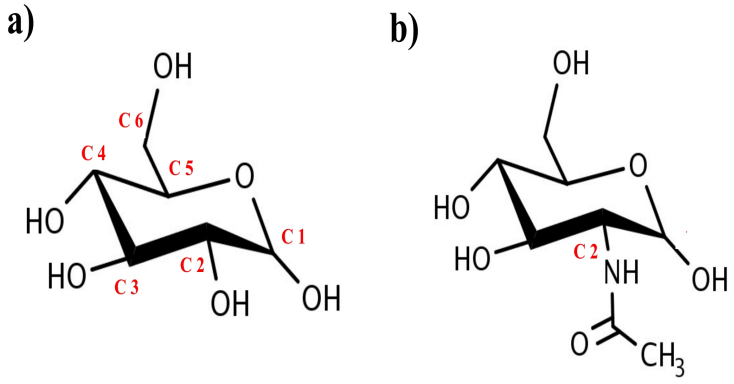

Figure 1.1: Chemical structures of (a). β-D- glucose, (b). β-D-Acetyl-glucosamine

attached to the anomeric carbon(C1) are defines the α or β forms of glucose. Here, α correspond to equitorial position of -OH with respect to ring oxygen while -OH will be in an axial position in β form. In Figure 1.1, β forms of glucose and N-acetyl-glucosamine are shown.

Monosaccharides can be connected to form polymers by glycosidic bonds, covalent bonds that form between the anomeric carbon and any hydroxyl group of the next monomer. Due to the many possible configurations, the resulting molecular structures range from linear to highly branched and from oligomers consisting of a few monomers to polysaccharides with a degree of polymerization (DP) of several thousand. In addition, the -OH groups can be chemically modified both in nature or artificially. Several modification such as methyl[11] , fluorine[11] , acetyl, etc. can be introduced to alter their chemical properties.

The conformational parameters of the carbohydrates depend on their possibilities to form intra-molecular hydrogen bonds between adjacent monomers, as shown in Figure 1.2. In addition, many possibilities of forming inter-molecular hydrogen bonds between polymer chains shown in Figure 1.2 leads to the formation of diverse aggregate structures. Their flexibility, as well as the DP and monomer sequences of these molecules also contribute to determine their solubility.

1.1.1 Polysaccharides: Cellulose and chitosan

Natural polysaccharides form the basis of many biomaterials. The two most abundant polysaccharides are cellulose and chitin. Cellulose is a polysaccharide consisting of lin-

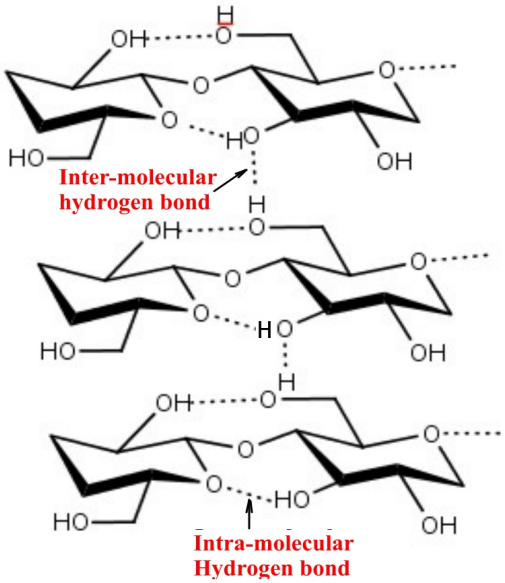

Figure 1.2: Intra- and inter- molecular hydrogen bonds between adjacent monomer and polymer chains

ear chains of β(1-4) linked D-glucose units as shown in Figure 1.1a). It is an important structural component of the primary cell wall of green plants, and many forms of algae. Cellulose can reach a DP up to 15000[12] . The many -OH groups present on the cellulose polymers can make multiple inter-polymer hydrogen bonds between different polymer chains as shown in Figure 1.2, forming crystalline microfibrils. The insolubility of cellulose results from this dense network of inter-molecular hydrogen bonds, as well the stiffness of the molecules produced by intra-molecular hydrogen bonds between the ring oxygen (O5) and the -OH group at the C3 carbon. Altering the chemical constitution of cellulose can alter the physical properties of the resulting network. Specific derivatives can be designed that disrupt hydrogen bond networks and alter the physical properties such as enhancing or decreasing the water solubility or change in ionic character[13] .

Chitin is a polymer very similar to cellulose composed of β(1-4) linked N-acetyl glucosamine as monomeric unit (as shown in Figure 1.1b). It has a similar structure to cellulose with the hydroxyl group at the C2 carbon on each monomer replaced with an acetyl amine group as shown in Figure 1.1b). The presence of the acetyl groups increases the hydrogen bonding between the polymer chains further compared to that of the hydroxyl groups. This result in the formation strong chitin polymer fibrils.

The N-acetylglucosamine monomers can be deacetylated chemically, to produce chitosan. As a result, chitosan is composed of a random sequence of β-(1,4) linked glu-

cosamine(GlcN) and N-acetyl glucosamine(GlcNAc) monomers. GlcN comprises a primary amine group which can be protonated at pH value lower than its pKa. This results in an electrostatic repulsion between the monomers, rendering chitosan chains to be soluble. The primary amine group also provides a site for chemical modifications as well. The presence of the N-acetyl group in GlcNAc, on the otherhand allow hydrophobic and hydrogen bond interactions, leading to self-association between the monomers. As a result, the self-assembly of chitosan primarily depends on the pH[14,15] and the degree of acetylation(DA)[16,17] of the polymer. It had been suggested that with protonation more than 75%, chitosan behaves as a poly-electrolyte, as chains have minimal association due to high charge density. While chains with protonation below 50% or a DA of more than 50% behave as hydrophobic polymer with only isolated positive charges. Neutral chitosan polymers form different aggregate structures with varying hydrophobic modifications. These varying chitosan hydrogel has been useful in various application like water purification[18] , oil spill remediation[17] , wound healing[19] and drug delivery[20,21] .

1.2 Hydrogels

Hydrogels are highly porous networks of polymers that can contain as much as around 99 wt% water. The chemical and physical properties of the hydrogels can be modified by chemically changing the constituents of the monomers, or the chemical nature and amount of linker holding the polymers together. Due to their flexible micro structure, they become a suitable candidate for drug delivery module[20,21,22,23] . Further, the loading and release rates of drugs in and out of hydrogels are mostly governed by diffusion, which depends on the molecular interactions between the polymer chains and the drugs, as well as the network morphology. These features have been harnessed for tuning the release kinetics and the scheduling of drugs, especially through chemical modification of the polymer backbone. Due to its many desirable properties, chitosan has received a lot of attention for potential applications as pharmaceutical hydrogel. With proper modifications of chitosan can be used to alter the absorption, diffusion and the release of small molecules from its hydrogels[20,21] .

Theoretical and computational models provide a method to explore the system parameters of such hydrogels on a large scale, while being comparatively cost effective. Some of the methods that have been applied to predict structure and interactions of polysaccharide assemblies and hydrogels are introduced in the next sections.

1.3 Molecular simulation

Molecular simulations provide essential tools to understand macromolecular structure based on the molecular interactions. Simulations can be regarded as in-silico experiments performed on the molecules. These computer based experiments can provide details about the conformations and interactions of the molecules and the physical and chemical properties of their aggregates.

At the most detailed level, quantum mechanics (QM) provides the most accurate and fundamental description of matter. However, QM simulations can only be run for at most few hundred atoms. Often systems need to be treated on larger length and longer times scales than QM methods can achieve. On these scales, the fluctuations of the electronic degrees of freedom play only a minor role. At even larger scales, the same can be said for the motion of individual atoms. Many modeling approaches to study a system on the required length and time scales have been developed, as shown in Figure 1.3.

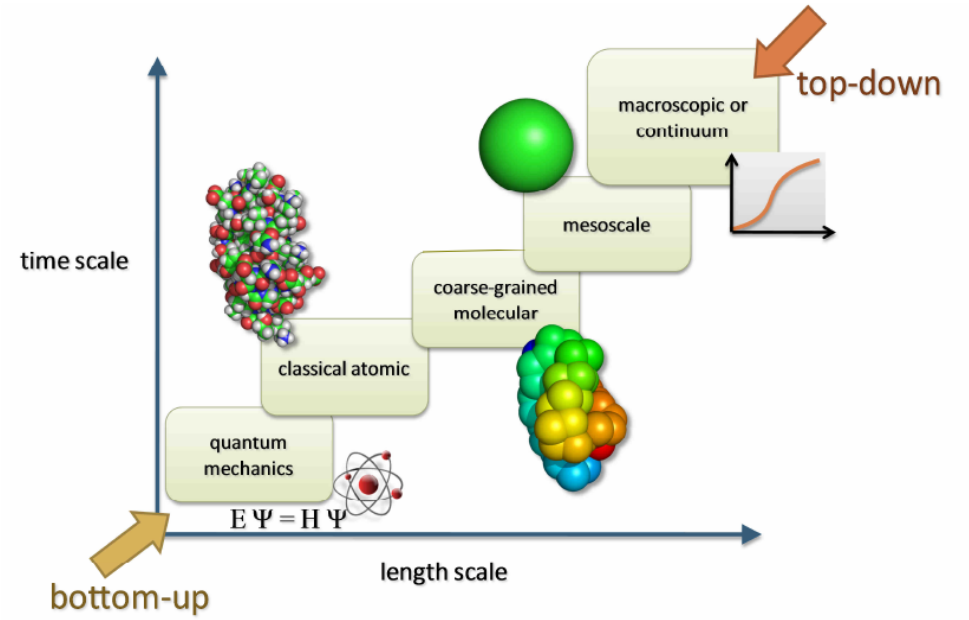

Figure 1.3: Different approaches to study the molecular systems with various resolution depending on the properties of interest. In a bottom-up model development, coarser resolution simulations are guided by detailed level studies like quantum mechanics. In top-down approaches, macroscopic properties are used to guide finer-resolution simulations like classical atomic or coarse grained molecular simulations.

The resolution required depends on the properties of interest and on the type of phenomenon that needs to be analyzed. All-atom molecular dynamics(MD) and coarse grained (CG)modeling are two such resolution as shown in Figure 1.4 for the solution of $GlcNH_2$ monomers. These models will be discussed in the next sections.

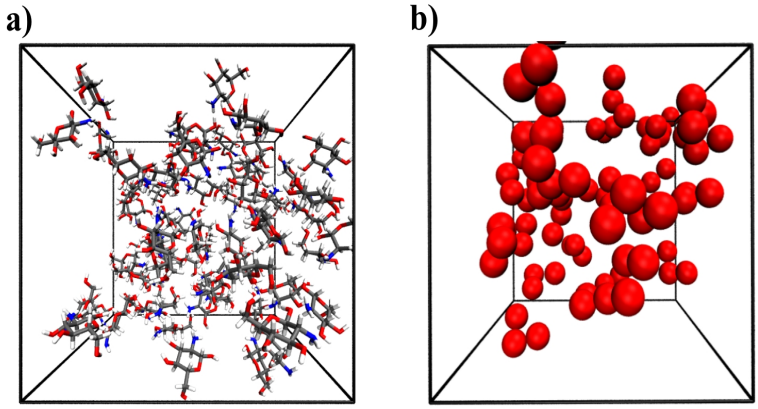

Figure 1.4: Atomistic representation of (a) β-D-glucosamine solution and the corresponding (b) coarse-grained representation.

1.3.1 Molecular dynamics

MD is a technique used to describe the positions and velocities of the molecules in the system based on the Newton's equations of motion as shown in Eq 1.2.

$$m_i \ddot{r}_i = f_i \tag{1.1}$$

$$f_i = -\frac{\partial \mathcal{U}}{\partial r_i} \tag{1.2}$$

Here, m_i and r_i are the mass and position of atom i. To study the evolution of the system with time, we need to calculate the forces f_i acting on atom i. The forces are usually described by a potential energy $\mathcal{U}(r^N)$, where $r^N = (r_1, r_2, ...r_N)$ represents the complete set of atomic coordinates.

$\mathcal{U}(r^N)$ is usually described by a set of interaction functions and corresponding parameters that is referred to as a force-field. Force-field functions and parameter sets are derived from both experimental data and high-level quantum mechanical calculations. Force-fields can be based on different parametrization principles and are specialized for different applications and give varied results[24,25] .

Typically $\mathcal{U}(r^N)$ is decomposed into bonded terms, relating atoms that are linked by covalent bonds and non-bonded (also called "non-covalent") terms, describing the long-range electrostatic and van der Waals forces. A general form for the total energy in an additive force field can be written as $\mathcal{U}_{total} = \mathcal{U}_{bonded} + \mathcal{U}_{non-bonded}$.

The non-bonded terms are computationally more costly, as they include many more interactions per atom. The non-bonded interaction are most commonly given by the Lennard-Jones potential ($\mathcal{U}_{LJ}$) and the Coulomb potential ($\mathcal{U}_{coloumb}$). The components of the non-bonded contributions are given by the following summations, $\mathcal{U}_{non-bonded} = \mathcal{U}_{LJ} + \mathcal{U}_{coulomb}$.

$$\mathcal{U}_{LJ}(r_{ij}) = 4\epsilon_{ij}\left[\left(\frac{\sigma_{ij}}{r_{ij}}\right)^{12} - \left(\frac{\sigma_{ij}}{r_{ij}}\right)^{6}\right] \tag{1.3}$$

Both, σ_{ij} and ϵ_{ij} in Eq 1.3 correspond to the equilibrium separation of two atoms i, j and the depth of the energy minimum and $r_{ij} = \mid \vec{r_i} - \vec{r_j} \mid$ is the distance between the two atoms.

The coulomb interaction between charges or partial charges on the atoms is expressed as:

$$\mathcal{U}_{coulomb}(r_{ij}) = \frac{q_i q_j}{4\pi\epsilon_o r_{ij}} \tag{1.4}$$

where, the q_i, q_j are the charges and ϵ_o is the permittivity of the free space.

The bonded potential typically comprises bond, angle, dihedral and improper dihedral as shown in Figure 1.5. The components of the covalent contributions are given by the summations: $\mathcal{U}_{bonded} = \mathcal{U}_{bond} + \mathcal{U}_{angle} + \mathcal{U}_{dihedral} + \mathcal{U}_{improper}$.

Typically, a covalent bond between two atoms is modeled as harmonic potential and expressed as,

$$\mathcal{U}_b(r_{ij}) = \frac{1}{2}\, k_{ij}(r_{ij} - r_{eq})^2 \tag{1.5}$$

where, $r_{ij} = \mid \vec{r_i} - \vec{r_j} \mid$ is the distance between the two atoms, r_{eq} and k_{ij} are equilibrium distance and spring constant.

A covalent angle is described by a harmonic angular potential of the form:

$$\mathcal{U}_a(\theta_{ijk}) = \frac{1}{2}\, k^{\theta}_{ijk}(\theta_{ijk} - \theta_{eq})^2 \tag{1.6}$$

where $\theta = \arccos \frac{\vec{r_{ij}}\vec{r_{kj}}}{r_{ij}r_{kj}}$ is the angle between atoms i, j and k. A simplified form can be

$$\mathcal{U}(\theta_{ijk}) = \frac{1}{2}\, k^{\theta}_{ijk}\, (\cos(\theta_{ijk}) - \cos(\theta_{eq})) \tag{1.7}$$

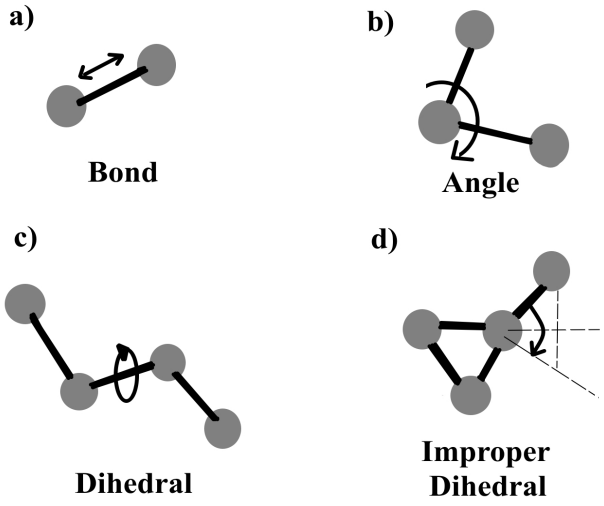

Figure 1.5: Bonded interaction potentials include (a) bond, (b) angle, (c) dihedral, and (d) improper dihedral

The dihedral angle ϕ is formed by four atoms with indices i, j, k, and l. ϕ is an angle between the normal $\vec{n}$ and $\vec{m}$ to the two planes of i, j, k and j, k, l.

$$\phi = \arccos \frac{\vec{n}\ \vec{m}}{\mid \vec{n} \mid\mid \vec{m} \mid} \tag{1.8}$$

where $\vec{n} = \vec{r_{ij}} \times \vec{r_{kj}}$ and $\vec{m} = \vec{r_{jk}} \times \vec{r_{lk}}$. The dihedral angle potential is represented as,

$$\mathcal{U}_d(\phi_{ijkl}) = k^{\phi}_{ijkl}\ (1 + \cos(m\phi_{ijk} - \phi_o)) \tag{1.9}$$

The another type of dihedral angle, *i.e.* improper dihedral is used to keep the groups planar and prevent molecules from flipping over to their mirror images. This type of dihedral is defined by a harmonic potential,

$$\mathcal{U}_{improper} = \frac{1}{2} k_\xi (\xi - \xi_o)^2 \tag{1.10}$$

where ξ is an improper dihedral angle and ξ_o its equilibrium value.
In this thesis, GLYCAM06$^{\mathrm{TIP5P}}_{\mathrm{OSMOr14}}$[26,27] force-field was used along with the TIP5P[28] water model throughout. As GLYCAM06$^{\mathrm{TIP5P}}_{\mathrm{OSMOr14}}$ had shown good agreement with experimental free energy of hydration data for small saccharides[29] .

1.4 Coarse-grained simulation

CG models helps to overcome the limitations of accessible length and time scales of all-atom MD by grouping together atoms into CG interaction sites. This reduces the number of degrees of freedom in the system and in addition typically creates a smoother energy landscape, which leads to faster dynamics. As a consequence, such CG models can be used to simulate larger systems for longer times. The gain in efficiency comes at the cost of losing some of the chemical detail in the system. One of the challenges lies in retaining enough information about the chemical details of the system in the CG representation.

In creating predictive CG models, different strategies have been developed to find effective interaction potentials between the CG sites. These potentials have enough information of the underlying system to predict their large scale behavior reliably.There are primarily two ways to transfer the information to obtain molecular interaction for CG model as shown in Figure 1.3 :

1. **bottom-up**: fundamental physical principles at the more detailed scale are used to parametrize a model at a CG scale

2. **top-down**: the behavior at larger scales is used to inform the interactions at more detailed scales

In this thesis, a bottom-up approach is used to obtain the interaction potentials for the CG model. The CG models consists of CG sites *i.e.* group of several atoms, and the interaction potentials are derived form atomistic molecular simulations. The two bottom-up coarse-graining methods used for that model, and had been successfully applied in the development of CG models of polysacharides, the Multi-Scale Coarse Graining (MS-CG)[30] method and Boltzmann inversion,[31] are described in more detail in the next section.

1.4.1 Multi-scale coarse graining (Force Matching)

The idea of the force matching strategy is to reproduce the average force acting on CG sites that are sampled in the all-atom system for the CG system. The force experienced by the group of atoms in the all-atom system, averaged over the all-atom conformation that correspond to the same CG sites is given as.

$$\langle f_I \rangle_A = F_{I,CG} \quad for\ all\ CG\ sites\ I = 1, ..., N_{CG} \tag{1.11}$$

Here, $\langle f_I \rangle_A$ is the average atomic force and $F_{I,CG}$ is the CG force acting on site I. The $F_{I,CG}$ can be used to generate $\mathcal{U}_{CG}$ according to the relation given below,

$$F_{I,CG} = -\frac{\partial \mathcal{U}_{CG}(R)}{\partial R_i} \tag{1.12}$$

where, $\mathcal{U}_{CG}$ is the CG potential energy.

Both forces $\langle f_I \rangle_A$ and $F_{I,CG}$ here correspond to those on the CG-sites for the same CG-sites configuration as shown in Figure 1.6[32] . The average forces on each CG sites in the all-atom system are constructed using the mapping function and propagating the individual atom forces to the CG sites. This procedure is applied to the entire reference trajectory in the all-atom system to extract the interaction potential between the CG sites.

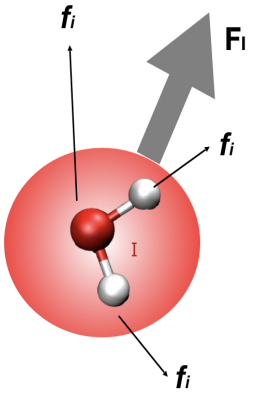

Figure 1.6: Demonstrating force matching[32] procedure by showing set of atomistic forces, $\langle f_I \rangle$ and its corresponding resultant CG force F_I for single water molecule.

The MS-CG method[30] is used throughout to derive non-bonded interactions for solute-solute, solute-solvent and solvent-solvent interactions separately. The separation ensured that solvent-solute interaction does not perturb the sensitive solute-solute interaction. This was achieved by separating the atomistic trajectory into three separate trajectories. Each individual trajectory has specific interactions *i.e.* solute-solute, solute-solvent and solvent-solvent. A MS-CG method[30] was applied on all the three trajectory to obtain specific interaction potential.

1.4.2 Boltzmann inversion

Boltzmann inversion(BI)[31] is based on matching the all-atom structure to obtain interaction potential for a given degree of freedom. It is based on the probability distribution of a canonical independent degree of freedom which obeys the Boltzmann distribution i.e.

$$\mathcal{P}(r) = Z^{-1} \exp[-\beta \mathcal{U}(r)] \tag{1.13}$$

From the above equation, the probability distribution$\mathcal{P}(r)$ can be calculated from the partition function *i.e.* $Z = \int \exp[-\beta \mathcal{U}(r)]dr$ with $\beta = 1/k_B T$ (where k_B represents the Boltzmann constant and T is the temperature). The corresponding interaction potential $\mathcal{U}(r)$ can be calculated from this probability distribution by

$$\mathcal{U}(r) = -k_B T \; ln(\mathcal{P} \; (r^N)) \tag{1.14}$$

where $\mathcal{P}(r^N)$ correspond to the probability of a CG configuration r^N obtained from the atomistic trajectory.

Bonded interactions such as bond, angle and dihedral potentials are calculated using BI from canonical sampling of the system, which is given by

$$\mathcal{U}(r)_{bond} = -k_B T \; ln(\mathcal{P}(r)) \tag{1.15}$$

$$\mathcal{U}(\theta)_{angle} = -k_B T \; ln(\mathcal{P}(\theta)) \tag{1.16}$$

$$\mathcal{U}(\phi)_{dihedral} = -k_B T \; ln(\mathcal{P}(\phi)) \tag{1.17}$$

where r, θ and ϕ are bond-length, angle and dihedral angle respectively. $\mathcal{P}$ is the probability distribution function for each degree of freedom.

In principle, these BI based interaction potential provide a good initial estimate for bonded interactions and could be used directly to perform CG simulations provided that the assumptions that the degree of freedoms are independent are approximately fulfilled. If too many other interactions influence their conformations, the corresponding interactions are typically overestimated and iterative optimizations steps are required.

1.4.3 Coarse-grained models for polysaccharides

A few CG models for polysaccahride systems have been developed until now. These include the parametrization to reproduce bulk thermodynamic data for the popular MARTINI model[33] , sampling polymer conformations based on the conformational space available to the glycosidic angles ϕ and ψ[15,34,35] , or deriving interaction potentials based on the MS-CG method[36,27,37] . In the latter model, a hybrid procedure was employed, where force matching was used to obtain non-bonded interactions while bonded interactions are obtained by BI. Non-bonded interactions for solute-solute, solute-solvent and solvent-solvent interactions were derived separately. This method offers a promising approach to elucidate structure-property relations in saccharides systems, because it can produce polysaccharide models that can be transferred to other concentrations as well as to longer polymer chains[27] and reproduces aggregation behavior and osmotic pressure of the atomistic system[37] .

To date, only few molecular modeling studies have addressed these for cellulose and chitosan assemblies. However, the conformations of cellulose[27] and single chitosan chains at atomistic[15] as well as in CG resolutions[15] , have been simulated and the aggregation of chitosan with different DA[38] and different monomer sequences[38] has also been studied for charged polymers with a MARTINI[33] like model.

1.5 Aim and overview of the thesis

The aim of this thesis is to better understand the self-assembly in these polysaccharides systems based on the effects of various modification and physical conditions on the aggregate structure. MD simulations have been employed to observe the formation and behavior of various aggregate structures and hydrogels formed from different monosaccharide units. Simulations with all-atom resolution were employed to provide a detailed picture of the local interactions and CG models for the different molecules were developed and extensively validated to study these systems at much larger scale.

First, cellulose, chitosan and similar molecules with various chemical modifications are simulated to understand how different perturbations of the intra- and inter-molecular hydrogen bond network affect the aggregation of these molecules. Structural analysis of the different morphologies generated by these polymer systems was performed. Then, CG models for different chitosan hydrogels are introduced and tested and finally, the potential applications of these models to optimize such systems for applications in fields

such as targeted drug delivery is demonstrated.

The rest of the thesis is structured as follows:

In chapter 2, the structure function relations for various cellulose derivatives and chitosan derivatives are analyzed. First, all-atom results for single polymers and dense solutions are shown. Then the development of CG models for all molecules and their application to study the aggregate structures were described. Aggregate structure were characterized by pore-size distribution, and contacts formed. Methylated, flourinated and chitin analogues with various hydrophobic modification were prepared with different patterns of substitution. Different aggregate structure were obtained for different types of substitution as well as pattern of substitution.

Chapter 3 describes the development and validation of an efficient and transferable CG model for chitosan. The model transferability across different concentrations, polymerization and degree of modification is explicitly tested. CG models for Doxorubicin (DOX) and Gemicitabine (GEM)were developed and polymer-drug interaction potential were also obtained.

In Chapter 4, chemically modified chitosan hydrogels were modeled for various conditions and system parameters. The effect of water concentration, type, degree and pattern of hydrophobic modification was investigated and their effects on the structural characteristics of the hydrogel such as the pore-size distribution, the average number of contacts and end-to-end distance of the polymers were analyzed.

Chapter 5, describes the migration of two model drugs molecules through the different hydrated network structures of modified polysaccharide chains that were obtained in chapter 4. Here DOX and GEM were chosen as model drugs. Initially, an all-atom analysis was performed to study the dependence on the type of interaction between both drugs and the polymers. CG simulations of their motion in the different chitosan networks were performed with both the drugs separately or in combination.

Finally, Chapter 6 provides a conclusions and summary of the results.

Chapter 2

Tailor-made cellulose derivatives

2.1 Introduction

The mechanical and structural properties of polysaccharides depend upon the intra- and inter- molecular hydrogen bonding of the polymers. Alterations in the monomeric units provide a tool to modify the structural properties by disrupting these hydrogen bonds. This approach can help us to understand what determines structure formation and thus guide the development of novel, tailor made carbohydrate based materials. It also provides insight to further understand the structure property relations of these polymers. Modifications such as methylation, fluorination and acetylation and charged glucosamine were used as shown in Figure 2.1. These modification have either hydrophobic or hydrophillic nature and were designed to selectively disrupt the hydrogen bond between the hydroxyl groups and monomeric oxygens of the polysaccharides *i.e.* cellulose and chitosan derivatives. Experiments with full control over the length and degree of substitution were constructed using Automated Glycan Assembly method[39,40] and had verified that the solubility and the gelation properties vary with these modifications as compared to pure cellulose[11] .

In this chapter, first all-atom MD simulations of cellulose and chitin derivatives are described. Simulations were performed to understand the effect of different functional groups on the molecular geometry and on the polymer-polymer association. In particular, we have also analyzed how the monomer sequence can lead to different conformations of the oligosaccarides with the same monomer composition. An-other important factor is the flexibility of the molecules which depends on the glycosidic dihedral angles shown in Figure 2.2. In that regard, the effects of substitution on the torsion angles (ϕ and ψ)

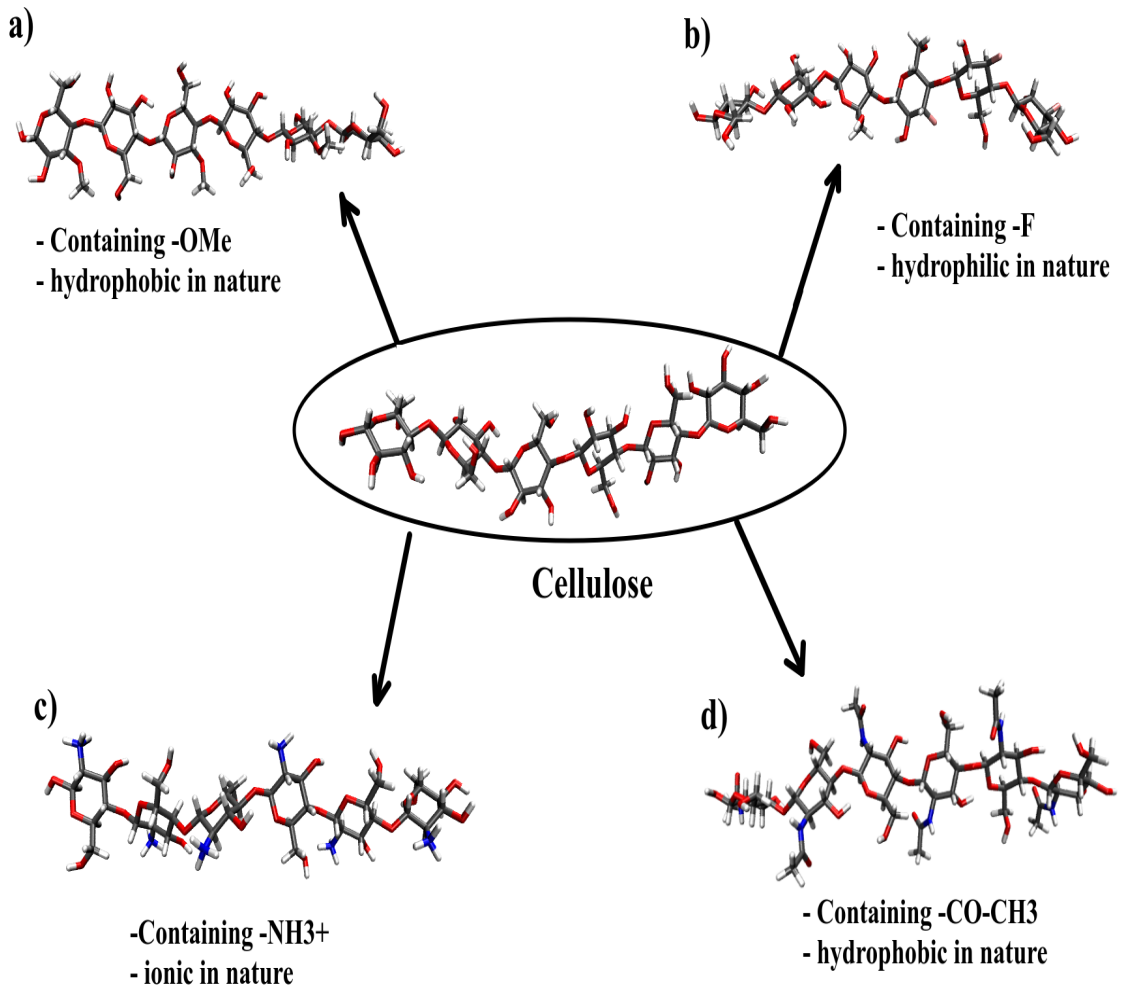

Figure 2.1: Example of modified cellulose structures (a) Methylation of alternating monomers (b) Alternative fluorination of alternating monomers increases the hydrophilicity. (c) Chitosan containing amine groups increases the positive charge in the polymer (d) Chitin, acetylation of all monomers increases the hydrophobicity.

were calculated. The change in ψ population are directly related to the presence of a hydrogen bond, and are therefore most affected by the modifications.

Then, to be able to study the self-assembly of these polymers on large time- and length scales, bottom-up CG models were developed for all molecules. A CG force field was developed using a hybrid approach based on MS-CG FM[30] and BI[31] to calculate

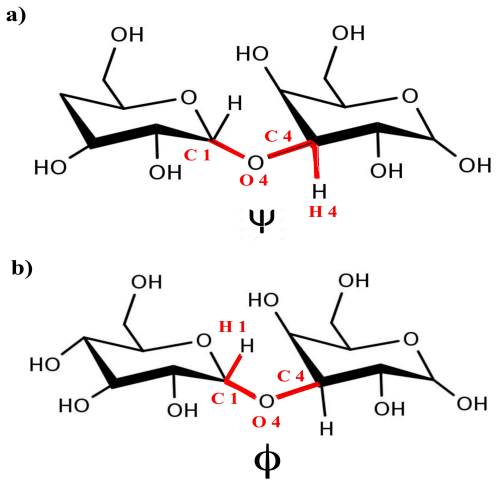

Figure 2.2: Definition of the dihedral angels ψ (C1,O4,C4,H4) and ϕ using the atoms (H1,C1,O4,C4)

the non-bonded and bonded interactions, respectively. The CG model was validated by comparing the radial distribution function (RDFs), end-to-end distances and radius of gyration to data from the respective all-atom system. The CG force-field was transferred to longer polymers (DP=12) and lower polymer concentration and used to follow aggregation in these systems. Different structural morphologies of the aggregates for the different modification types, but also for different modification patterns were obtained.

2.2 Methods: MD details

The following atomic system were simulated with Gromacs 5.1.2[41] :

1. Single β-D 1-4 linked glucose with DP=6 in water.
2. Single β-D 1-6 linked glucose with DP=6 in water.
3. Single β-D 1-4 linked glucose with DP=6 in water with methylation and fluorinated with different pattern *i.e.* alternate(A) and blocky(B) pattern.
4. Single N-acetyl-glucosamine. with DP=6 in water.
5. Single glucosamine polymer (charged and uncharged monomer) with DP=6 in water.

6. 25 chains of system 1-5 with 2100 water molecules with DP=6.

Initial structures for the different cellulose and chitosan based molecules were constructed with tleap[42] . The topologies were converted to gromacs format using the glycam2gmx script[43,44] and subsequently solvated in GROMACS[45] . The GLYCAM06$^{\text{TIP5P}}_{\text{OSMOr14}}$[26,27] force-field was used together with the TIP5P[28] water model. Parameters for existing modifications namely methyl, and acetylation were taken from the GLYCAM06 force-field[26] while parameter for fluorine were take from GAFF force field[46] . Partial charges for the modified monomers were calculated using the R.E.D scripts[47] and following the GLYCAM06 protocol[26] . A cut-off of 1.4 nm was used for Lennard Jones and electrostatic interaction. Long range electrostatics were evaluated using Particle Mesh Ewald[48] . Covalent bonds involving hydrogen atoms were constrained with the LINCS [49] algorithm while, water molecules were kept rigid using SETTLE[50] .

Energy minimization was performed following a standard protocol and a 50ns NPT equilibration at 300 K and 1 bar, using the Nóse-Hoover thermostat[51,52] and Parrinello-Rahman barostat[53,54] . Subsequently, a 400ns NVT equilibration run using the average box size extracted from the NPT trajectory and the Nosé-Hoover thermostat[51,52] was performed, followed by a 100 ns production MD run. A time-step of 2 fs was used and energy and pressure dispersion corrections where appropriate have been applied.

To extract forces for the coarse-graining procedure, separate reruns of the MD trajectories containing only solute-solute, solute-solvent or solvent-solvent interaction were conducted[27] . Long range electrostatics were calculated in the using the reaction-field method[55] using the same 1.4 nm cutoff as in the original simulations.

2.3 All-atom simulation results

2.3.1 Glucose and its derivatives

Two natural glucose oligomers having β 1-4 and β 1-6 linkage with DP =6 were simulated to study the effect of the glycosidic linkage. As expected, the simulation snapshots shown in Figure 2.3 represent linear and coiled structure for 1-4 and 1-6 linkage respectively. The end-to-end distance also changed from 2.58±0.3 nm for 1-4 linkage to 1.28± 0.2 nm for (1-6) linkage portraying more coiled configuration with 1-6 linkage.

Next, derivatives of cellulose, *i.e.* β 1-4 linked glucose with different well defined substitution patterns were modeled to study the effect of these moleculer structure and

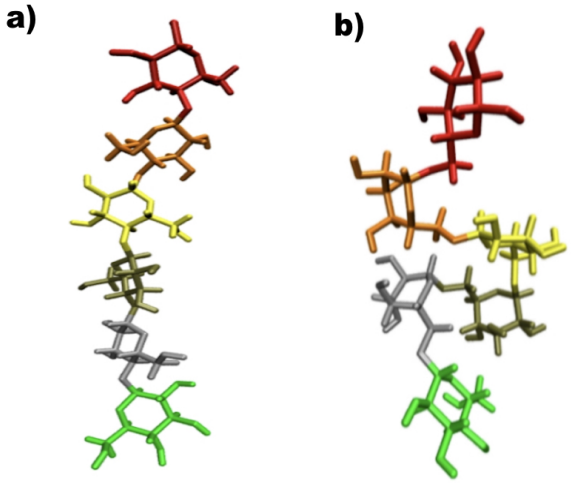

Figure 2.3: Simulation snapshots in (a). β-D 1-4 linked Glucose and (b) for β-D 1-6 linked Glucose.

the properties of the aggregates formed. Modifications were introduced by replacing the hydroxy group at C3 as shown in Figure 2.4 with methyl and fluorine. These selectively disrupt the intra-molecular hydrogen bonds reducing the rigidity of cellulose oilgosaccharides.

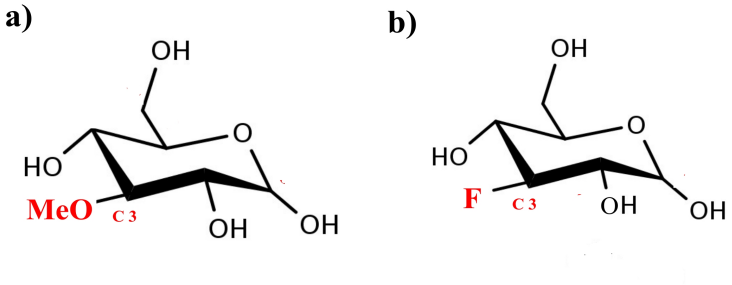

Figure 2.4: Chemical structure of (a). β-D- glucose methyl modified at C3 atom, (b). β-D-glucose fluorine modified at C3 atom.

Methylation tends to disrupt the hydrogen bond between the O(5) and OH(3) destabilizing the linear conformation of the cellulose. In addition, it is bulkier and represents an additional steric hindrance. Two different patterns namely alternate methylation$(AB)_3$ and di-block methylation (A_3B_3) were simulated to study the effect of the modification

pattern on the results.

The alternate$(AB)_3$ methyl substitution patterns shows very similar configuration as pure cellulose. As in alternated case, there is slight decrease in the in the ψ population as shown in Figure 2.5a), which result due to decreased tendency to form hydrogen bond between methyl and monmeric oxygen. However, the same degree of methylation with a block distribution leads to very different configurations with two diferent maxima for different linkage as shown in Figure 2.5b). The distribution again show negative ψ values for the links involving methylated monomers, however the sharp increase in the negative ψ values of the non-modified block indicates an increase of OH3-O5 hydrogen bond formation. The corresponding simulation snapshots show a bent structure for the

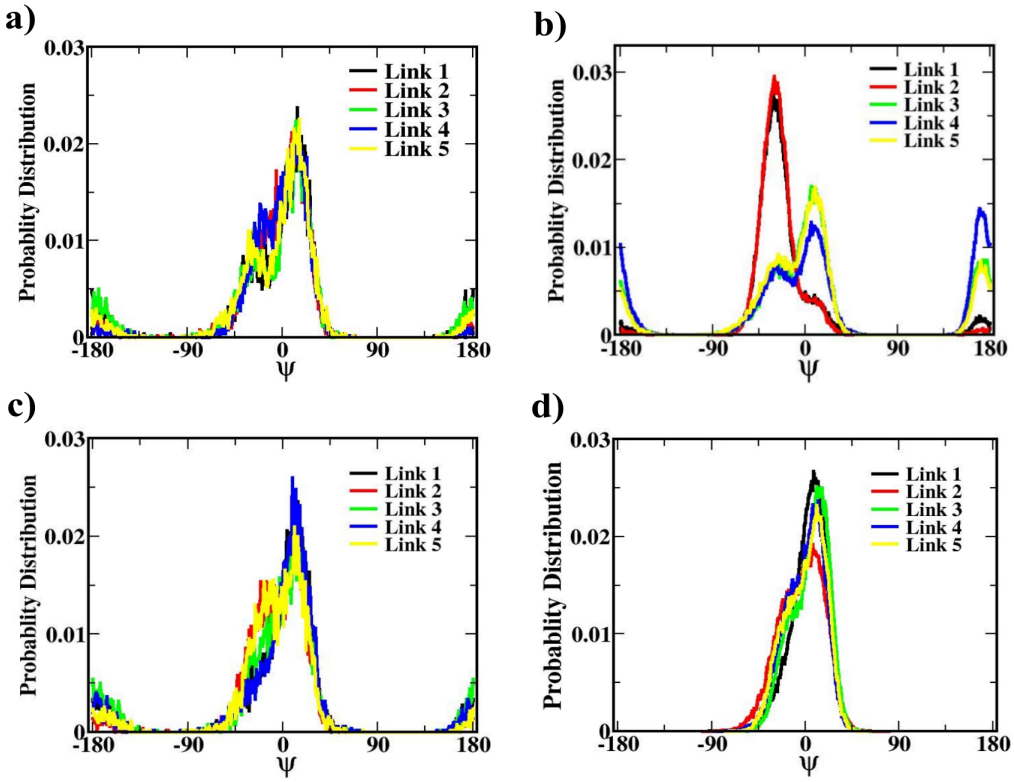

Figure 2.5: Analysis of ψ distribution for (a) alternating methyl modified cellulose (b) blockwise methyl modified cellulose, (c)alternating fluorine modified cellulose, and (d) blockwise fluorine modified cellulose. The residues are numbered from the nonreducing end to the reducing end.

block methyl pattern as compared to alternate pattern and pure cellulose as shown in Figure 2.7. The end-to-end distance measured for the block methyl modification, reduces from 2.7±0.2 nm for alternate methyl to 2.4 ±0.9 nm. The decrease in the average end-

to-end distance confirm overall structural changes in block methyl pattern. The time trace of the end-to-end distance also show in Figure 2.6, highlights the more flexible nature of the blockwise methyl modified cellulose as compared to the alternating methyl modified cellulose.

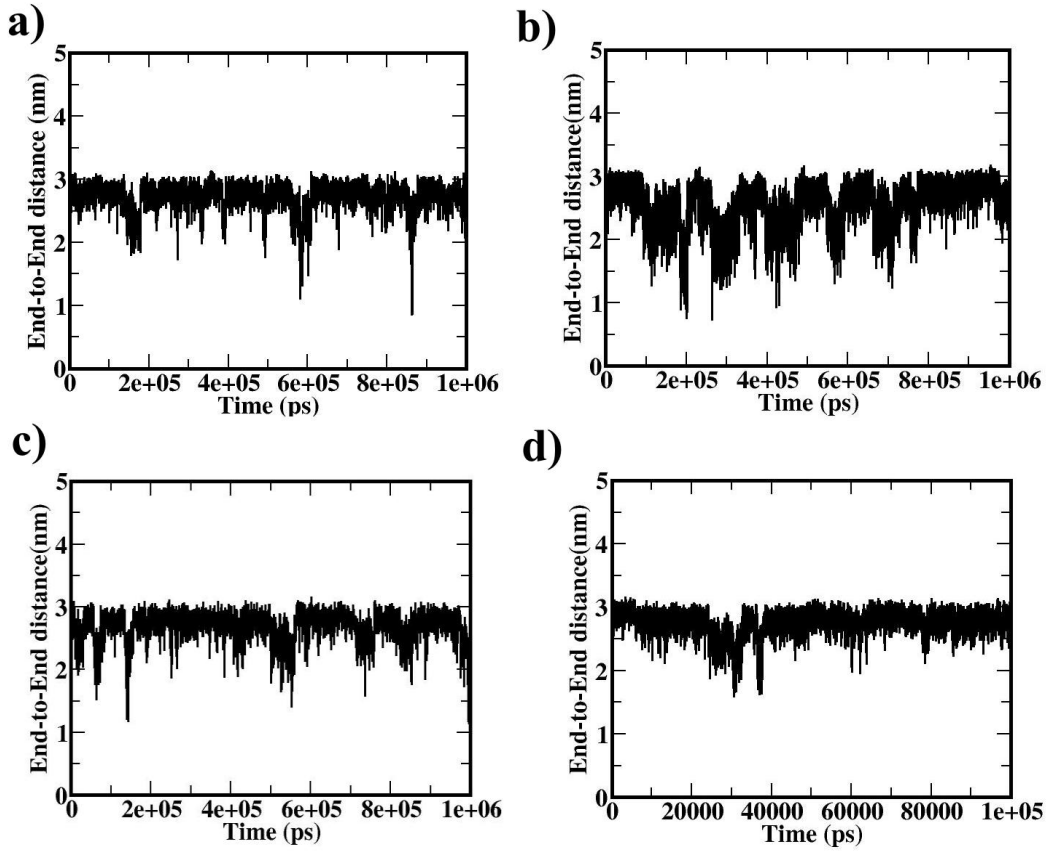

Figure 2.6: Analysis of end-to-end distance (a) alternating methyl modified cellulose (b) blockwise methyl modified cellulose, (c)alternating fluorine modified cellulose, and (d) blockwise fluorine modified cellulose. The end-to-end distance was monitored over 100ns. The residues are numbered from the nonreducing end to the reducing end.

Similar to methylation, fluorination also prevents the hydrogen bond formation as the OH group forming the hydrogen bond is no longer there, and affects the electron density of the monomer. The replacement of -OH by electron withdrawing fluorine affects the population of the ψ angles as shown in Figure 2.5. However, the effect is small, the fluorine modified cellulose molecules still have an overall linear conformation with both patterns of modification *i.e.* alternate or block as shown in Figure 2.7. However, the large distribution in average end-to-end distance shown in Figure 2.6c), present a very

flexible system for the alternated fluorine modified cellulose. The average end-to-end distance between alternate 2.70±0.2 nm to block pattern 2.75±0.2 nm does not show significant differences from each other. However, in alternate fluorination end-to-end distance vs time plot show more flexible structure as compared to blockwise fluorination pattern.

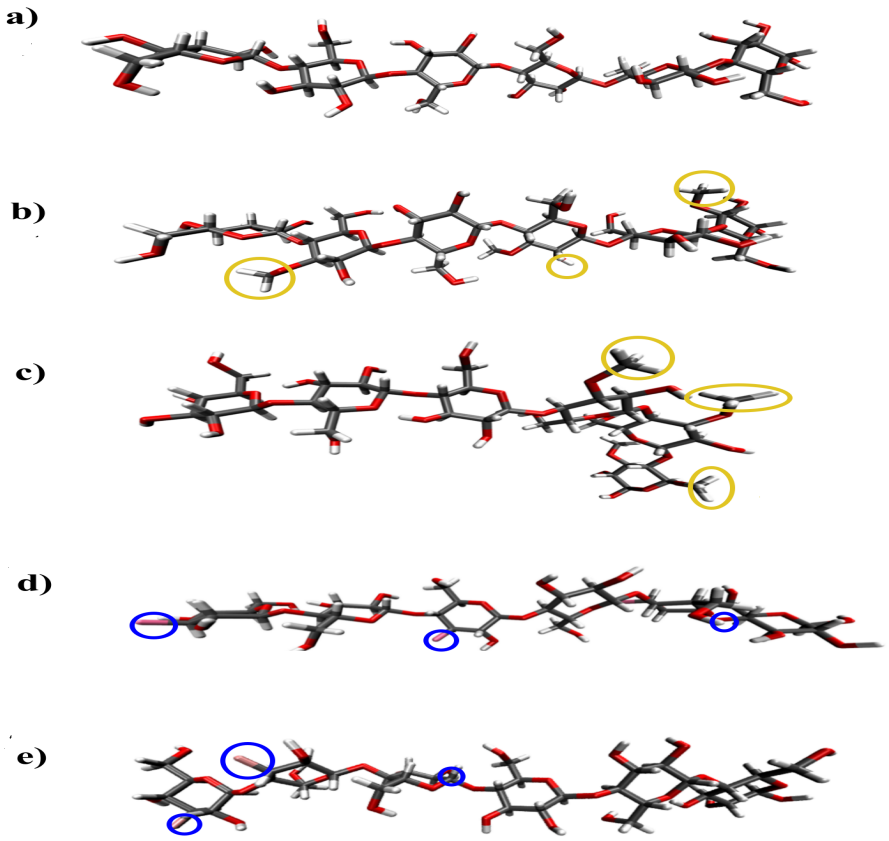

Figure 2.7: Simulation snapshots of system 1 and 3 with DP = 6 and 2000 water molecules. The simulation snapshots show the carbon atom in gray, oxygen in red, hydrogen in white, and fluorine in pink. The hydrophobic modification are encircled in yellow and hydrophilic modification in blue for (a) glucose (b) alternated methyl modified glucose (c) block methyl modified glucose (d) alternated fluorine modified glucose, and (e) block fluorine modified glucose.

Thus overall the two chemically different substitutions did not shown drastic structural variations as compared to pure cellulose. The strongest change was found in the configuration with block pattern methylation were seen.

2.3.2 Chitosan

Chitosan polymers are made up from three monomeric building blocks $GlcNH_2$, $GlcNH_3^+$ and GlcNAc as shown in Figure 2.10. Three polymers with single monomeric unit *i.e.* β 1-4 linked GlcNAc, $GluNH_2$, and $GluNH_3^+$ were simulated and their snapshots are shown in Figure 2.9.

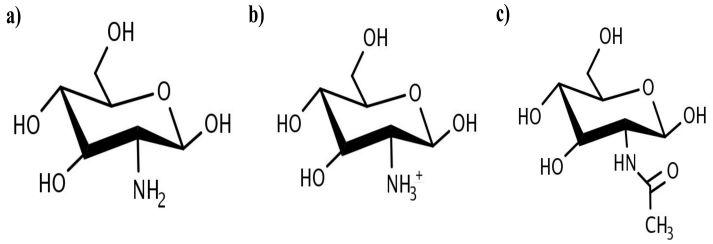

Figure 2.8: Chemical structure of (a).β-D- glucosamine(NH_2), (b) β-D-glucosamine(NH_3^+), and (c). β-D-Acetyl-glucosamine

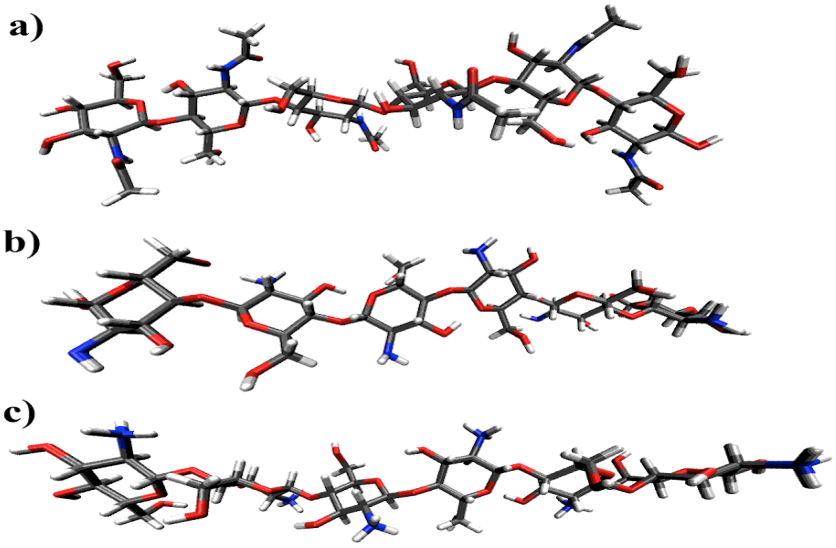

Figure 2.9: Simulation snapshots of system 4 and 5 with DP = 6 and 2000 water molecules. The simulation snapshots show the carbon atom in gray, oxygen in red, hydrogen in white, and nitrogen in blue for (a) N-acetyl glucosamine (b) neutral glucosamine (c) charged glucosamine.

As has been described before[15] we see that both, the charge and the acetylation of the monomers can have significant influence on the flexibility of the polymer.The maps in all

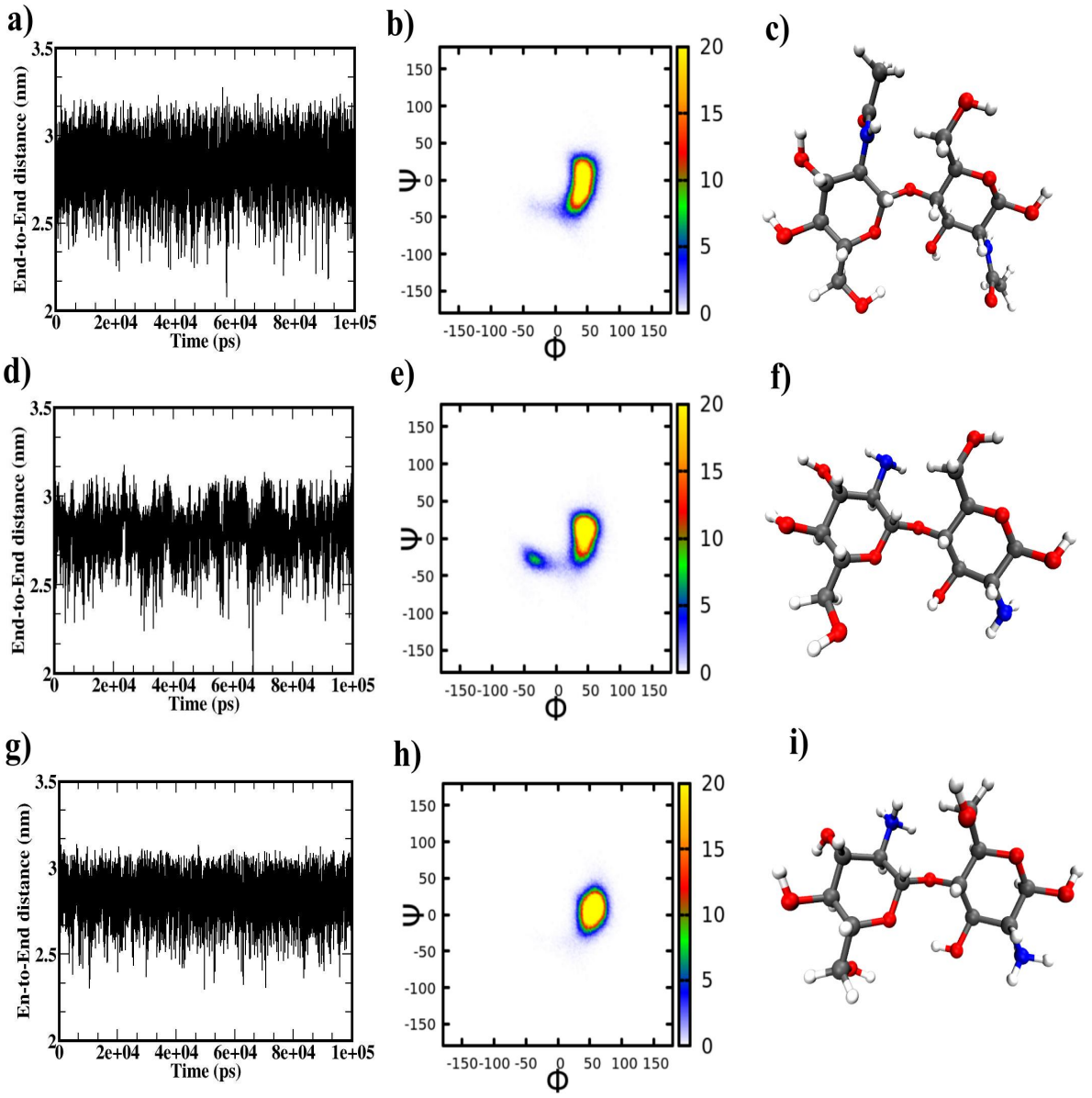

Figure 2.10: Analysis of end-to-end distance and conformational maps of ϕ and ψ of chitosan (a) N-acetyl glucosamine (b) neutral glucosamine(NH_2) (c) charged glucosamine(NH_3^+) obtained by MD simulations. The end-to-end distance was monitored over 100ns.The residues are numbered from the nonreducing end to the reducing end. The dihedral angles ϕ and ψ are shown on x- and y- axes, respectively.

cases shown in Figure 2.10 have a main minimum present at the same angle. However, the charged monomer(NH_3^+) had been shown a slight reduction of conformational flexibility in comparison to neutral monomer(NH_2)[15] . The charge of the monomers also have

significant influence on the flexibility of the link. As, there is a existence of a second minimum in case of full uncharged glucosamine as compared to charged one as shown in Figure 2.10. The average polymer conformation is linear in all the cases in Figure 2.9 and the end-to-end distance does not show significant difference as varying from 2.84±0.12 nm for Glc-NH_2 to 2.83±0.11 nm in Glc-NH_3^+ and 2.82±0.14 nm for GlcNAc.

2.4 CG model and mapping

Polymers behave differently in a crowded environment and different molecular properties modulates the aggregation and structure of these polymer system. Along with that, polymer systems usually have slow dynamics. An efficient approach was required to study the self assembly of these system at longer length and time scale. A CG simulation method was proposed as an appropriate tool to study their network structure formation.

In the CG model, each monosaccharide was mapped onto three coarse-grained interaction sites. The modifications were represented by modified sites for the methyl, amine and fluorine containing sites while the larger acetyl groups were modeled as an additional site, as shown in Figure 2.11. Water molecules were represented as a single CG site. The interaction potentials between these sites were generated using Boltzmann inversion[31] for the bonded interactions and the MS-CG method[30] for non-bonded interactions, following the procedure described by Sauter *et al*[27] .

2.4.1 CG simulations for short oligomers

CG simulations were performed with Gromacs 4.6.4[41] . Systems 1-5 containing single polymer and 25 polymer chains with DP=6 and 2,500 water molecules of glucose, methyl and fluorine modified glucose and charged as well as uncharged glucosamine were simulated. Two different patterns, alternate and blocks of three were simulated for methyl and fluorine modified cellulose. The initial CG structures for all the short oligomers were obtained from their corresponding atomistic representation. All CG simulation were conducted in the NVT ensemble using the Leap-Frog integrator[56] with the Nóse-Hoover thermostat[51,52] . A 1.4 nm cut-off was used for CG simulations throughout. A 10ns production run was done and results were used for validation of the model by comparing the RDFs, end-to end distances and radius of gyration obtained from the CG and atomistic system.

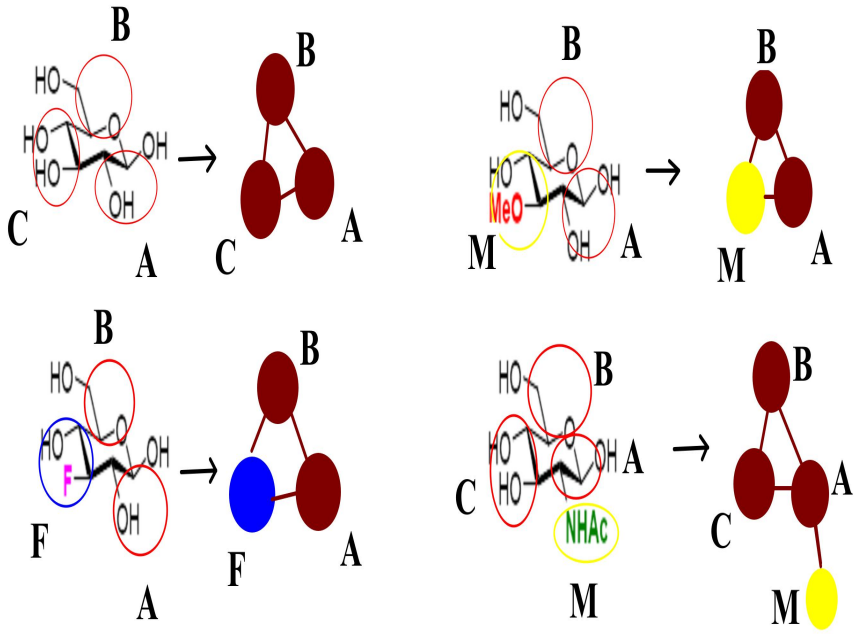

Figure 2.11: All atom and coarse-grained representation of (a). β-D- glucose, (b). methyl modified glucose (c). fluorine modified glucose (d) N-acetyl glucosamine

2.5 Model validation

2.5.1 Cellulose

To validate the performances of CG force field, RDFs between all interaction sites of the CG model were compared and showed excellent agreement with their equivalent obtained from all-atom simulations. The RDFs of the atomistic and CG trajectories of β-D glucose with DP=6 and 2100 water molecules are shown in Figure 2.12 for the CG sites A and B with themselves and with water.

The RDFs show good overall agreement of the short range structural features, and the A-WAT and B-WAT RDFs, which were previously found to be the most sensitive to perturbations[27] , show that aggregation behavior is captured correctly in the CG-FFs. Overall, local structure and features are well represented in all CG RDFs. A CG model for β 1-6 linked glucose was also developed and showed similar agreement of RDFs as β 1-4 link glucose.

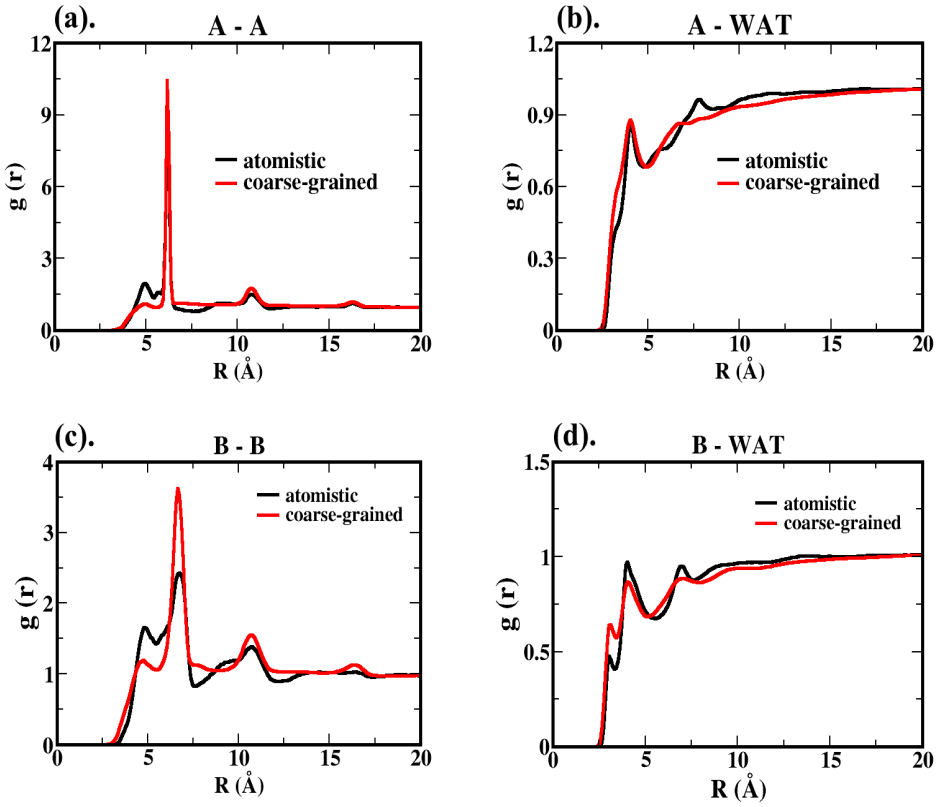

Figure 2.12: Comparsion of AA and CG RDFs for interaction involved with CG site type A and B with itself and water. (a) A-A (b) A-WAT, (c) B-B, and (d). B-WAT

2.5.2 Methyl modified cellulose

Next, CG-FFs were developed for methyl modified cellulose to study the network structure formed by these molecules, as compared to pure cellulose. As for all-atom system, two patterns, block and alternate were analyzed as shown in Figure 2.13. The CG interactions were developed for both patterns, alternate and block, separately. The model performance was analyzed by comparing RDFs between M(modified) beads and between M beads and water. Due to the hydrophobic nature of the methyl modification, it was expected to plays an important role in polymer-polymer association.

Comparing the RDFs shown in Figure 2.13, differences in the short range structure between the two modification patterns become apparent. The short range peak at 5Å and 10Å contain large contributions from the first and second bonded neighbors, respectively. In the alternate pattern, all modifications with in the same molecules are 2^{nd} neighbor, so the second neighbor peak at 10Å is very pronounced. The peak at 5Å in this case comes entirely from the non-bonded assembly. It is noticable, that in the CG model this

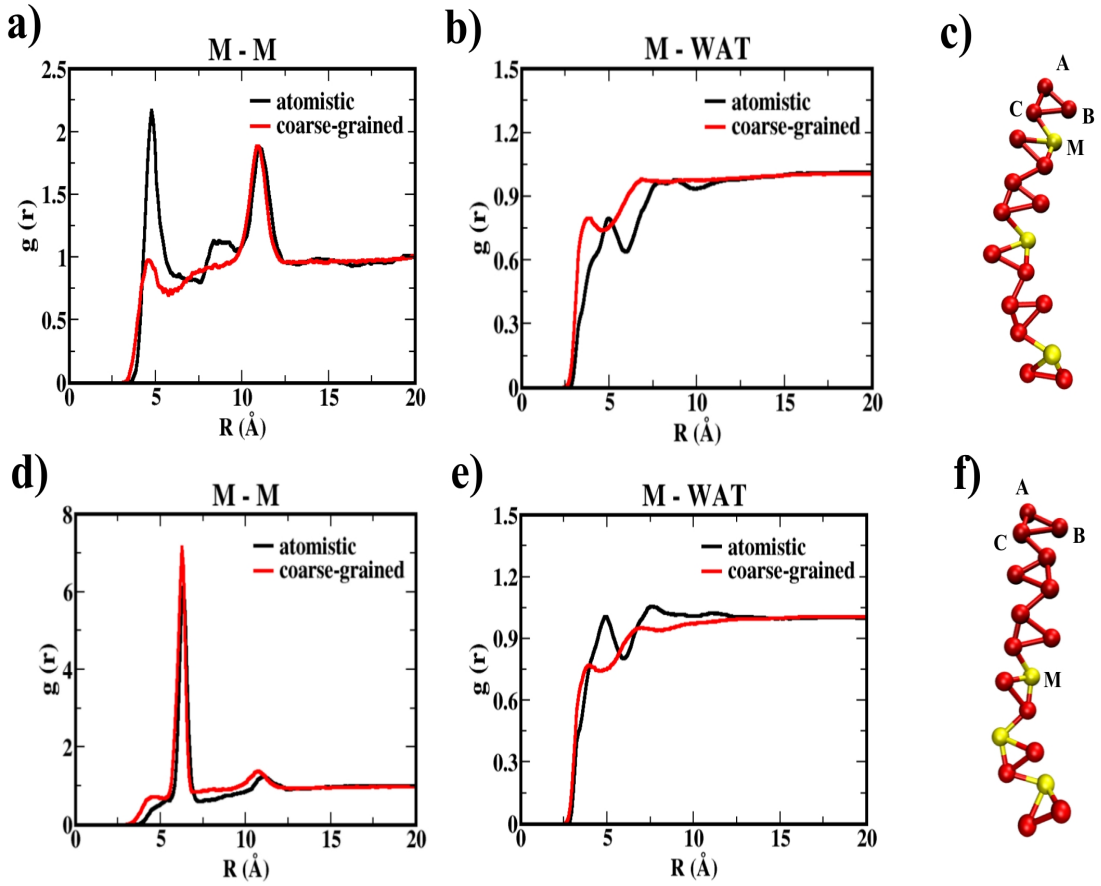

Figure 2.13: Comparison of AA and CG RDFs and their corresponding polymer snapshot for interaction involved for (a) M-M (b) M-WAT (c) snapshot, for alternate methyl modification and (d) M-M (e) M-WAT and (f) snapshot for block methyl modification.

peak is reduced compared to the atomistic case, whereas the peak at 10Å is very well captured.

Figure 2.13d) has a less pronounced second peak compared to Figure 2.13b) because in the block pattern as there is only one second neighbor pair. Instead, the 5Å peak has drastically increased as a result of the bonded neighbors and very good agreement between the CG and all atom representation is found. The water RDFs show similar behavior irrespective of modification pattern and show overall good resemblance with the atomistic counterpart.

Similarly, the fluorine modified cellulose with both pattern of modification was developed. Overall, it showed good agreement between the RDFs for all-atom and coarse-grained simulation respectively.

2.5.3 Amine (-NH_2 and -NH_3^+) groups

The systems with amine groups (-NH_2 and -NH_3^+) were evaluted as shown in Figure 2.14. Similar to the methylated system, the RDFs clearly demonstrate that the developed force field was able to capture the overall aggregation behavior and the local structure of the atomistic system well.

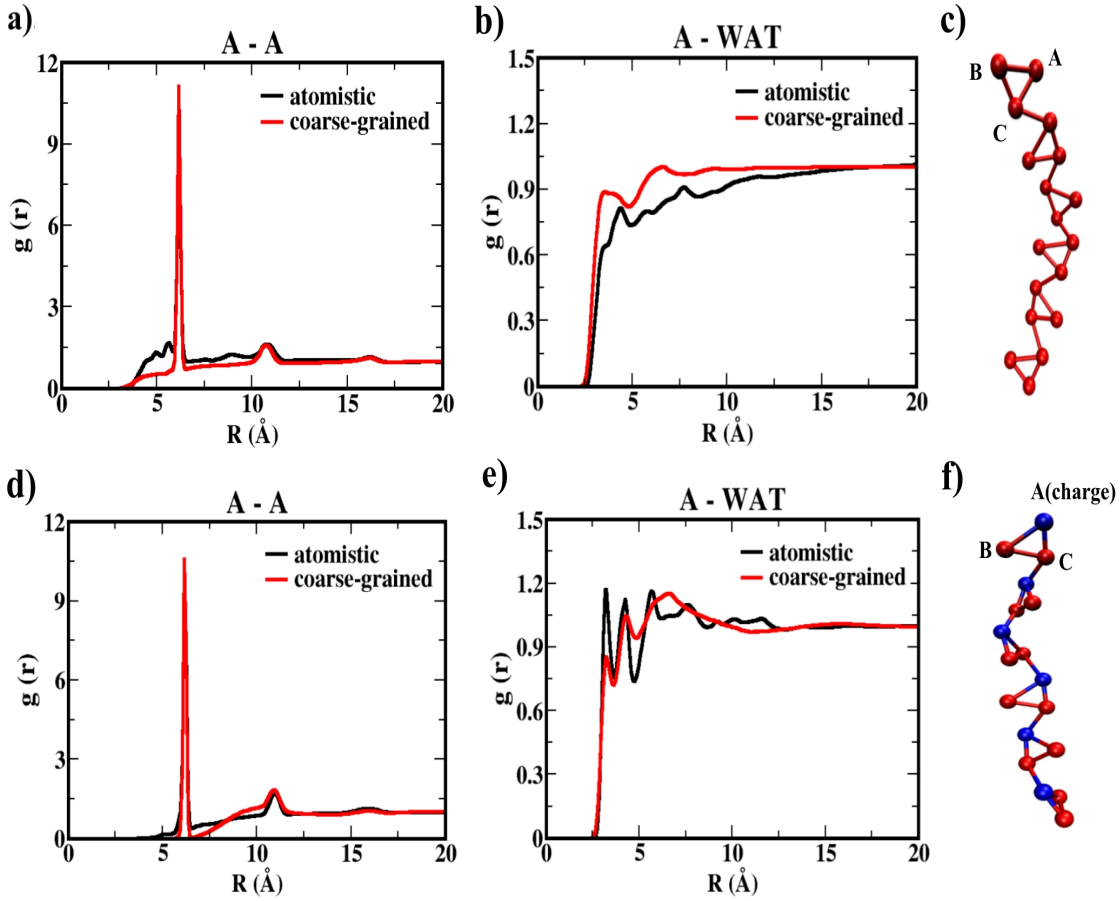

Figure 2.14: Comparison of AA and CG RDFs of neutral and charged glucosamine and their corresponding polymer snapshot for interactions (a) A-A (b) A-WAT (c) snapshot for uncharged system (d) A-A (e) A-WAT and (f) snapshot for charged system.

The RDFs shown in Figure 2.14 (a & b) correspond to uncharged glucosamine, while Figure 2.14 (d & e) correspond to charged glucosamine. Comparing the RDFs, the minimum bead distance between the charged A sites has increased in Figure 2.14d) as compared to that of the neutral molecules in Figure 2.14a). This shift is properly captured by CG FFs. In addition, the charged monomer leads to a more ordered structure of water beads around the charged beads. Figure 2.14e) clearly shows water shell for-

mation around the charged bead. Overall, the location of water shells in the CG have good agreement with the atomistic structure, but are less pronounced and are smoothed out after the third shell.

2.5.4 Single polymer conformation

The end-to-end distances for single polymers were calculated and compared with their corresponding atomistic end-to-end distances. They provide useful information about the overall conformations of the molecules and about the effect of type and pattern of modification on the individual molecules. The end-to-end distances are summarizes in Table 2.1. In most cases, atomistic and CG distances show good resemblance with each other. However, in the case of β 1-6 linked glucose, a significant difference between the end-to-end distance for atomistic and CG simulation appear. The 1-6 linked glucose tend to form a coiled structure in atomistic simulation, which seems to linearize the structure in the CG simulation. A possible explanation is that, the BI bonded interaction are too over-determined, making 1-6 linkage more stiffer. An solution can be to use iterative BI to make molecule more flexible and get a better glycosidic link sampling. Despite this observation, also in the CG model the 1-6 linked glucose has the shortest end-to-end distance and very large fluctuations, indicating that the high flexibility of the 1-6 link is at least partially captured by the CG model.

	Atomistic		Coarse-Grained(CG)	
Modification	End-to-End distance(nm)	Radius of Gyration(nm)	End-to-End distance (nm)	Radius of Gyration (nm)
Glu(1-4)	2.58 ± 0.32	0.90 ± 0.00	2.86 ± 0.12	0.93 ± 0.02
Glu(1-6)	1.28 ± 0.26	0.60 ± 0.04	1.96 ± 0.62	0.78 ± 0.14
Glu-OMe(A)	2.73 ± 0.22	0.93 ± 0.04	2.79 ± 0.19	0.92 ± 0.03
Glu-OMe(B)	2.47 ± 0.88	0.93 ± 0.06	2.70 ± 0.22	0.89 ± 0.03
Glu-F(A)	2.70 ± 0.24	0.91 ± 0.04	2.73 ± 0.21	0.90 ± 0.03
Glu-F(B)	2.75 ± 0.19	0.93 ± 0.02	2.75 ± 0.19	0.91 ± 0.03
Glu-NAc	2.82 ± 0.14	0.97 ± 0.01	2.65 ± 0.14	0.95 ± 0.01
Glu-NH_2	2.80 ± 0.12	0.94 ± 0.01	2.81 ± 0.15	0.92 ± 0.02
Glu-NH_3^+	2.83 ± 0.11	0.94 ± 0.01	2.87 ± 0.08	0.93 ± 0.01

Table 2.1: Comparison between atomistic and CG end-to-end distance and radius of gyration for cellulose and chitosan and their derivatives. Here A and B correspond to alternating and blockwise modification respectively

2.6 Aggregation and aggregate properties

After validation, the CG models were applied to model the self assembly of polymer systems at greater length and longer time scales. Network structures of these polymers with different type and pattern of modifications were generated in the CG simulations and subsequently analyzed in terms of their pore sizes, the end-to-end distances of the polymers and the average number of contacts formed between the polymers as well as between the modifications. The distribution of pore sizes, was calculated by the method described in Ref[57] . This procedure finds the largest sphere that can be constructed to contain randomly selected points in the network. This is achieved with a constrained nonlinear optimization of the center of the sphere using the SOLVOPT routine[58] .

CG systems containing 100 polymer chains with DP = 12, and 40 000 water beads (400 water molecules per chains) with different modification, were generated by following the same steps as described in the previous section for the hexamers. Initial CG structures were obtained from a 10 ns NPT equilibration simulation run using the Nosé-Hoover thermostat[51,52] and Parrinello-Rahman barostat[53,54] with all-atom resolution. Then, the atomistic structures were mapped to their CG representations using the VOTCA package[59,60] . All the CG simulation were simulated for 100ns in NVT at the optimal volume obtained in the NPT run with the Nosé-Hoover thermostat[51,52] .

The following system were simulated with Gromacs 4.6.4[41] .

1. 100 cellulose chains with DP =12 and 40,000 water beads.
2. 100 chitin chains with DP =12 and 40,000 water beads.
3. 100 cellulose chains with DP =12 having methyl modification and 40,000 water beads with alternate modifications pattern.
4. 100 cellulose chains with DP =12 having methyl modification and 40,000 water beads with modifications in blocks of three.
5. 100 cellulose chains with DP =12 having fluorine modification and 40,000 water beads with alternate modifications pattern.
6. 100 cellulose chains with DP =12 having fluorine modification and 40,000 water beads with modifications in block of three.
7. 100 chitosan chains with neutral glucosamine with DP =12 and 40,000 water beads.

8. 100 chitosan chains with charged glucosamine with DP =12 and 40,000 water beads.

2.6.1 Cellulose and chitin structure

First we characterized the aggregation behavior of the natural polysaccarides, cellulose and chitin. Both polymers self-assemble into fibrils from different initial conditions. Simulation snapshots of the cellulose and chitin cluster are shown in Figure 2.15. All polymers have straightened out and the average end-to-end distance for cellulose is 6.03 $\pm$0.11 nm while for chitin it is 5.74 $\pm$ 0.07 nm. On further analysis, approx. 50% of the polymer are aligned anti-parallel to each other while the rest are aligned parallelly. The self-assembled structure of both, cellulose and chitin show some twisting of the fibrils. The crystal structure of α-chitin and cellulose have been resolved[61,62] and can be compared to the self-assembled fibrils in our simulation model. Alignment is not as optimal in crystal structure, but structure with both alignments had been found experimentally for different conditions and thus neither orientation is not completely unfavorable. Regarding twisting of the fibrils, it could be brought about by the assembly kinetics e.g. to accomodate initial contacts formed with different molecules. On the other hand, twist is also observed in many atomic simulations of cellulose fibrils[29,63] and was found to depend sensitively on the interplay of different force field contributions[64] .

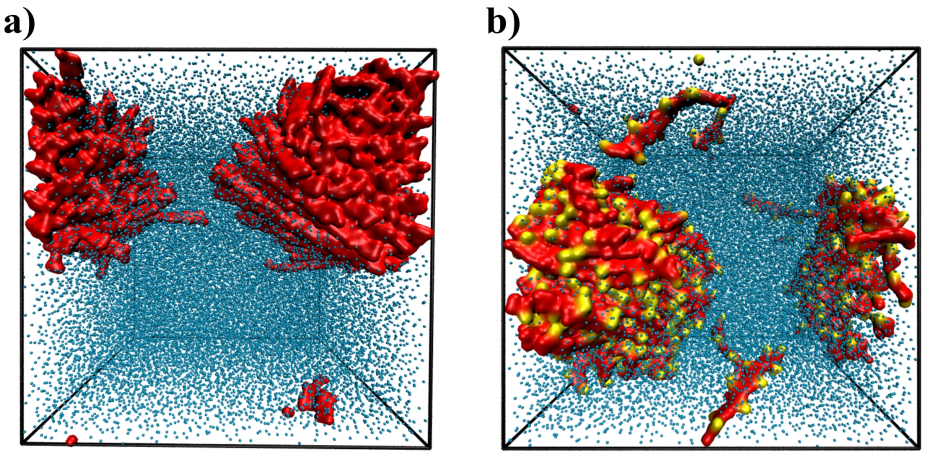

Figure 2.15: Simulation snapshots of (a) cellulose and (b) chitin networks with 100 polymers of DP=12 and 32 water molecules/monomer.The simulation snapshots show the polymer backbone (A,B,C beads) in red, modifications (M beads) in yellow and water molecules as blue dots

A similar model for chitin was used for longer polymer with DP=50, as described in chapter 4 and showed to form fibrils as well. The fibril structures formed by the cellulose and chitin oligomers show that the CG model closely captures the aggregation behavior that is expected for these molecules.

2.6.2 Methylated and fluorinated cellulose hydrogels

Simulation snapshots of the systems with 100 polymers, DP =12 and 40,000 water beads of cellulose with methyl and fluorine modification are presented in Figure 2.16. These polymer have either an alternate or a block (3 modifications) pattern of methyl and fluorine modifications. Strikingly, the simulation snapshots and pore-size distributions differ dramatically for the different modification patterns demonstrating that pattern can have a dramatic effect on the aggregation behavior of the molecules. In case of alternated methyl modification, polymer aggregate to aligned fibrils was observed similar to that found for unmodified cellulose while with block modification, the polymer was soluble and distributed evenly through the box.

This is reflected in the pore size distribution in Figure 2.16c), which shows a large shift in the pores sizes, with large pores corresponding to the separate solvent phase for the alternate pattern. The pore size decreases from 4.0 nm in alternate pattern to 1.5 nm in block pattern. The end-to end distance had increased from 5.1 $\pm$ 0.0 nm in blockwise to 5.7$\pm$ 0.1 nm in alternate patterns, showing the effect of polymer aggregation which leads to alignment and thus a more linear configuration for alternate pattern. The average number of contacts between the M beads was also calculated. As obvious from the snapshots the average number of contacts decreased drastically from 638$\pm$86 for the alternate pattern to 270$\pm$23 in the blockwise pattern. The average number of contact increased with alternate pattern due to the aggregation of the polymer. The solubility in block pattern can be due to the steric hindrance of the adjacent methylated monomer, causing non-linearity in the polymer. The non-linearity was found in the snapshots of both atomistic as well as coarse-grained snapshot of single polymer shown in Figure 2.7 c) and Figure 2.17c) respectively. Overall, pattern of modification plays a bigger role in polymer aggregation.

Surprisingly for fluorine modifications, the opposite effect was observed. The polymer were soluble for the alternate modification pattern but formed highly aligned aggregates with the block pattern. The pore size distributions shown in the Figure 2.16 illustrate an increase in the pore size from alternate to blockwise fluorinated pattern. Similarly,

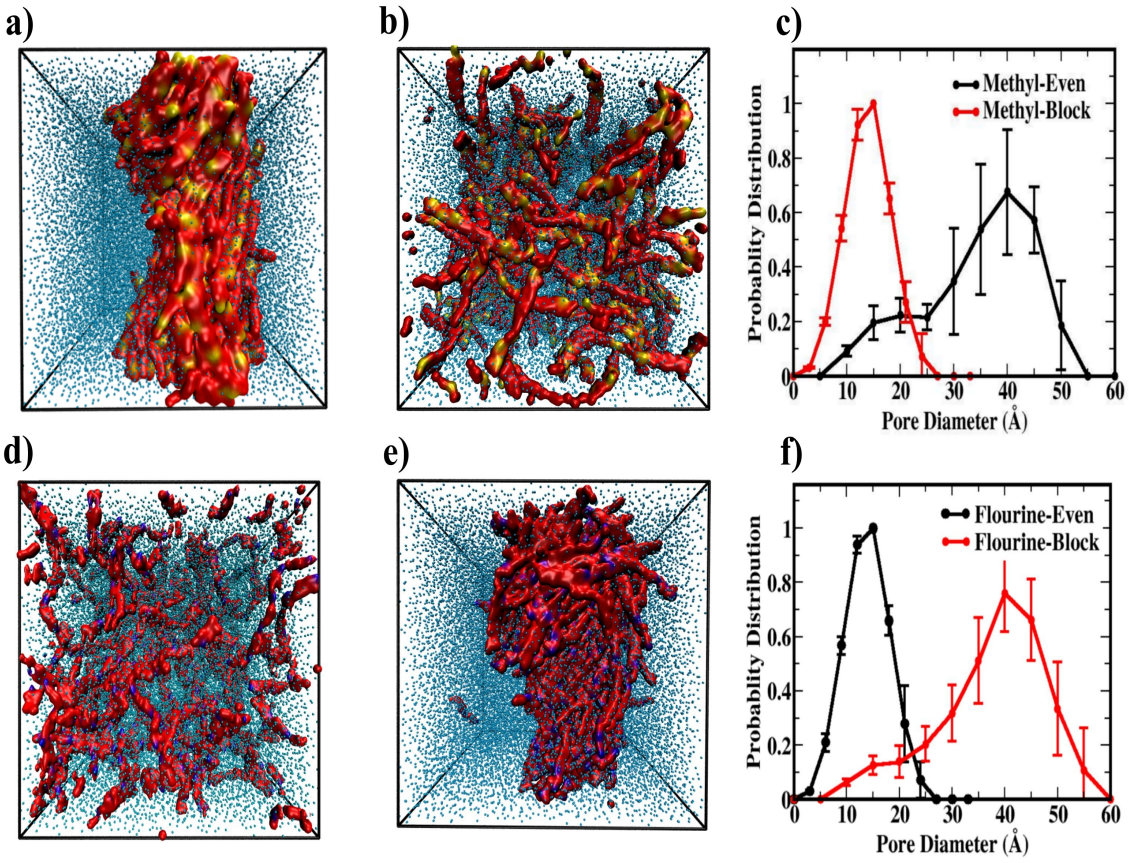

Figure 2.16: Simulation snapshots and pore-size distributions of cellulose networks with 100 polymers of DP=12 and 32 water molecules/monomer. The simulation snapshots show the cellulose backbone (A,B,C beads) in red, methyl modifications (M bead) in yellow, fluorine (F bead) modifications in blue, and water molecules as blue dots for (a) alternately methylated cellulose (b) blockwise methylated cellulose (d) alternately fluorinated cellulose, and (d) blockwise fluorinated cellulose.

the end to end distance changes from 4.8±0.01 nm in the alternate to 5.6±0.1 nm in the blockwise pattern. The polymer has become more linear with block modification, due to the aggregation of the polymers as shown in Figure 2.16e). Again, the average number of contacts between the F beads, had increased from the alternate to block patterns *i.e.* 167±23 to 1000±93 portraying the strong polymer aggregation in block pattern. It is noticable, that the increase of contacts in the aggregates is much higher than the one observed for methyl modification, by a factor of 5.9 as compared to 2.4.

The data for end-to-end distances of single polymer with different modifications and modification pattern are shown in Table 2.2 compared to the dense solution.

Modification	End-to-End distance(nm) (Single chain)	Radius of Gyration(nm) (Single chain)	End-to-End distance(nm) (100 chains)
Glu(1-4)	5.56 ± 0.50	1.77 ± 0.08	6.0 ± 0.1
Glu-OMe(A)	5.13 ± 0.72	1.70 ± 0.11	5.7 ± 0.1
Glu-OMe(B)	5.08 ± 0.74	1.67 ± 0.12	5.1 ± 0.0
Glu-F(A)	4.63 ± 0.82	1.58 ± 0.14	4.8 ± 0.0
Glu-F(B)	5.24 ± 0.64	1.70 ± 0.10	5.6 ± 0.1
Glu-NAc	5.48 ± 0.38	1.81 ± 0.59	5.7 ± 0.1
Glu-NH_2	5.46 ± 0.51	1.74 ± 0.86	5.4 ± 0.5
Glu-NH_3^+	5.78 ± 0.25	1.80 ± 0.04	5.7 ± 0.2

Table 2.2: Polymer end-to-end distance for single polymers in solution. The errors represent one standard deviation. Here A and B correspond to alternating and blockwise modification respectively

The single cellulose and chitin polymer resemble closely with the network end-to-end distance. For the methyl-modified polymers, no great differences were found between the different modification patterns. Both have an end-to-end distances that are slightly lower than pure cellulose, and similar standard deviation which mark them as more flexible than pure cellulose. Although comparison of the hexamers with all-atom results has shown, that it is possible that the CG model may not correctly capture the greater flexibility of the blockwise-methylated cellulose, the CG model predicts strong differences for the aggregation of these two molecules, so there must be some difference captured by the model. A possible explanation may lie in the different shape of the two patterns, which can be seen in the snapshots in Figure 2.17c). While the molecule with an alternate pattern curves smoothly, the blockwise pattern leads to sharp kinks in the molecular structure, which makes it less suitable for stacking. Differences in flexibility were found for the different patterns of fluorination. The fluorine modified polymer with the alternate pattern showed a reduced end-to-end distance and larger as compared to the blockwise modification pattern. Thus the blockwise fluorine modification causes the polymer to be stiffer which facilities to aggregation compared to the more flexible alternate fluorination. In addition, it is possible that the blockwise pattern leads to enhanced interaction between the modification, as suggested by the strong increase in average contacts between the F beads in the aggregates. Oligosaccharides with blockwise and alternate patterns of modifications have been produced

experimentally using the Automated Glycan Assembly method[39,40] and have confirmed the opposing trends observed for the fluorine and methyl modification. While molecules with blockwise methylation and alternating fluorination appeared completely soluble[11] , the XRD spectra of molecules with alternate methylation and blockwise fluorination showed characteristics resembling those observed for pure cellulose.

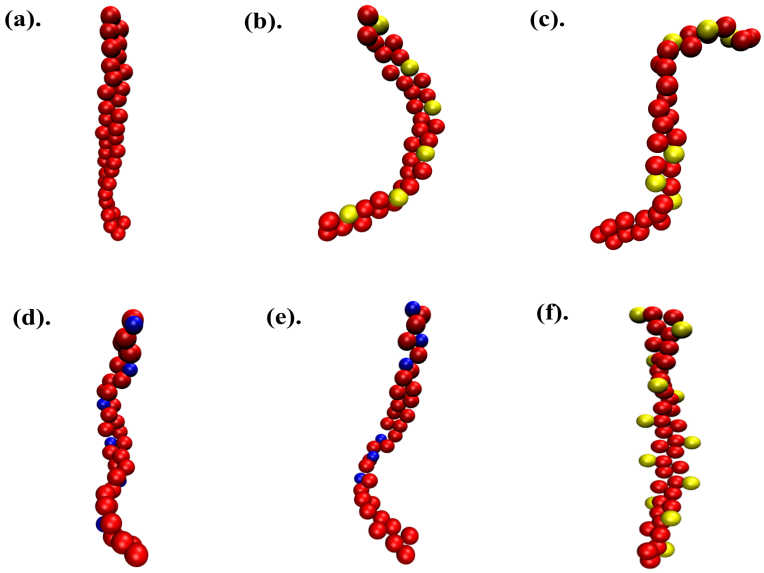

Figure 2.17: Simulation snapshots of single cellulose polymers with DP=10 and 40000 water molecules/monomer. The snapshots show the cellulose backbone (A,B,C beads) in red, methyl and acetyl modifications (M bead) in yellow, fluorine modification F in blue and water molecules as blue dots for a) pure cellulose (b) 50% methylated cellulose with alternating pattern (c) 50% methylated cellulose with block pattern (d) 50% fluorinated cellulose with alternating pattern (e) 50% fluorinated cellulose with block pattern (f) chitin.

2.6.3 Chitosan hydrogel

Chitosan self-assembly is governed by both charge and DA. The effect of DA will be discussed thoroughly in chapter 3 and 4. Chapter 3 shows the model development of the chitosan. Chapter 4 shows the self-assembly for longer polysaccharides with DP =50 and also the effect of degree and pattern of acetylation as well as other hydrophobic modification namely butyl and heptyl on hydrogel structure. Here, the effect of charges in the full deacetylated chitosan is investigated.

Simulation snapshots of glucosamine polymer with neutral and charged monomers of 100 chains with DP =12 and 40,000 water beads are shown in Figure 2.18 a) & c). On first sight both solution appear similar, with the polymer distributed evenly through the simulation box. The difference in the network structure can be observed from the pore size distributions, also shown in Figure 2.18 c). The charged glucosamine network have smaller pore size diameter of 1.2 nm, while uncharged glucosamine have 1.5 nm pore-size diameter. This is caused by the electrostatics repulsion between the charged sites, causing the chains to distribute as evenly as possible through the box to maximize the distance between the charged sites, whereas the slight association between the neutral chains frees up space for larger pores in the solvent phase. This is also reflected in the minimum distance between polymer, changing from 0.29 nm to 0.24 nm in charged to uncharged networks. The charged network is soluble, as the box had fix dimensions this result in the maximum spacing. Thus the model characterize the swelling and de-swelling of the polymer chains well, as far as the fixed box size allows. To fully capture the swelling of the charged chains the system would have to be coupled to a water reservoir, that allow the charged chains to dispense.

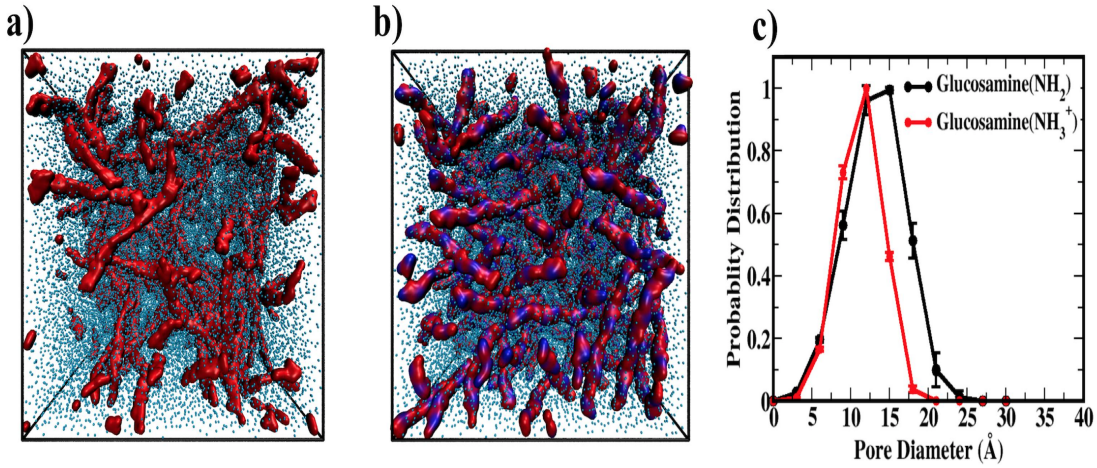

Figure 2.18: Simulation snapshots and pore-size distributions of chitosan networks with 100 polymers of DP=12 and 32 water molecules/monomer. The simulation snapshots show the chitosan backbone (A,B,C beads) in red, charged glucosamine A in blue, and water molecules as blue dots for (a) Glucosamine(NH_2) (b) Glucosamine(NH_3^+).

2.7 Conclusion

Cellulose can be chemically modified to form various derivatives which poses the desired properties for specific application. In this chapter, we have shown that a combination of all-atom simulations and a systematic coarse grained model based on the all-atom interactions, can be used to efficiently and precisely predict the effect of the modifications on the aggregates. Chemical alterations such as substitution of one hydroxyl group with methyl groups or fluorine atoms were modeled to study the self-assembly of these polymer systems by different functional groups. The CG model revealed insights into properties of the network such as the pore size, end-to-end distance and the minimum distances between the polymers.

Chapter 3

A multiscale model for hydrophobically modified chitosan

3.1 Introduction

Chitosan is a polymer of major interest to researchers and clinicians for developing therapeutic hydrogels. It is derived from naturally abundant chitin and is a bio-compatible, nontoxic polymer that is degradable by human digestive enzymes[20] . In addition, the presence of the primary amine groups on the glucosamine monomers provide a site for the chemical modification, which has been extensively exploited to tailor the kinetics of drug release[65,66] . As a result, a variety of chitosan-based formulations have been developed for oral, ophthalmic, and transdermal applications,[20,67,68,69] several of which have received FDA approval, demonstrating clear feasibility of these materials toward clinical translation.

In this thesis acetyl, butanoyl, and heptanoyl moieties as shown in Figure 3.1 were chosen for chitosan modification as they represent similar but increasingly hydrophobic modifications and therefore allow us to study systematically their effect on the properties of modified chitosan polymers and network.

To understand how these above mentioned chemical modifications govern the morphology of the hydrogel. It is necessary to model chitosan hydrogels across a large length and time scale, where a high number of long chitosan polymer chains, and many water molecules and their dynamic interplay can be simulated, for a sufficient time to render a physically accurate representation of these systems. This is not possible with all-atom simulations. We therefore resolved to adopt a CG modeling procedure that was

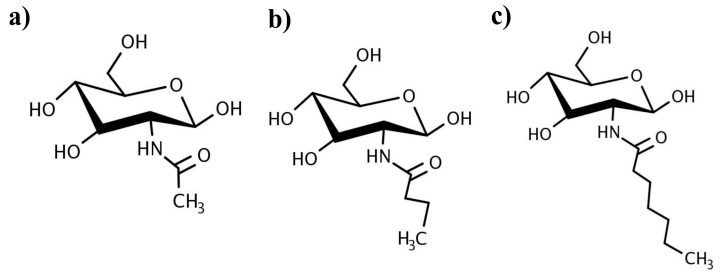

Figure 3.1: Chemical structure of (a). N-acetyl glucosamine, (b) N-butyl glucosamine, and (c) N-heptyl glucosamine.

informed by the results of the all-atom simulations and that has been shown to capture the behavior of the polysaccharide-based hydrogel[70] .

In this chapter, the development and validation of a bottom-up CG model for the modified chitosan molecules is described. An atomistic simulations were performed to obtain the CG potentials for polymer-polymer and polymer-solvent interactions. As shown in chapter 2, to obtain a predictive CG model, the MS-CG[30] procedure was used to obtain the non-bonded interaction while BI[31] was used for bonded interactions. The model is validated by comparing RDFs and end-to-end-distances and radius of gyration against all atom data.

3.2 Methods

3.2.1 All-atom simulations

For the development of the CG interactions, all-atom MD simulations of the following systems were performed using Gromacs 5.1.2[41] .

1. 10 chitosan chains with degree of polymerization (DP) = 16 and 0% acetylation, with 200 water molecules per oligosaccharide, *i.e.* 2000 water molecules in total.

2. 10 acetylated chitosan chains with DP = 16 and 200 water molecules per oligosaccharide for degrees of acetylation of 16 %, 24 %, 32%, and 50 %.

3. 10 chitosan chains with DP = 16 and 200 water molecules per oligosaccharide with degrees of butylation 16 %, 24%, 32%, and 40 %.

4. 10 chitosan chains with DP = 16 and 200 water molecules per oligosaccharides with degrees of heptylation 8 %, 16%, 20%, and 24 %.

5. 50 DOX molecules with 10 water molecules per DOX.

6. 50 GEM molecules with 10 water molecules per GEM.

7. Systems 1 to 4 with the addition of 10 DOX or 10 GEM molecules.

The acetyl, butyl, or heptyl modifications in systems (2-4) were uniformly distributed along the chains.

In addition, single polymers with DP=16 in a water box were simulated to compare the end-to-end distance and radius of gyration between atomistic and CG simulations. The computational procedure used here was similar that described in Chapter 2. Parameter for the butanoyl and heptnoyl modifications and the drug molecules were obtained from the gaff force field[46] . Partial charges for the modified glucosamine monomer, DOX and GEM were obtained by the same way mentioned in Chapter 2. Other parameter for the carbohydrates were taken from the modified GLYCAM06$^{\mathrm{TIP5P}}_{\mathrm{OSMOr14}}$[26,27] force-field with the TIP5P[28] as water model.

3.3 CG Model

As similar to previous chapter 2, glucosamine monomers were mapped to three CG sites - A, B and C - as shown in Figure 3.2 using center-of-mass (COM) mapping. Acetyl or butyl or heptyl modifications were mapped to one, two or three CG M sites, as also shown in Figure 3.2. DOX was mapped to 11 CG sites, using 9 distinct bead types, to produce a structure that can capture the planar geometry of the DOX molecule. Four distinct beads were used to model GEM. Water molecules are mapped to one CG site located at its center of geometry (COG).

Potentials for bond, angle and dihedral interactions, as well as specific non-bonded 1-3 and 1-4 interactions were obtained from Boltzmann inversion[31] , using the VOTCA package[59,60] . The non-bonded interaction were obtained using the MS-CG Method[30] using the rerun trajectories with separate solute-solute, solute-solvent and solvent-solvent interactions. All the bonded and intra-molecular interaction were excluded during the MS-CG procedure.

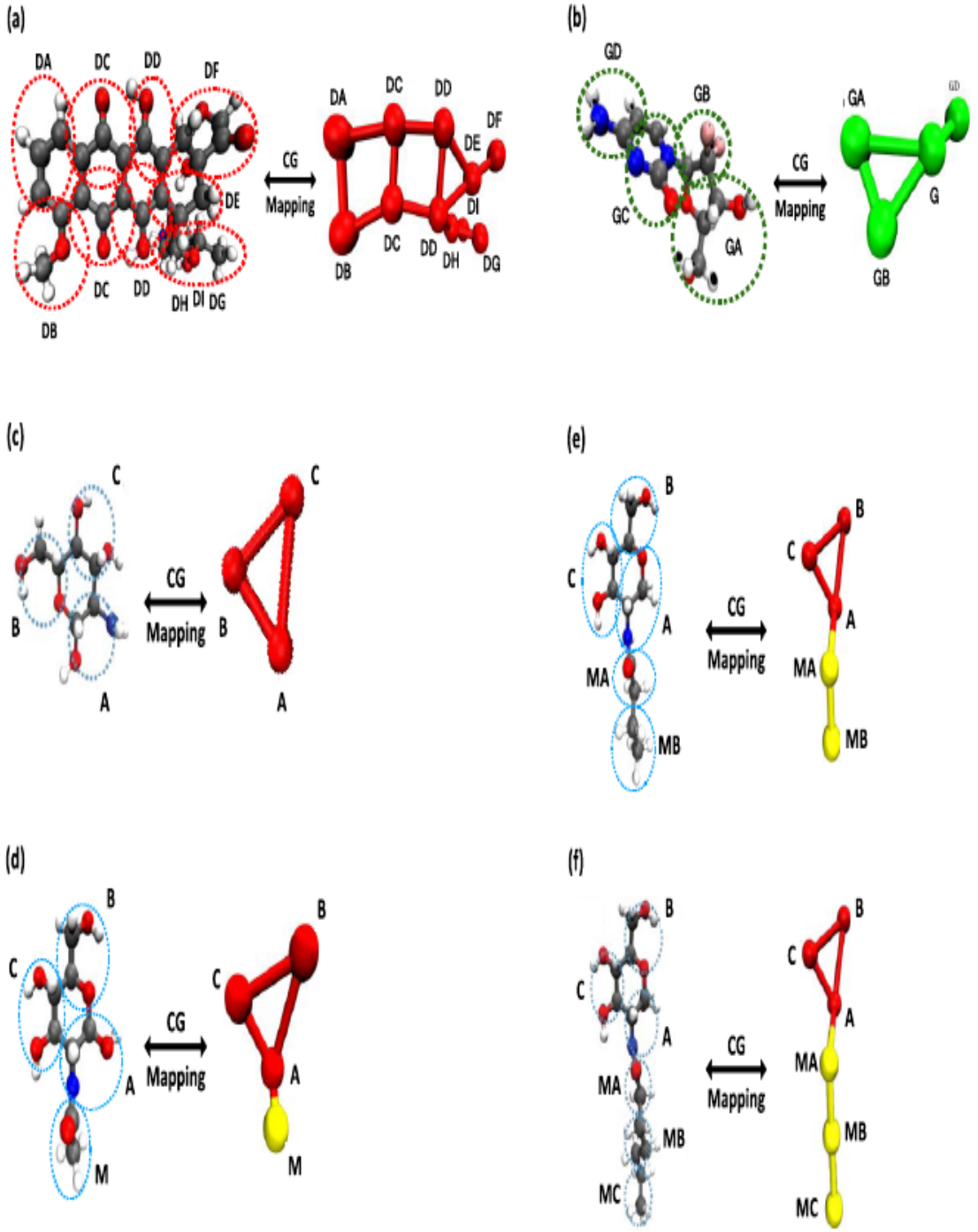

Figure 3.2: All-atom and coarse-grained representations of (a) DOX, (b) GEM, (c) unmodified glucosamine monomer, (d) acetyl-glucosamine, (e) butanoyl-glucosamine, and (f) heptanoyl-glucosamine.

3.3.1 CG Simulations

CG simulations of systems corresponding to the all-atom systems 1-7 were performed with Gromacs 4.6.4[41] .

Initial structures were obtained from the corresponding atomistic representations. CG simulations for each system were performed in the NVT ensemble using the Leap-Frog integrator[56] with the Nosé-Hoover Thermostat[51,52] and a time step of 1 fs. A cut-off 1.4 nm was used for all the CG simulations. Simulations were run for 10ns to obtain equilibrated RDFs, angle distributions, average end-to-end distances and radius of gyration to compare between all-atom and CG simulation.

3.4 Model validation

To evaluate the CG model's ability to reproduce the local molecular structure of the solution, as well as the overall tendency of chitosan molecules to aggregate, we compare the radial distribution functions (RDFs) obtained from the CG simulations of chitosan chains with DP = 16 to those obtained in the atomistic simulations of the same system. The ensemble of RDFs between all pairs of CG sites was calculated and offers information both on the short range molecular structure, reflected in the position and magnitude of the peaks at short distances, and the overall aggregation trends of the chitosan chains, visible in the long range behavior of the curve. were compared to obtain a measure of the solution structure.. To characterize the conformation of single chitosan chains, angle distributions and end-to-end distances were also calculated.
First, the RDFs obtained from CG simulations of chitosan chains with low degree of modification, $\chi_{Ac} = 16\%$ (Figure 3.3), $\chi_{But} = 16\%$ (Figure 3.4) , and $\chi_{Hep} = 8\%$ (Figure 3.5) aligned well with the corresponding RDFs obtained from atomistic simulations . Of particular notice is the agreement between CG and all-atom data for the RDFs between water beads and the various CG sites of chitosan chains Figure 3.6, since carbohydrate-water interactions were previously found to be highly sensitive to long range perturbations and sampling issues[27] . The RDFs for all other pairs of CG sites obtained for modified chitosan chains with low χ from CG and atomistic simulations also showed good resemblance with each other.

For the bonded interactions, the most flexible degrees of freedom of polysaccharide systems are those of the glycosidic bonds. In the present CG model, the conformations of the glycosidic dihedral angles, ϕ and ψ are reflected by the angles $B_i - A_i - C_{i+1}$ and

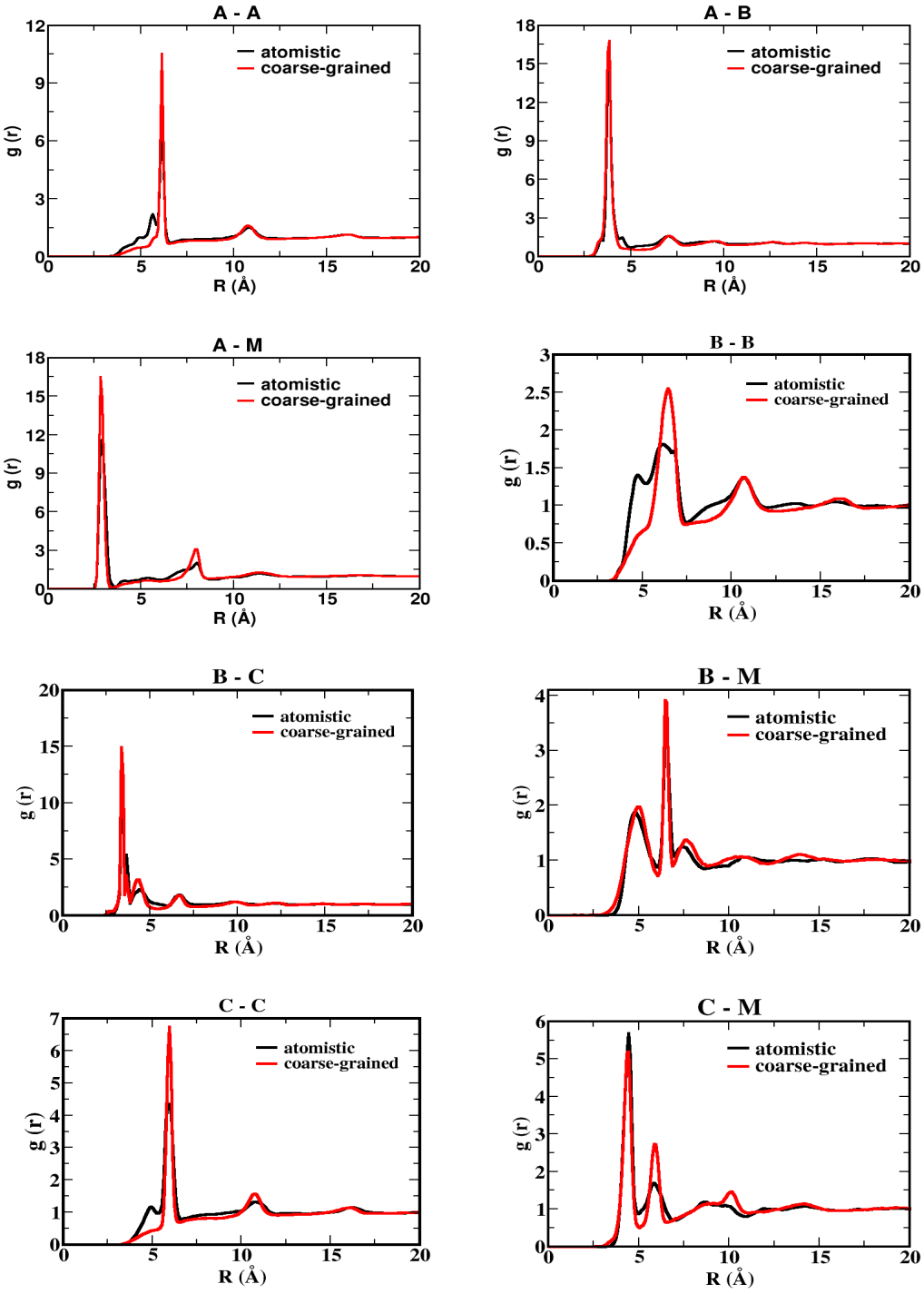

Figure 3.3: Comparison of CG and atomistic RDFs of the distances between CG (A, B, C, M for χ_{Ac}=16% . Note: A, B, and C beads map the GlcN monomers, whereas M map the modification(acetyl) group.

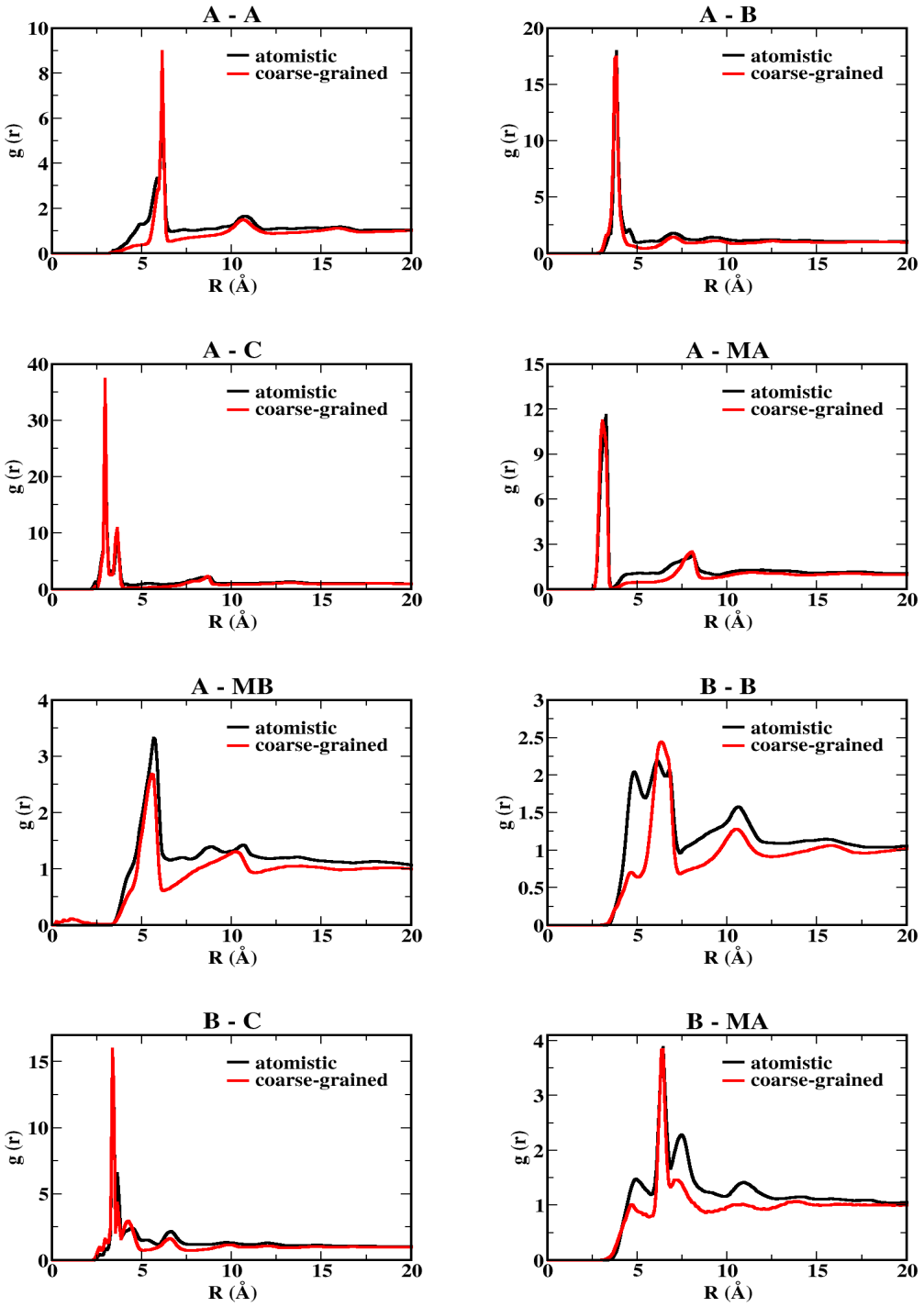

Figure 3.4: Comparison of CG and atomistic RDFs of the distances between CG (A, B, C, M for χ_{But}=16% . Note: A, B, and C beads map the GlcN monomers, whereas MA and MB map the modification groups

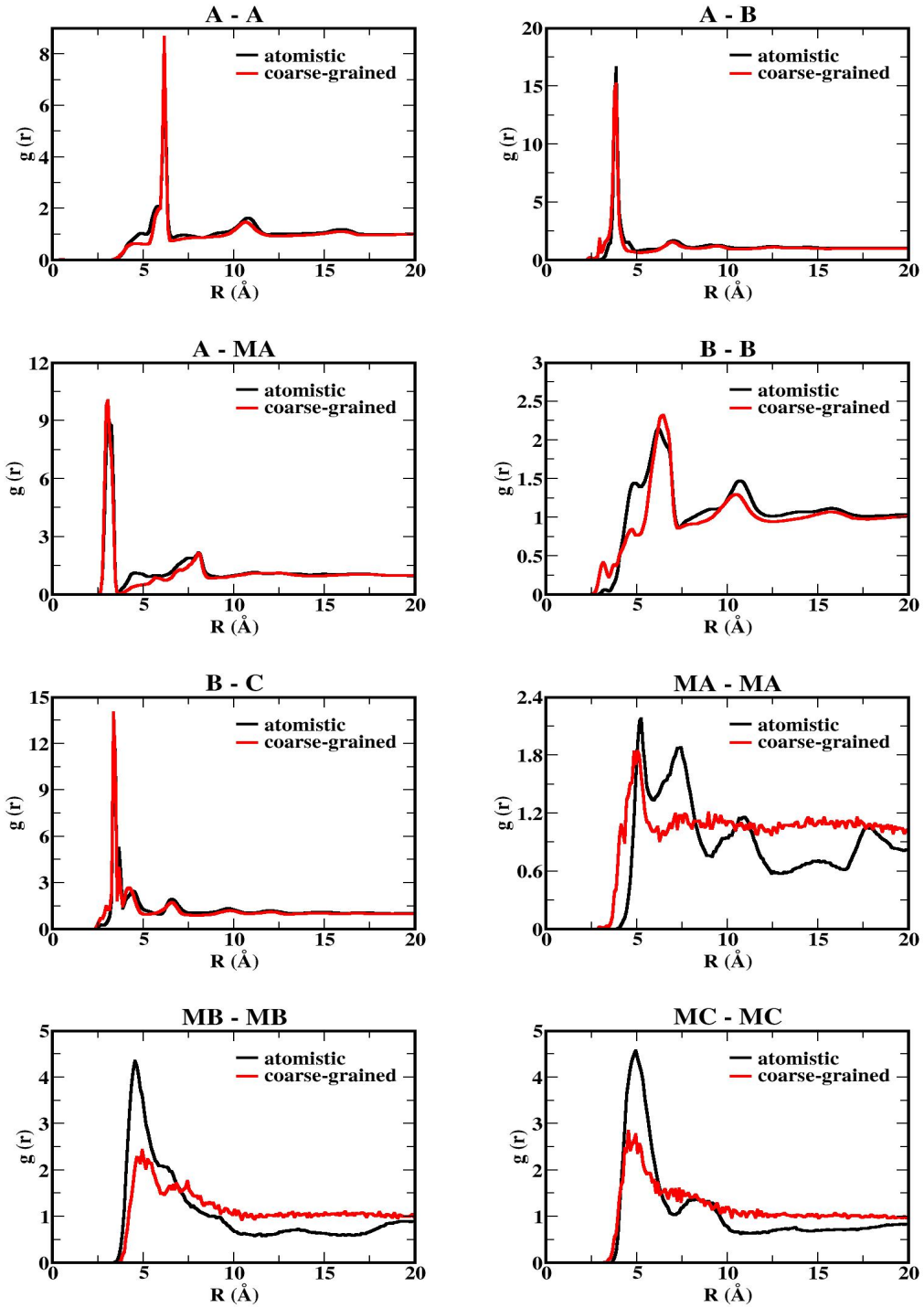

Figure 3.5: Comparison of CG and atomistic RDFs of the distances between CG (A, B, C, M for χ_{Hep}=8% . Note: A, B, and C beads map the GlcN monomers, whereas MA, MB, and MC map the modification groups

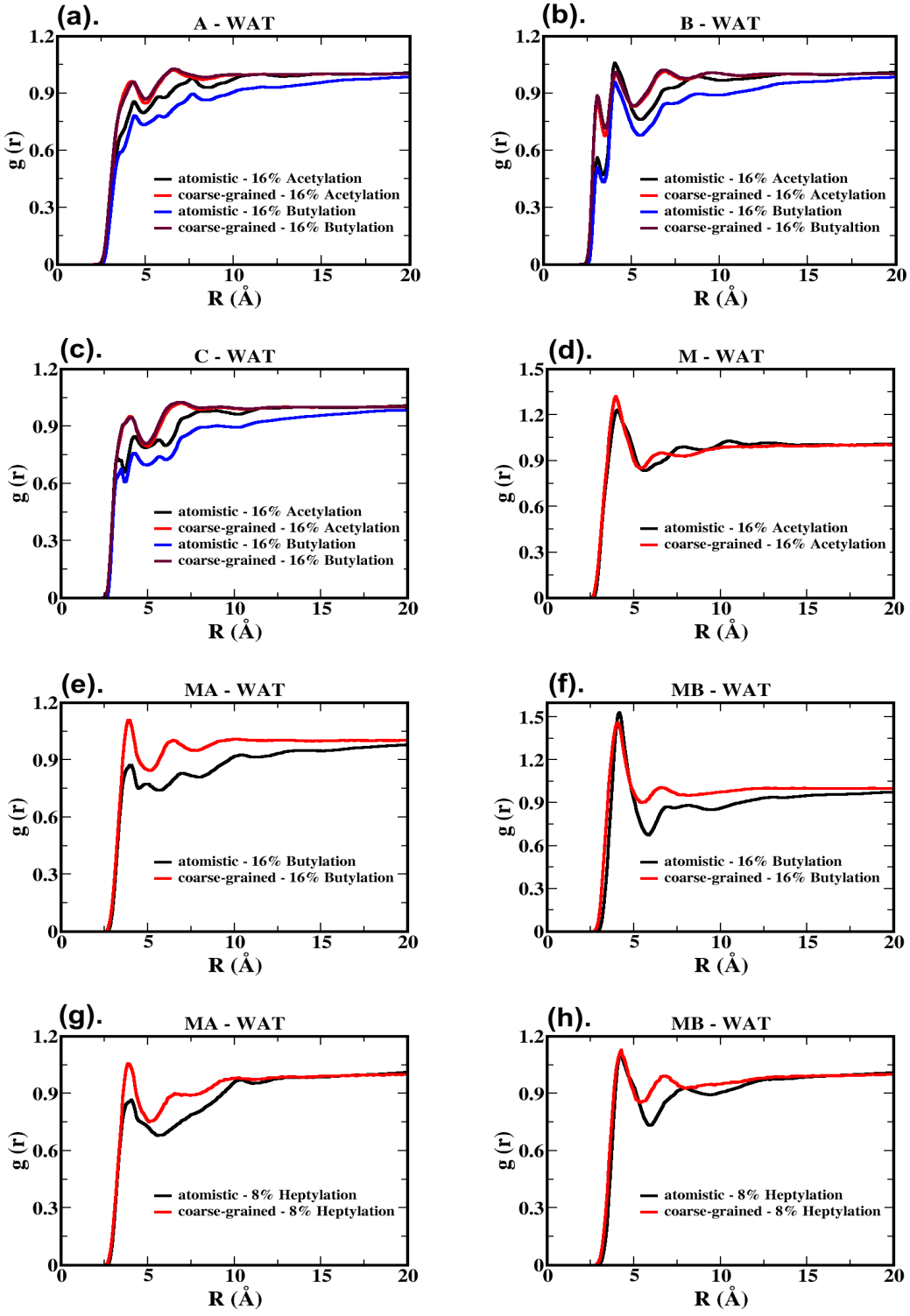

Figure 3.6: RDFs for interaction involved with CG site type WAT with other beads for (a),(b),(c) and (d) 16 acetylation and (e), (f) for 16 % butylation.

$A_i - C_{i+1} - A_{i+1}$ as well as the dihedral angle $B_i - A_i - C_{i+1} - B_{i+1}$. The probability distributions sampled for these angles in the all atom as well as simulation snapshots corresponding to the three minima in the $\phi - \psi$ free energy landscape are shown in Figure 3.7. Both angle distributions show two distinct maxima, whereas in the atomistic system, the dihedral distribution has three maxima at -140°, 30° and 140°, corresponding to the three conformations shown in Figure 3.7.

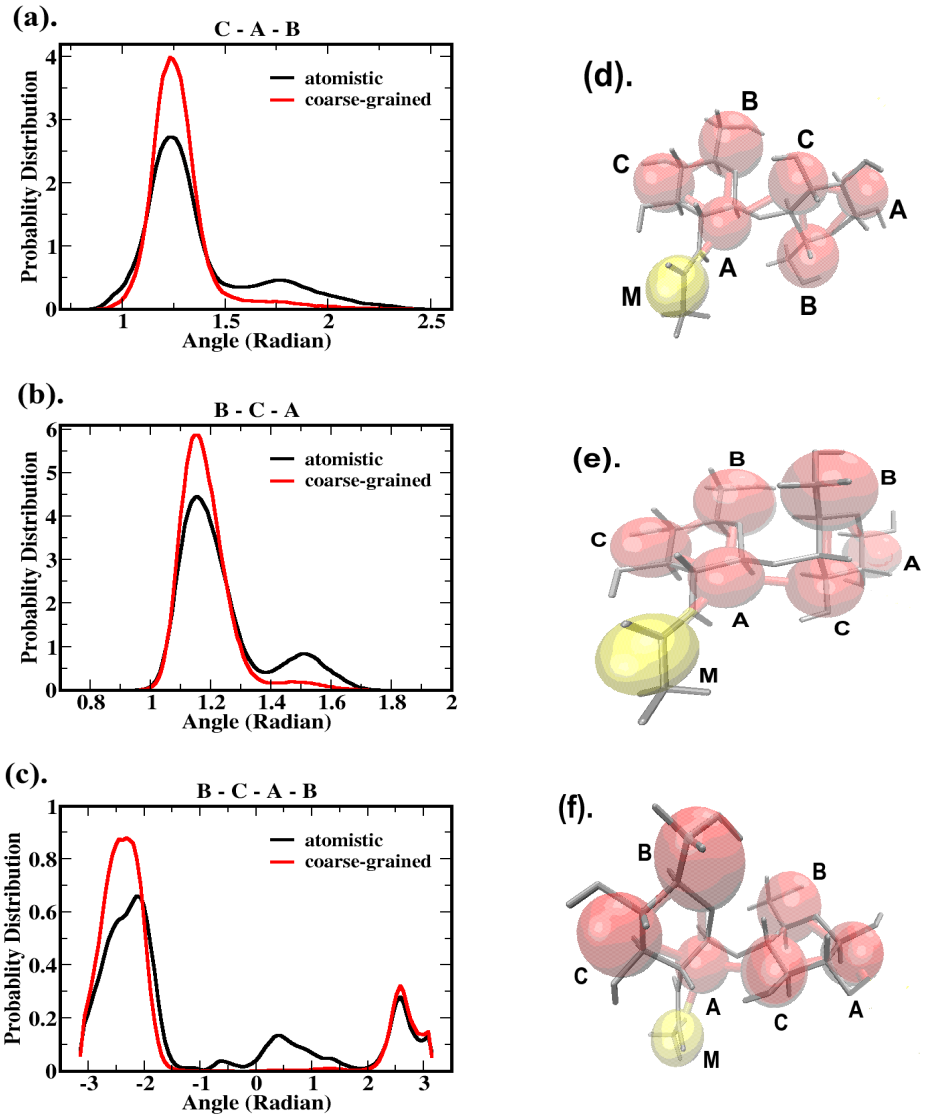

Figure 3.7: (a-c) Angle distributions in the atomistic and CG models; (d-f) molecular conformations corresponding to the three free energy minima of the $\phi - \psi$ dihedral angles. All-atom models are drawn as grey sticks, CG molecules as red (ABC) and yellow (M) beads.

A comparison of the atomistic and CG distributions shows that the CG model gives a good representation of the dominant conformation, but that the second energy minimum is under-represented in the CG model. This is a consequence of applying the inverse Boltzmann method without further iteration, which does not account for the effects of neighboring bonds and may therefore sometimes over-represents the stiffness of interaction potentials. However, the population of the second minimum is relatively small in the atomistic model, and will therefore only have a minor effect on the overall polymer conformation, as illustrated for example by the comparison of the end-to-end distances of the of the atomistic and CG oligosaccharides shown in Table 3.1.

	Atomistic		Coarse-Grained (CG)	
Modification	End-to-End distance(nm)	Radius of Gyration(nm)	End-to-End distance (nm)	Radius of Gyration (nm)
16% Acetylation	7.14 ± 0.35	2.33 ± 0.05	6.80 ± 0.87	2.19 ± 0.14
16% Butylation	7.11 ± 0.44	2.20 ± 0.08	5.95 ± 1.18	2.02 ± 0.19
8% Heptylation	5.83 ± 0.68	2.06 ± 0.09	5.94 ± 1.38	2.00 ± 0.21

Table 3.1: Table showing comparison between atomistic and CG end-to-end distance and radius of gyration for (a). 16% acetylation ,(b). 16% Butylation and (c). 16% Heptylation

For higher degrees of modification however, it becomes apparent, that the CG RDFs for the hydrophobic modifications become progressively worse. The RDFs of the M-beads for 32% acetylated chitosan, shown in Figure 3.8a), exhibit a strongly exaggerated peak at short distances. Similarly, the RDFs for 32% butyl modification shown in Figure 3.8b) and c) for MA-MA and MB-MB interactions differ between the atomistic and CG systems. Whereas the MB-MB CG RDFs in Figure 3.8c) capture the overall atomistic behavior, although with a reduced magnitude of the short distance peaks, the MA-MA RDFs differ substantially at short distances, and show un-physically close contacts. The all-atom RDF on the other hand contains a number of irregular peaks at all distances, which indicates the formation of clusters and suggests that there may be problems for accurately sampling the distribution of atomistic forces as a result of the strong interactions between the hydrophobic modifications. Because previously potentials obtained from a similar coarse-graining procedure were found to be transferable to different concentrations,[70] we tested the use of M-bead interaction potentials obtained at a lower degree of acetylation $\chi = 16\%$, where they performed well. The results are shown in

Figure3.8 a) together with those from the native CG model.

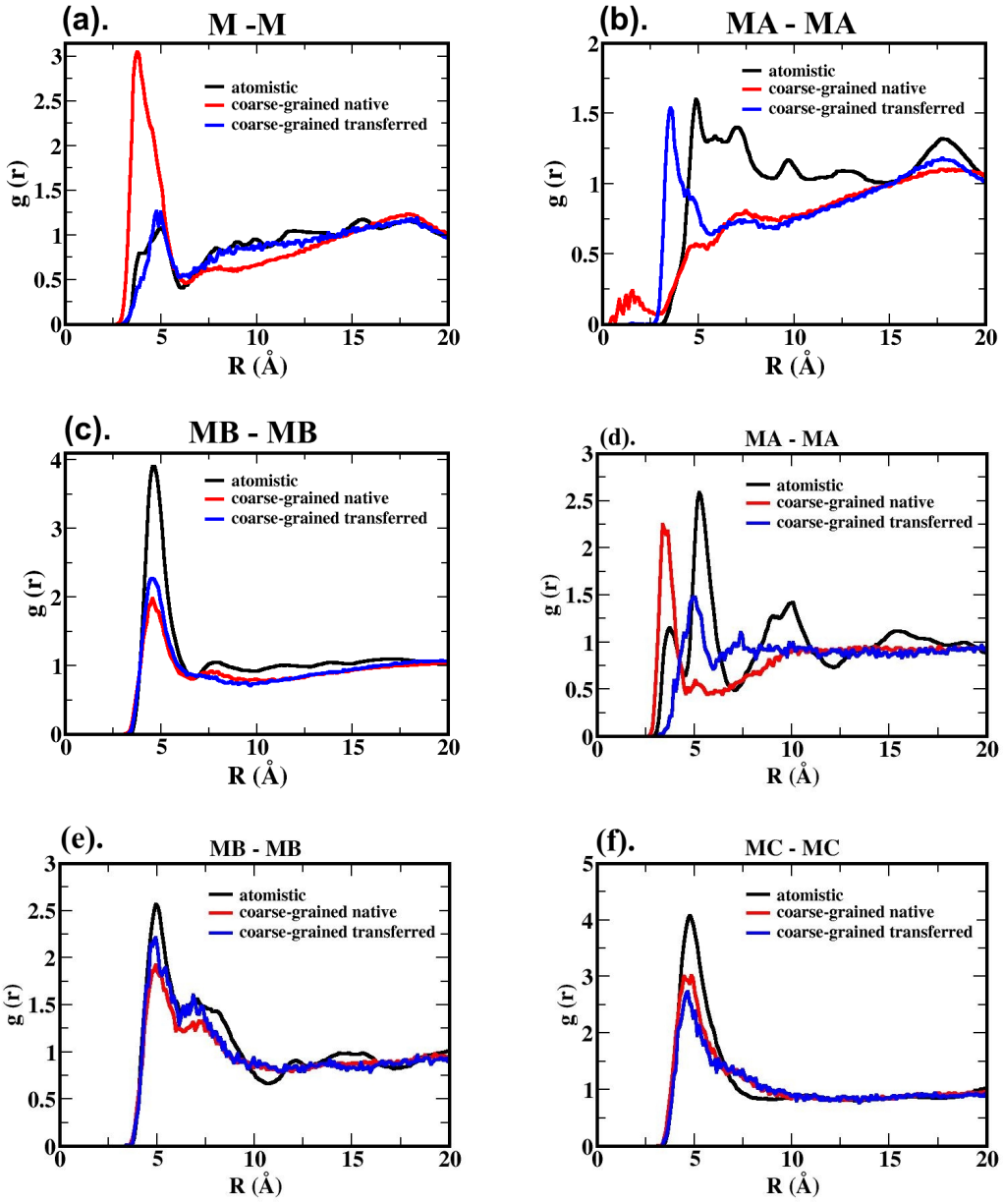

Figure 3.8: RDFs of the distances between modification beads: (a) M-M beads in acetyl-chitosan with χAc = 32%; (b) MA-MA and (c) MB-MB beads in butanoyl-chitosan with χBut = 32%; and (d) MA-MA, (e) MB-MB, and (f) MC-MC beads in heptanoyl-chitosan with χHep = 16%. The RDFs obtained from the atomistic, native CG, and CG with transferred potential models are in black, red, and blue, respectively.

Comparison shows, that the transferred potentials significantly improve the over-aggregation of the M-beads for acetylated chitosan, and the CG RDF for M-M inter-

actions now closely resembles the atomistic one. Applying the same approach of using interaction potential from 16% butylated for 32% butylated, the CG RDF for MA-MA interactions also shows significantly reduced clustering and now resembles that of the acetylated chitosan, whereas the MB-MB interactions (Figure 3.8c) are unchanged compared to the CG model obtained explicitly for χ = 32%. All other RDFs remain unchanged for the transferred modification interactions. Analogous results were found for the heptyl modified chitosan chains. Because the heptyl modifications are more hydrophobic, effects of clustering was already seen for χ=16% modification, so that the CG interaction potential were obtained for χ=8% heptylation and transferred to χ=16% and χ=24% heptylation. The comparison of RDFs for the MA-MA interactions in heptanoyl-chitosan chains again shows a better representation of the short range features in the atomistic RDF by the transferred interaction potentials as shown in Figure 3.8d). MB-MB and MC-MC interactions on the other hand, remain unchanged Figure 3.8e) & f). Similarly, the RDFs between all other CG sites remain unchanged when the transferred interaction potentials are used.

Collectively, these results showed that transferring the interaction potentials obtained at lower values of χ to systems at higher χ improves the agreement between atomistic and CG simulations for the hydrophobic sites, without altering the interactions between other CG sites. Accordingly, the CG interaction potentials obtained at χAc and χBut of 16% and χHep of 8% were applied in the rest of this study to model the systems with higher χ. Notably, this approach has the additional advantage of rendering the model more versatile for constructing polysaccharides with varying degrees of modification and that can be arranged in different patterns.

Next, the performance of the chitosan model for higher degrees of polymerization and for systems with a higher water content was tested. As a first step, the transferability to systems with higher water content, *i.e.* lower chitosan concentration, was explicitly tested for chitosan with DP=16. As expected from related systems[27] , the RDFs obtained for chitosan with 32 water molecules per chitosan monomer using CG interactions transferred from a system with 12 water molecules per chitosan monomer, were found to very closely resemble the native CG model produced at the lower chitosan concentration in Figure 3.9.

Then, a system of larger polysaccharides with DP=50 and 32 water molecules per monomer is constructed and simulated with the same CG model with respect to DP and water concentration. For most interactions, the RDFs of the longer chains, shown

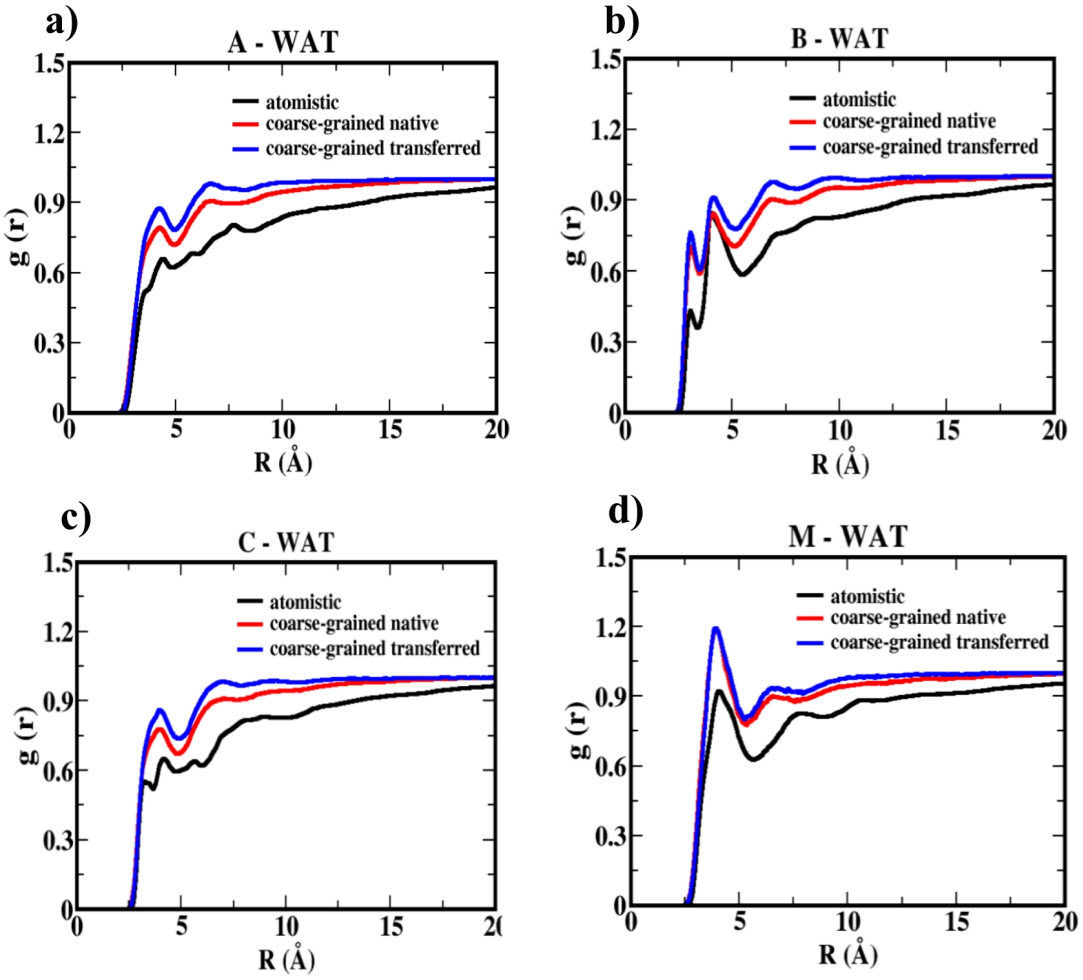

Figure 3.9: RDFs for 16% acetylation comparing all-atom results with DP=16 and 32 waters/monomer (black), CG results with DP=16 and 32 waters/monomer (red) and transferred CG interaction potential from DP=16 and 12 waters/monomer (blue).

in Figure 3.10, strongly resemble those obtained for the 16-mers. Only the short range peaks of the solute-solute interactions, which correspond to bonded neighbors, increased in intensity for the higher DP, because there are more bonded neighbors.

3.5 CG model for drug

A CG FFs was developed for system 5 and 6 by following the same procedure as described in the method section. A feasible mapping schemes were used to map DOX and GEM to obtain CG representation as compared to all-atom representation. For DOX, 9 distinct bead types were used to have a planar structure in the chosen mapping which resemble

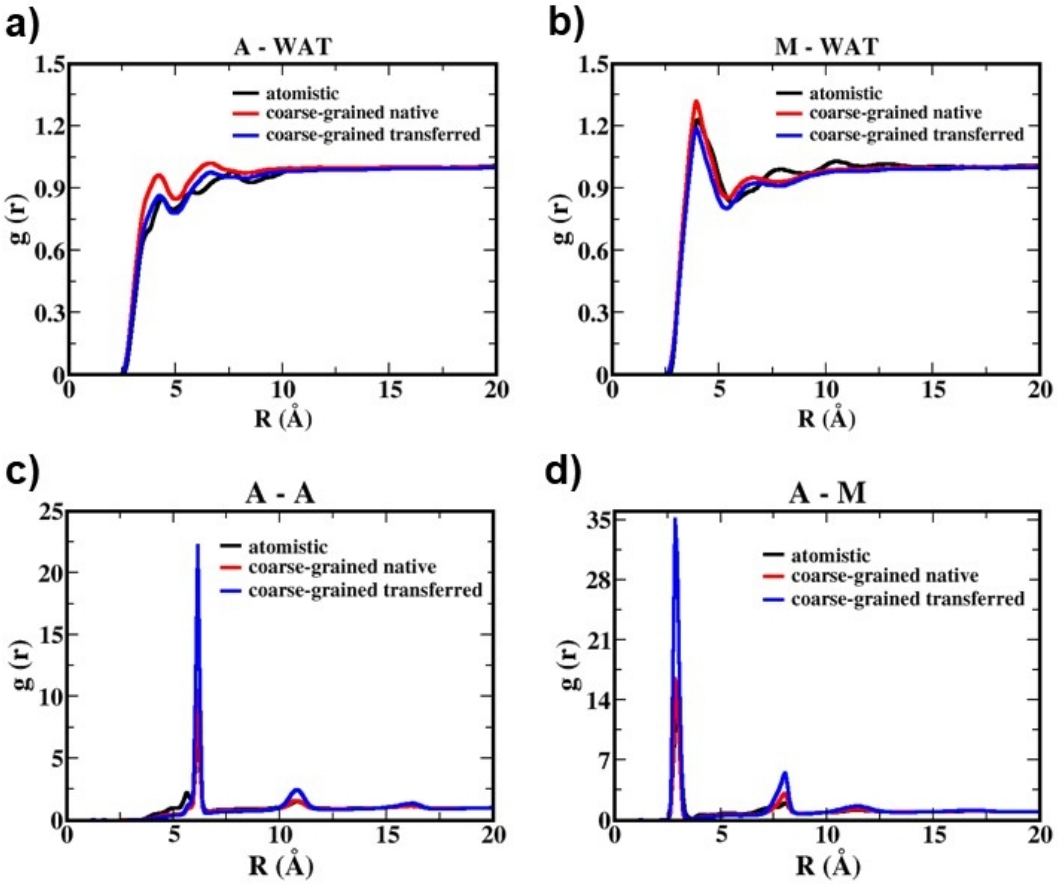

Figure 3.10: RDFs for 16% acetylation comparing all-atom results with DP=16 and 12 waters/monomer (black), CG results with DP=16 and 12 waters/monomer (red) and CG results for DP=50 and 32 waters/monomer (blue).

to its atomistic structure as shown in Figure 3.2, with a total number of 11 beads. Different combination of bonds, angles and dihedrals were tested. In the final model, the bonds DA-DB, DA-DC$_i$, DB-DC$_{i+1}$, DC$_i$-DC$_{i+1}$, DC$_i$-DD$_i$, DC$_{i+1}$-DD$_{i+1}$, DD$_i$-DE, DD$_{i+1}$-DE, DE-DF, DD$_{i+1}$-DG, DG-DH, DG-DI, and DI-DH are used. The four angles, DC2-DD2-DG, DD1-DE-DF, DD2-DG-DH and DE-DD2-DG and five dihedral, DC1-DD1-DD2-DG, DC2-DD2-DG-DH, DD2-DG-DH-DI, DF-DE-DD2-DG, and DE-DD2-DG-DH are used. For the CG representation of GEM, four distinct bead types were used as presented in Figure 3.2. Six different bonds namely GA-GB, GB-GC, GC-GD, GA-GC and two explicit 1-3 intra-molecular interactions GA-GD and GB-GD were used. Simulation snapshot of DOX in water and GEM in water are shown in Figure 3.11.

Like for the carbohydrates, the CG-FFs was validated by comparing the RDFs for

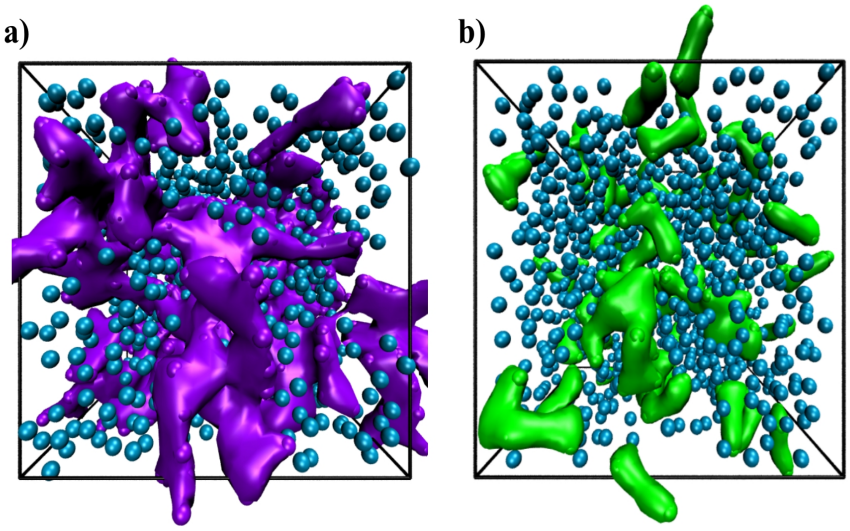

Figure 3.11: Simulation snapshots of DOX and GEM with 10 water molecules/molecules. The simulation snapshots show DOX in purple, GEM in green and water molecules as blue dots for a) DOX in water (b) GEM in water

both the drugs. RDFs show overall good agreement with the atomistic RDFs as shown for two example in Figure 3.12.

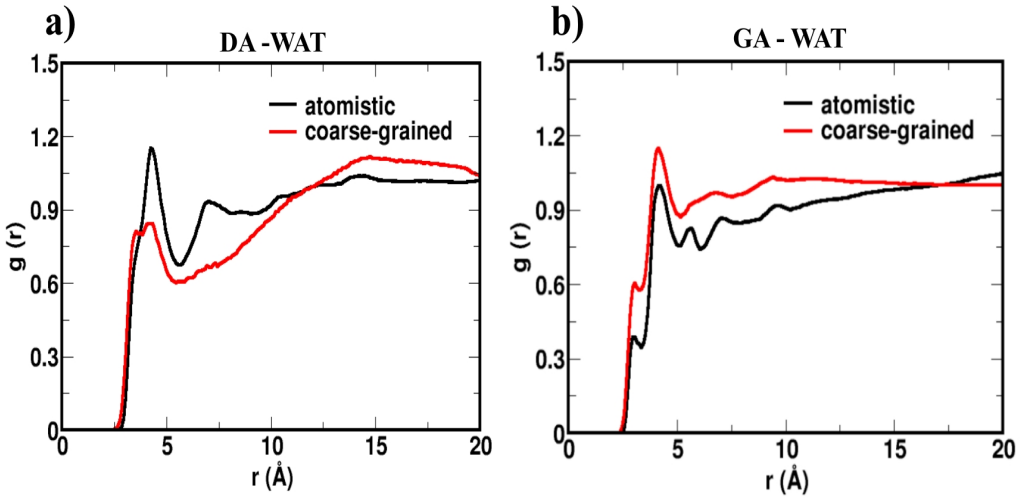

Figure 3.12: RDFs for interaction of DOX and GEM with water (a). DA bead from DOX with water, (b) GA bead from GEM with water

The other RDFs show a similar resemblance with atomistic RDFs. The developed model was used to provide drug-drug CG interaction potential for futher simulation. Along with that, system 1-4 were simulated with 10 DOX and 10 GEM molecules sepa-

rately to obtain drug-chitosan CG interaction potential.

3.6 Conclusion

In this chapter, a CG model for chitosan with three different hydrophobic modifications was introduced and analyzed. First, all-atom simulations of the different chitosan solutions were performed and CG interactions potential were obtained from MS-CG procedure for non-bonded and BI for bonded interaction to study the polymer network at larger length and time scale. The CG model can reproduce structural data of the all-atom systems, such as details of the RDF, angle distribution and end-to-end distances well. In addition we showed that it can be transferred to systems with high water content and to molecules with high degree of hydrophobic modification. A CG model of the two drugs namely DOX and GEM was also proposed, showing good resemblance with their atomistic counterpart.

Chapter 4

Effect of hydrophobic modifications on chitosan hydrogel properties

4.1 Introduction

This chapter describes the application of the CG model developed in Chapter 3 to obtain equilibrated structures of chitosan hydrogels under different conditions. We had analyzed the effect of modification type, degree and pattern as well as water content in the gel on the network structure. The network structure were equilibrated and then quantitatively characterized in terms of the pore sizes, end to end distance of the polymers and average number of contacts between the modifications. Finally the effect of pattern of modification on the network structure was also analyzed and the structure formed compared to those corresponding to the uniformly-spaced modifications. The CG-FFs developed in previous chapter 3 was used for longer polymer *i.e.* DP =50. Because no correlation between the gel fraction and the molecular weight of chitosan exist and simulating chitosan chains with DP $>$ 50 would lead to long computational time, hence considered unnecessary.

In chitosan hydrogels, usually both modification and their patterns are governed by the monomers and the reagents utilized for chemical modification, as well as by the structure of the polymer chain in solution as it evolves through the course of the chemical modification(χ). Usually, the anhydrides used in the modification process are amphiphilic molecules, their tendency to form aggregates will increase with increasing hydrophobic fraction. Whereas χ can be easily measured, evaluating the modification patterns is much more challenging, and it is often assumed to be random. However, other

distributions of the modification groups, an evenly spaced or a blocky pattern can also be envisioned, and their presence can have profound effect on the macroscopic behaviors of the polymer. A block-type polymer pattern is more favored during hydrophobic modifications of the anhydrides (like acetic, butanoic and heptanoic). As, the probability of creating a modification next to an already modified(hydrophobic monomers) site may becomes larger, leading to clustered modificationss in aqueous acidic media.

It is likely that both χ and the modification pattern, in fact, govern the aggregation of polymer chains in solution; in particular, chain aggregation is likely to be promoted by blocky modification patterns as opposed to a random distribution along the polymer chain[71,72,73] . While such an effect cannot be easily controlled or measured in experiments, computational models have full control over the distribution of modifications, and can therefore explore the effect of different patterns on the hydrogel structure. To evaluate this effect of the modification pattern on the network structure and the molecular interactions, chitosan chains modified with two different patterns, namely, evenly spaced modifications (i.e., two neighbor modification groups are separated by a number of unmodified monomers) and blocky (i.e., clusters of four modified monomers separated by a number of unmodified monomers), were constructed to be simulated and analyzed.

4.2 Methods: CG network model

The larger hydrogel systems were also initially constructed with atomistic resolution, following the same steps as for the shorter chains (described in Chapter 3). Starting structures for the CG simulations were obtained from 10 ns atomistic NPT simulations, to obtain the corresponding box-sizes. Then the systems were mapped to their CG representation using the VOTCA software[59,60] . The large hydrogel structures were simulated for 100 ns in NVT. Data from the last 10 ns was used for analysis.

CG simulations of the following systems were performed with Gromacs 4.6.4[41] :

i. 50 chitosan chains with DP=50 and 80,000 water beads, corresponding to 1600 water molecules per polymer chain (32 water molecules per monomer), with evenly spaced modifications.

ii. 50 chitosan chains with DP=50 and 80,000 water beads, with modifications grouped in blocks of four.

iii. 20 chitosan chains with DP=50 and 100,000 water beads or 5000 water molecules per polymer chain (100 water molecules per monomer), with evenly spaced modifications.

iv. 20 chitosan chains with DP=50 and 100,000 water beads, with modifications grouped in blocks of four.

The hydrogel structures were characterized by the distribution of pore sizes, following the same protocol mentioned in chapter 2. For each distribution, three snapshots of the network structures at 5 ns intervals were analyzed.

4.3 Low water content

Simulation snapshots of dense chitosan networks with 50 polymers with DP=50 and 80,000 CG water molecules are presented in Figure 4.1. These polymers have evenly spaced acetyl, butyl and heptyl modifications. For all systems, the chitosan polymers appear to be overall uniformly distributed throughout the box. Analysis of the pore sizes in these networks results in a similar picture. The pore size distributions, also shown in Figure 4.1, reveal no differences between the different modifications, all showing a relatively narrow distribution with most pore diameters at 1.2 nm.

Though no measurable large scale differences in the network structure are found, inspection of the simulation snapshots suggest that the more hydrophobic modifications form local clusters. For a more local picture of the molecular interactions within the networks we have characterized the number of contacts formed between the hydrophobic modifications, as summarized in Table 4.1. For the acetyl modifications the all contacts of M beads have been counted, while butyl and heptyl the number of contacts formed by MB or MC beads, respectively, with any other modification beads were counted.

As one would expect, the total number of contacts increases with higher χ and for larger modifications, both of which correspond to a higher total number of modification beads in the network. For acetyl chitosan, the M beads form on average only 28 ± 7 contacts for $\chi = 16\%$ but 273 ± 2 for $\chi = 50\%$. Similarly the contacts of the butyl MB beads increase from 433 ± 8 for $\chi = 16\%$ to 1002 ± 15 for $\chi = 32\%$, and the heptyl MC beads form 306 ± 9 contacts at $\chi = 8\%$ and 980 ± 18 contacts for $\chi = 24\%$. Put in relation to by the total number of modifications in the system, the trends remain similar: both butyl and heptyl form significantly more contacts per modification than acetyl, and in all cases the number of contacts increases with χ.

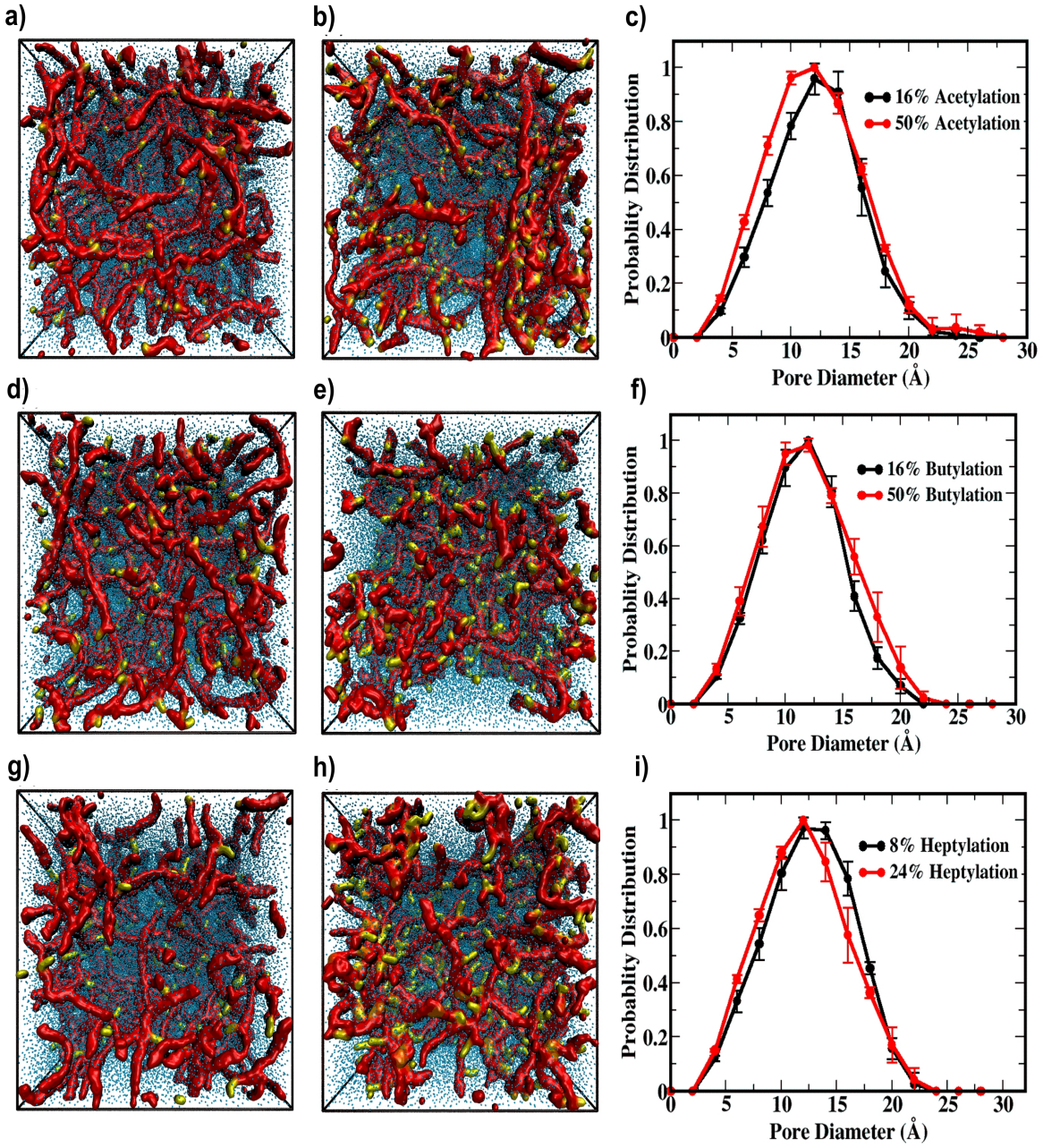

Figure 4.1: Simulation snapshots and pore-size distributions of chitosan networks with 50 polymers of DP=50 and 32 water molecules/monomer with (a-c) acetyl, (d-f) butyl and (g-i) heptyl modifications. The simulation snapshots show the chitosan backbone (A,B,C beads) in red, modifications (M, MA, MB, MC beads) in yellow and water mlecules as blue dots for (a) $\chi = 16\%$ acetylation (b) $\chi = 50\%$ acetylation, (d) $\chi = 16\%$ butylation, (e) $\chi = 32\%$ butylation, (g) $\chi = 8\%$ heptylation and (h) $\chi = 24\%$ heptylation.

	low water		high water	
Modification	total	per modification	total	per modification
16% Acetylation	28 ± 7	0.07 ± 0.02	4 ± 2	0.025 ± 0.012
50% Acetylation	273 ± 2	0.22 ± 0.002	46 ± 10	0.092 ± 0.02
16% Butylation	433 ± 8	1.08 ± 0.02	165 ± 3	0.41 ± 0.01
32% Butylation	1002 ± 15	1.25 ± 0.01	561 ± 10	1.03 ± 0.06
8% Heptylation	306 ± 9	1.53 ± 0.006	115 ± 5	1.44 ± 0.06
24% Heptylation	980 ± 18	1.63 ± 0.015	233 ± 7	0.97 ± 0.03

Table 4.1: Number of contacts between modification beads formed in the chitosan networks

Finally, the end-to-end distance can provide insight as to the effect of the modifications and of the interactions within the network on the conformations of the polysaccharides. The data for single polymers with different modifications and different χ is summarized in Table 4.2 and simulation snapshots in Figure 4.2. The addition of acetyl modifications barely affect the conformational space of the polysaccharide. Butyl and heptyl modifications on the other hand lead to more compact polymers, with decreasing end-to-end distances when the degree of substitution is increased, consistent with the increased hydrophobicity of the molecules.

	Evenly-Spaced Pattern			Blocky Pattern	
Modification	single polymer	network 50 chains	network 20 chains	single polymer	network 20 chains
16% Acetylation	15.4 ± 3.6	14.6 ± 0.4	14.4 ± 0.6	12.10 ± 4.06	15.4 ± 0.6
32% Acetylation		15.1 ± 0.2	15.4 ± 0.7		15.4 ± 0.6
50% Acetylation	15.9 ± 4.2	16.2 ± 0.3	16.1 ± 0.9	16.29 ± 3.92	15.7 ± 0.6
16% Butylation	10.2 ± 5.1	12.9 ± 0.5	12.7 ± 0.8	13.68 ± 3.65	13.4 ± 0.6
24% Butylation		11.8 ± 0.3	10.4 ± 0.5		13.0 ± 0.4
32% Butylation	8.7 ± 3.4	9.0 ± 0.3	5.6 ± 0.4	10.84 ± 3.66	10.2 ± 0.3
8% Heptylation	13.2 ± 3.7	13.5 ± 0.5	13.1 ± 0.7	10.42 ± 3.78	13.0 ± 0.4
24% Heptylation	11.7 ± 3.7	11.8 ± 0.3	12.4 ± 0.9	9.94 ± 1.38	12.4 ± 1.1

Table 4.2: Polymer end-to-end distance for single polymers in solution and in the network. The errors represent one standard deviation.

The trends observed in the chitosan networks follow the same overall line as for the single polymer. For acetylated networks, the average end-to-end distance of the polymers increases slightly from 14.6 ± 0.4 nm to 16.2 ± 0.3 nm from 16% to 50% acetylation, which suggests that the contacts in the hydrogel favor alignment and there-

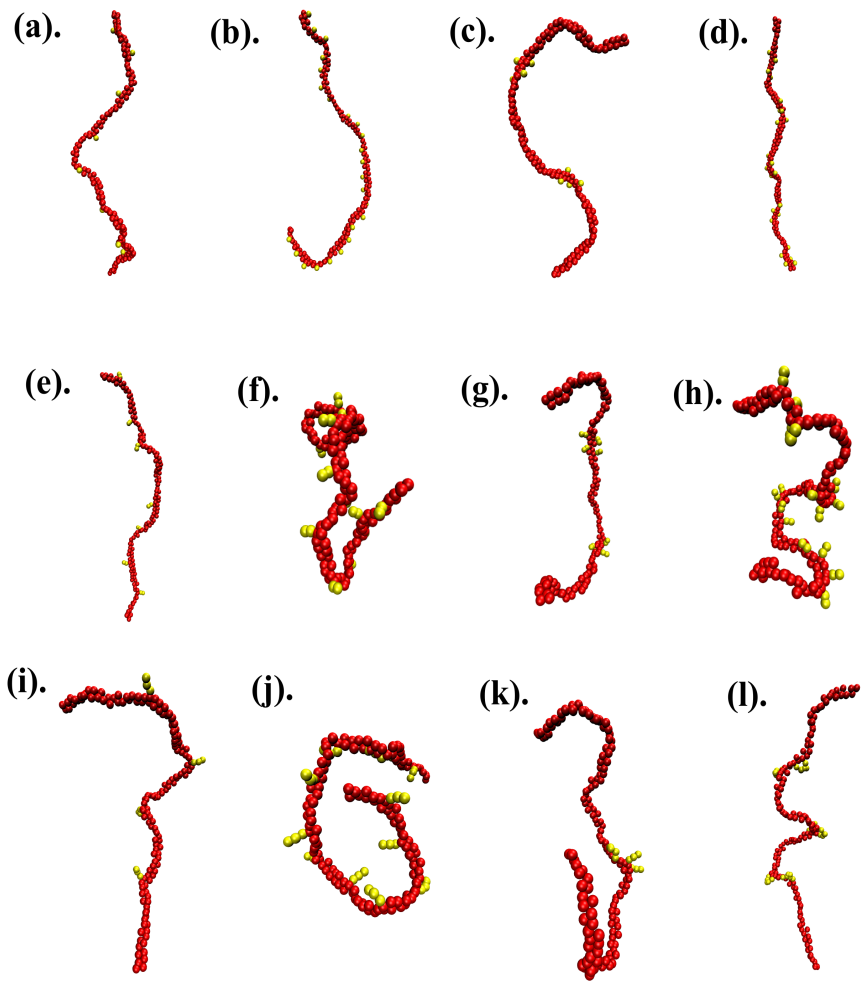

Figure 4.2: Simulation snapshots of single chitosan polymers with DP=50 and 100000 water molecules with (a-d) acetyl, (e-h) butyl and (i-l) heptyl modifications. The simulation snapshots show the chitosan backbone (A,B,C beads) in red, modifications (M, MA, MB, MC beads) in yellow (a) $\chi = 16\%$ acetylation with evenly-spaced pattern (b) $\chi = 50\%$ acetylation with evenly-spaced pattern, (c) $\chi = 16\%$ acetylation with blocky pattern (d) $\chi = 50\%$ acetylation with blocky pattern, (e) $\chi = 16\%$ butylation with evenly-spaced pattern, (f) $\chi = 32\%$ butylation with evenly-spaced pattern, (g) $\chi = 16\%$ butylation with blocky pattern, (h) $\chi = 32\%$ butylation with blocky pattern, (i) $\chi = 8\%$ heptylation with evenly-spaced pattern and (j) $\chi = 24\%$ heptylation with evenly-spaced pattern, (k) $\chi = 8\%$ heptylation with blocky pattern and (l) $\chi = 24\%$ heptylation with blocky pattern.

fore more linear conformation in the polymers. Both butyl and heptyl modified chitosan polysaccharides have more compact conformations with higher degrees of modification.

Thus overall, the observed network structure of the dense systems is very similar across different modification types, degrees and patterns. However, the higher number of contacts formed and the differences in the polymer conformations reflected in the altered end-to-end distances suggest that the modifications are likely to affect hydrogel properties under the right conditions.

4.4 High water content

One factor that can influence the network structure significantly, and that limits polymer flexibility and the sizes of the pores, is the high chitosan density and low water content in the systems above. The water content in real hydrogels is often much larger, reaching weight fractions up to to 0.98-0.99.

To better understand what effect the water content has on the hydrogel properties, we have simulated hydrogels for all modifications with a higher water content. A 20 chitosan chains with DP = 50 and 100,000 CG water beads, *i.e.* 100 water molecules per monomer. This corresponds to a weight fraction to 0.89. Representative simulation snapshots from the end of the 100 ns trajectories are shown in Figure 4.3. From the snapshots, the overall structure of the acetylated networks still appears to be independent of χ. Similar to the denser systems, chains are evenly distributed throughout the simulation box. For the butyl-chitosan on the other hand the network-structure changes drastically between $\chi = 16\%$ and $\chi = 32\%$ of modification, forming dense clusters of hydrophobic modifications, surrounded by the polymer backbone, and connected by individual polymer strands. The result is a cluster/channel network featuring large pores between the dense chitosan clusters as shown in Figure 4.3e).

This morphological change is also clearly visible in the pore size distributions shown in Figure 4.3. While at 16% butylation, the pore size distribution looks very similar to those observed in the acetylated networks, with the majority of pore diameters between now 1.5 and 3.0 nm, in the 32 % butylated chitosan network, the pore sizes have markedly shifted to pore diameters centered around 7.0 nm.

As can be expected from the smaller number of modification beads in the system, and the larger volume fraction occupied by water, the total number of contacts between modification beads in the network has decreased. To account for the smaller total number

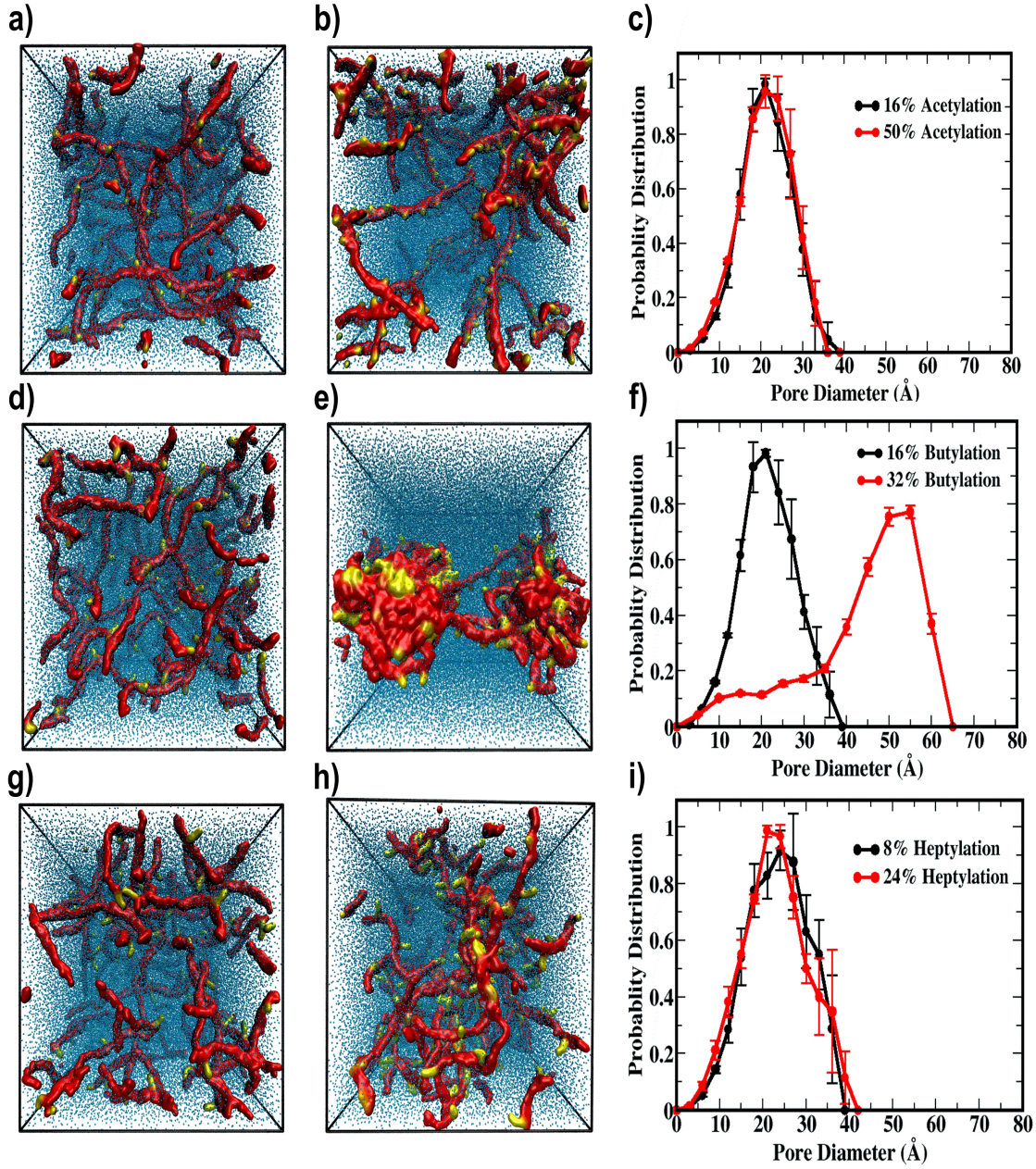

Figure 4.3: Simulation snapshots and pore size distributions of chitosan networks with 20 polymers of DP=50 and 100 water molecules/monomer with (a-c) acetyl, (d-f) butyl and (g-i) heptyl modifications. The simulation snapshots show the chitosan backbone (A,B,C beads) in red, modifications (M, MA, MB, MC beads) in yellow and water molecules as blue dots for (a) $\chi = 16\%$ acetylation (b) $\chi = 50\%$ acetylation, (d) $\chi = 16\%$ butylation, (e) $\chi = 32\%$ butylation, (g) $\chi = 8\%$ heptylation and (h) $\chi = 24\%$ heptylation.

of modifications in the system, the number of contacts has again been normalized by the number of modifications in the system. The number of contacts and the number of contacts per modifications for the high-water networks are also listed in Table 4.1. In the acetylated networks, and for butyl at low χ, the average number of contacts each modification forms has decreased with the higher water fraction. For $\chi = 32\%$ butylation and heptyl on the other hand, the contacts per modification are almost as high as in the denser networks, indicating their role in forming adhesive contacts.

The end-to-end distances of the polymers in the high water content gels, listed in Table 4.2, also show the same trends as before. Especially for the butylated chitosan, the changes with increasing values of χ have become much more pronounced in the hydrated networks, and the end-to-end distance decreases significantly, changing from 12.7 ± 0.8 nm at $\chi = 16\%$ to 5.6 ± 0.4 nm at $\chi = 32\%$. These very compact conformations of the polymers are required to accommodate the aggregation of the butyl modifications to clusters. In addition, the polymer backbones tend to wrap around these hydrophobic clusters to form micelle-like structures.

In contrast, a similar morphological transition does not take place in heptanoyl-chitosan systems, despite the even higher hydrophobicity of modification. Although small clusters of modification beads are visible in the simulation snapshots (Figure **??**, the resulting pore size distribution does not significantly change. Consistent with the absence of hydrophobic clusters heptanoyl-chitosan did not show any notable difference in the end-to-end distances. This different behavior of butanoyl- and heptanoyl-chitosan networks originates from the association between the hydrophobic modification groups, which is much stronger for the larger heptanoyl moieties. As a result, the initial heptanoyl clusters are too stable to allow a rearrangement of the network into a cluster/channel morphology, which requires dissociation and rearrangement of some of these initial contacts. This suggests that the network structure heptanoyl-chitosan is likely to be more rigid, and less amenable to adjust to different conditions in the surrounding aqueous environment, such as variations in ionic strength and pH.

4.5 Influence of modification pattern

Whereas the degree of acetylation or further modification of chitosan is typically well characterized, the distribution of the modifications on the chain is not easily determined experimentally and is likely to depend on the preparation process[71,72,73] . For chitosan,

typically a random distribution is assumed, however, it has also been suggested that deacetylation under heterogeneous conditions favors the formation of a blockwise pattern[74,75,76] .

A real random pattern will contain a mixture clusters of different sizes, especially for higher degrees of modification, and single modifications. To gain a clearer understanding of the relation between modification pattern and network properties, instead of simulating random patterns, we opted to compare the effect of individual, evenly spaced modifications as described in the previous sections to small modification blocks of four consecutive modifications (see Figure 4.4).

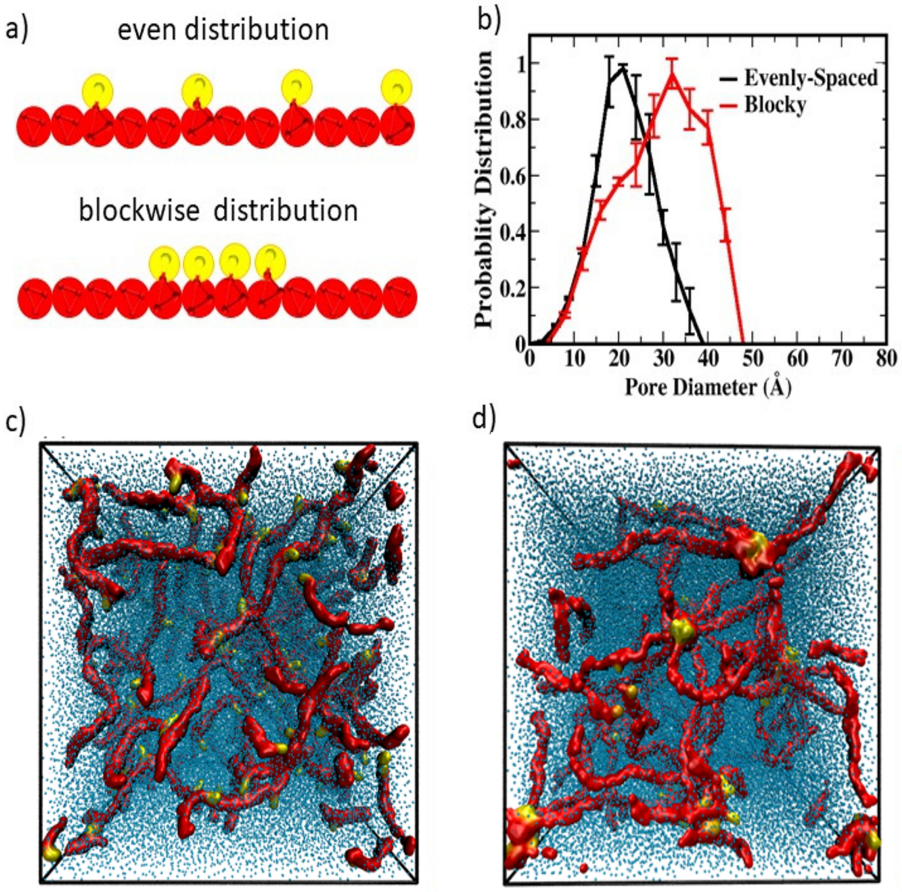

Figure 4.4: Effect of modification pattern: a) scheme of the evenly spaced and blockwise modification pattern; b) pore size distribution for $\chi = 16\%$ butylation with the two patterns; c) and d) simulation snapshots of for $\chi = 16\%$ butylation with c) evenly spaced and (d) blockwise modification.

The tendency of the hydrophobic modifications to interact with each other, is already observed in the RDFs shown in Figure 3.8 as well as in the clusters formed in

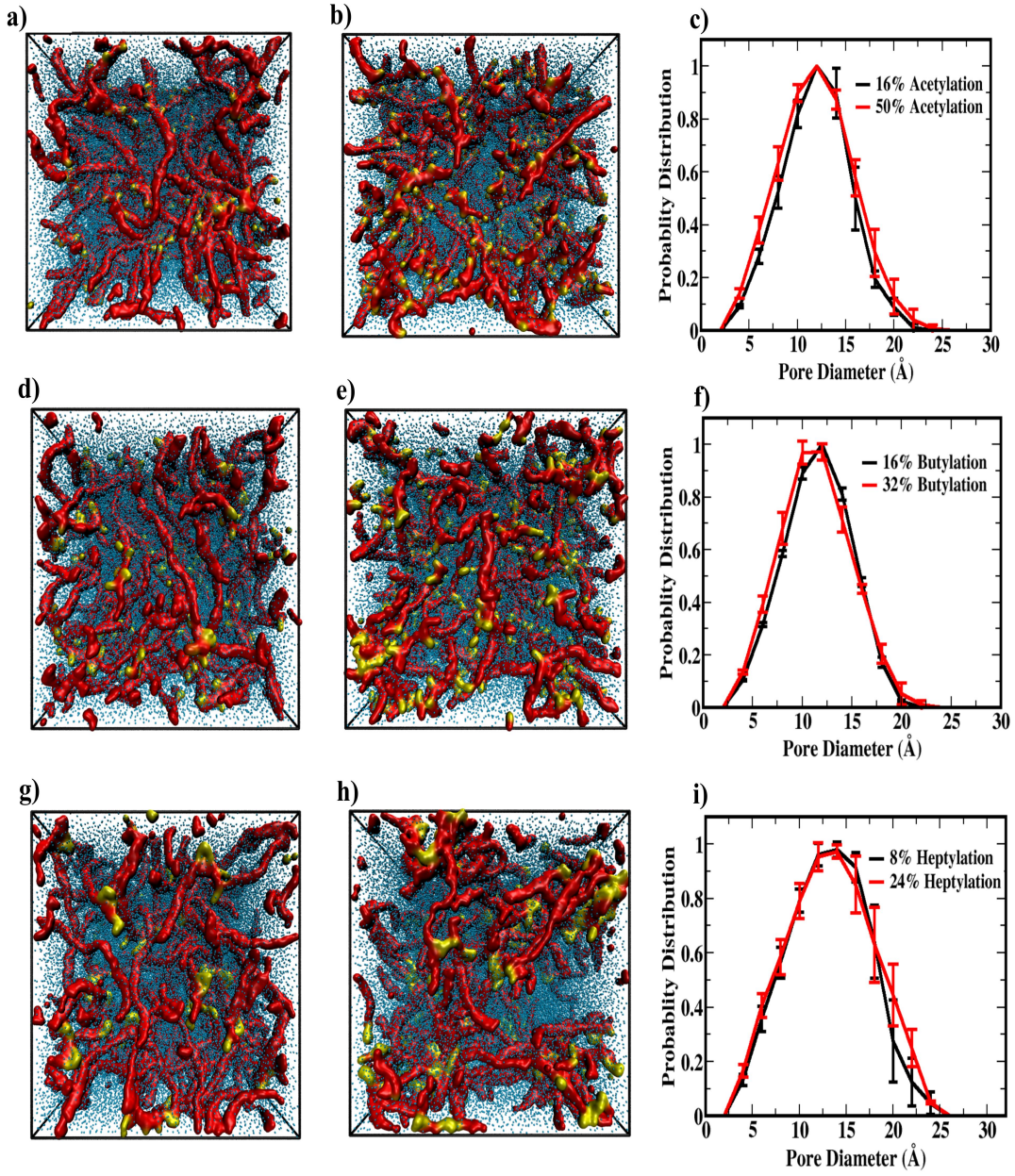

Figure 4.5: Simulation snapshots and pore-size distributions of chitosan networks with 50 polymers of DP=50 and 32 water molecules/monomer with (a-c) acetyl, (d-f) butyl and (g-i) heptyl modifications with blockwise modification pattern. The simulation snapshots show the chitosan backbone (A,B,C beads) in red, modifications (M, MA, MB, MC beads) in yellow and water molecules as blue dots for (a) $\chi = 16\%$ acetylation (b) $\chi = 50\%$ acetylation, (d) $\chi = 16\%$ butylation, (e) $\chi = 32\%$ butylation, (g) $\chi = 8\%$ heptylation and (h) $\chi = 24\%$ heptylation.

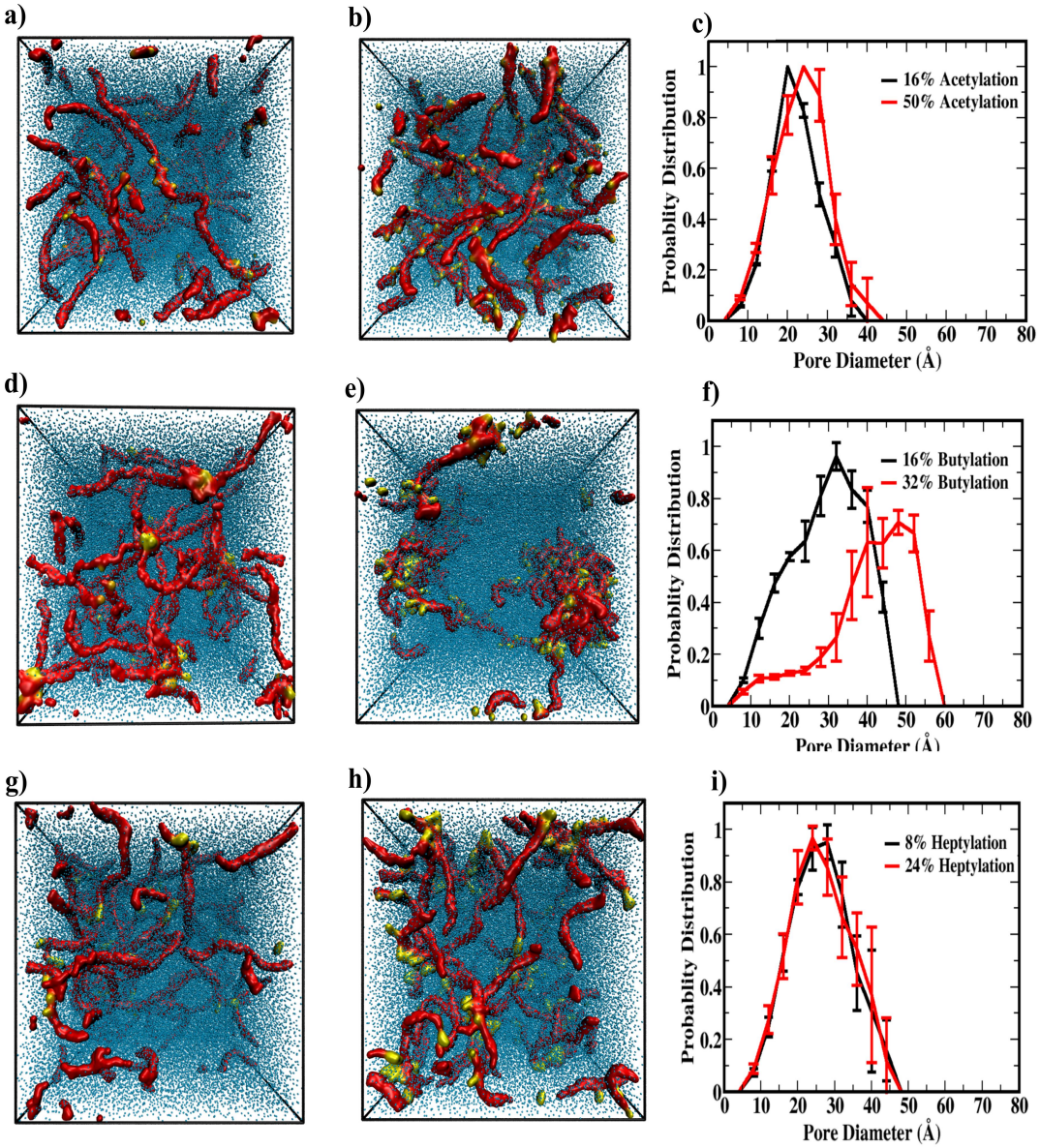

Figure 4.6: Simulation snapshots and pore-size distributions of chitosan networks with 20 polymers of DP=50 and 100 water molecules/monomer with (a-c) acetyl, (d-f) butyl and (g-i) heptyl modifications with blockwise modification pattern. The simulation snapshots show the chitosan backbone (A,B,C beads) in red, modifications (M, MA, MB, MC beads) in yellow and water mlecules as blue dots for (a) $\chi = 16\%$ acetylation (b) $\chi = 50\%$ acetylation, (d) $\chi = 16\%$ butylation, (e) $\chi = 32\%$ butylation, (g) $\chi = 8\%$ heptylation and (h) $\chi = 24\%$ heptylation.

the butylated and heptylated chitosan networks. A block pattern of modifications allows the modification beads to interact with several other modifications simultaneously, and thereby facilitates the formation of hydrophobic clusters while requiring less deformation of the polymer backbone. Thus, an enhancement of interactions between the modifications is expected.

	Low Water		**High Water**	
Modification	Total	per modification	Total	per modification
16% Acetylation	37 ± 9	0.09 ± 0.02	5 ± 3	0.03 ± 0.02
50% Acetylation	319 ± 23	0.26 ± 0.02	56 ± 10	0.11 ± 0.02
16% Butylation	456 ± 12	1.14 ± 0.03	308 ± 3	1.92 ± 0.02
32% Butylation	1034 ± 20	1.23 ± 0.03	507 ± 16	1.58 ± 0.05
8% Heptylation	399 ± 11	2.00 ± 0.06	151 ± 6	1.89 ± 0.08
24% Heptylation	1383 ± 24	2.35 ± 0.04	491 ± 15	2.04 ± 0.06

Table 4.3: Number of contacts between modification beads formed in the chitosan networks with modifications grouped in blocks of four

A comparison of the polymer data for the two patterns is summarized in Table 4.2. For acetylated chitosan, a comparison to the evenly spaced modifications shows no discernible effect of the blockwise distribution on the polymer properties, or network structure.

The average number of contacts between modifications increases compared to a uniformly distributed pattern in all the cases as shown in Table 4.3 , because a modification bead can more easily interact with several others in the immediate vicinity in the block pattern. For the end-to-end distances, overall the same trends are observed for the block chitosan, though they become less pronounced in the dense system as shown in Table 4.2 for high-water and low water content respectively.

The most striking difference between the two modification patterns, is observed for the onset of the network morphological transition to the cluster-pore network, which is markedly shifted to lower values of χ for a blockwise distribution of butyl groups. For other cases, it shows similar behaviour as compared to uniformly spaced modifications. At high ($\chi = 32\%$) level of modification, the networks for blockwise and evenly distributed modifications show a similar structure and and pore size distribution. However, for the block pattern, the distribution of pore sizes has already shifted to larger pore diameters, as compared to both the evenly spaced modifications (Figure 4.4b).

A change in the hydrogel structure is more easily accessible to experimental quantification than the distribution of modifications, for example by comparing the diffusion of different probe molecules through the system, as described below, and may therefore be helpful to distinguish modification patterns. However, for such a purpose, a detailed analysis of the effects of various cluster sizes as well as truly random distributions would be required.

4.6 Full range of substitution: 0% and 100%

To complete the structural picture, we have simulated the limiting cases of $\chi = 0\%$ and $\chi = 100\%$ acetylation. The latter corresponds to unmodified chitin, whereas the former represents fully deacetylated chitosan, which is, in practice, hard to produce and therefore not often used, so that typically 5% to 15% of monomers retain their acetyl groups. Experimental studies report that full deacetylated chitosan forms hydrogels with homogeneous networks[77] . Similarly, the fully deacetylated chitosan forms a uniform network structure spanning the simulation box as shown in the simulation snapshot in Figure 4.7a) , and the distribution of pore sizes and end-to-end distances that is very similar to those found in the acetylated chitosan networks.

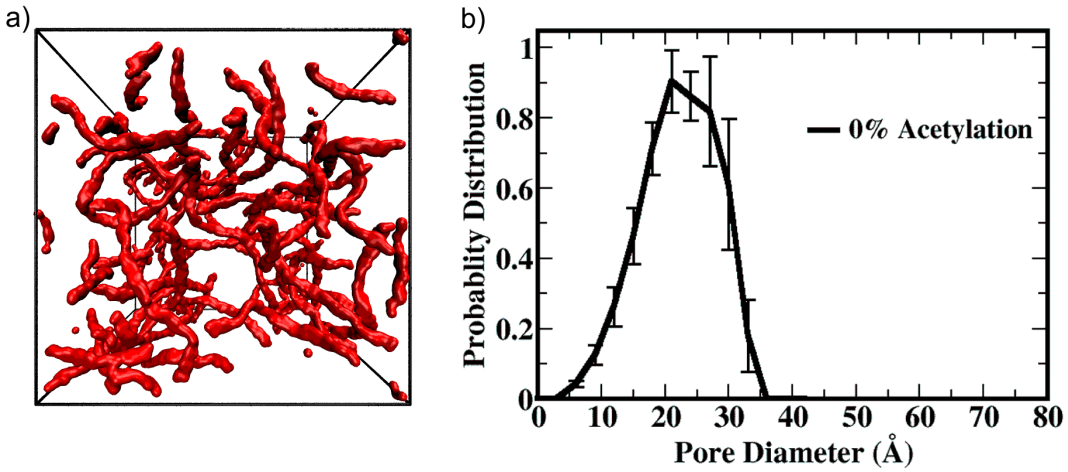

Figure 4.7: (a) Simulation snapshot and (b) pore-size distribution of deacetylated chitosan networks with 20 polymers of DP=50 and 100 water molecules/monomer. The simulation snapshots show the chitosan backbone (A,B,C beads) in red.

The fully acetylated polymers on the other hand self-assemble into form thick fibrils, as shown in Figure 4.8a). As a result of the alignment, the individual polymers

are straightened out and the average end-to-end distance increases to 20.4 ± 0.4 nm. Chitin is known to form crystalline fibrils with anti-parallel alignment of the polymers. Figure 4.8b) shows a fibril segment color-coded by the polymer direction. In this fibril, as well as the rest of the system, only about 50% of the polymers have formed an anti-parallel alignment, the rest aligned parallel to each other. In addition, the self-assembled fibrils are more twisted than the chitin structure. The crystal structure of α-chitin has been resolved[61,62] and can be compared to the self-assembled fibrils in our simulation model. Nevertheless, the contacts formed between the polymers with anti-parallel alignment show a remarkable similarity to those in the α-chitin structure, as shown for example in Figure 4.8c), which superimposes a segment of self-assembled fibril on the crystal structure. Thus, the CG model, despite being derived at quite different conditions, and low acetylation is able to reproduce the right crystal packing at least locally, which speaks for the wide rage of applicability of the model. Reproducing the overall formation of crystal fibers with the right orientation cannot be expected in an unbiased simulation of such large molecules, which are kinetically trapped, once they have aligned in either orientation[78] .

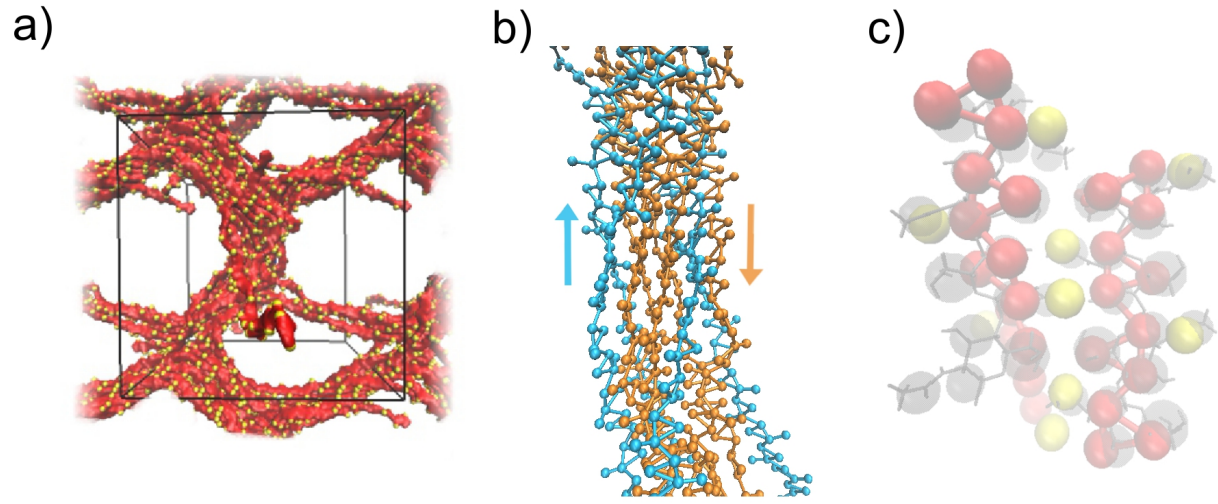

Figure 4.8: (a) Simulation snapshot of 100% acetylated chitosan networks with 20 polymers of DP=50 and 100 water molecules/monomer showing the chitosan backbone (A,B,C beads) in red, modifications M beads in yellow, (b) alignement of polymer in blue as non-reducing end at the top and orange as non-reducing end at the bottom while (c) shows the structure of two antiparallely aligned polymers superimpose to α-chitin structure from Ref[61,62] .

4.7 Conclusion

We have studied the morphologies of hydrogels formed by chitosan polymer with different modifications *i.e.* acetyl-, butanoyl-, heptanoyl and different water concentration with CG MD simulations. The structures formed were found to depend significantly on these material parameters. At low water concentration, the network structure does not show a measurable difference in hydrogel properties such as pore-size distribution, end-to-end distance and average number of contacts. The polymers form a uniform network in all cases. However, in case of high water content, the acetyl modified hydrogels still form a uniform network while with butanoyl, polymers aggregate around hydrophobic clusters formed. In heptyl modified hydrogel, polymer show strong association of the heptyl modification. However, they are so strong that once formed they are unable to rearrange so that no cluster-channel morphology can form. The pore size distribution shows shifts in the pore size, confirming the formation of polymer aggregates. The distribution of modifications across the polymer chains can also cause morphological changes in the network structure. Two modification patterns namely, a block modification pattern (four consecutive modified monomer) and evenly-spaced were analyzed in detail. Similar, network structures were obtained as for the evenly-spaced pattern for most conditions. However, the formation of hydrophobic clusters in the network becomes more favorable, so that the transition from the uniform network to the cluster-channel morphology sets on earlier in butyl modified chitosan. Finally, the minimum (0%) and maximum (100%) degree of acetylation cases were also studied. The 0% acetylation form a uniform network structure while 100% acetylation forms fibrils. The fibril are twisted and 50% anti-parallel aligned that resemble with the structure of α chitin.

Chapter 5

Effect of chitosan hydrogel properties on drug diffusion

5.1 Introduction

Chitosan hydrogels have been extensively utilized as materials for tissue engineering, wound healing, and drug delivery[79,80,81] . Their optimization as drug delivery carriers for clinical applications, however, is extremely laborious due to the variety of tunable parameters controlling the structure and transport properties of these materials. Computational models capable of predicting the transport properties of drugs across chitosan-based hydrogels have the potential of accelerating pre-clinical development and translation. Critical towards accurate modeling of drug diffusion is the development of a detailed model connecting physicochemical properties and architecture of the chain network and drug properties. In this work, we adopted DOX and GEM, established chemotherapeutic drugs, as model molecules to study diffusion through modified chitosan hydrogels. GEM is a small (263.2 g/mol), hydrophilic and electrically neutral molecule, whereas DOX is a larger (543.5 g/mol) amphiphilic molecule. CG models of DOX and GEM were initially prepared through the mapping shown in chapter 3, and drug-drug, drug-solvent, and drug-chitosan interactions were obtained from initial all-atom simulations as presented in chapter 3.

In this chapter, first an atomistic analysis was conducted to study the type of interaction between the chitosan polymer-drugs. The CG model of chitosan introduced in chapter 2 & 3 was designed in a way that can afford the delivery for any desired drug combination with a synergistic molar ratio and kinetics. As an example for the significance of hydro-

gel morphology, the diffusion of two example drug molecules GEM and DOX through the different gel morphologies was also simulated. Diffusion trends were obtained for both the drugs. To study the effect of multiple drugs interacting with each other on diffusion trends, dual drug migration through the network was also studied.

5.2 Analysis of drug-chitosan interactions at all-atom resolution

All-atom simulations of the drug-loaded chitosan hydrogels were analyzed to obtain a molecular-level understanding of (i) the interactions between the drug molecules and the modified chitosan chains and (ii) the dependence of these interactions on the type and degree (χ) of modification.

Atomistic systems have a high density of chitosan monomers and low water content, which were necessary to obtain a sufficient sampling of the forces needed to implement the CG procedure as described in Chapter 2. This high density, however, results in many non-bonded interactions between the polymer and drug molecules. It must be also noted that the frequency of these interactions in real hydrogels, where the water content is significantly higher, is much lower. Nonetheless, the analysis of these interactions at the atomistic scale provides insight into the relative contribution of different types of interaction between the drug and polymer. The interaction energies among the drug molecules, the chitosan backbone, and the modification groups were separated into electrostatic and Lennard-Jones (LJ) contributions and the ability to form hydrogen-bond was analyzed. The resulting interactions between DOX and modification groups and between DOX and the chitosan backbone as a function of χ are reported in Figure 5.2. The analogous results for GEM are shown in Figure 5.3. The hydrogen-bond interactions for DOX modification and DOX backbone as a function of χ are reported in Figure 5.4. The hydrogen-bond interaction for GEM modification and GEM backbone as compared to DOX is negligible.

We observed that the interactions between the drug molecules and chitosan were consistently dominated by the LJ-type, particularly for DOX as compared to GEM. DOX interacts both with the chitosan backbone and the modifications; The daunosamine moiety in DOX (ring structure shown in Figure 5.1) aligns with the pyranose rings in the chitosan backbone resulting in the formation of multiple hydrogen bonds (Figure 5.1a and b). However no alignment were observed between GEM and the chitosan back-

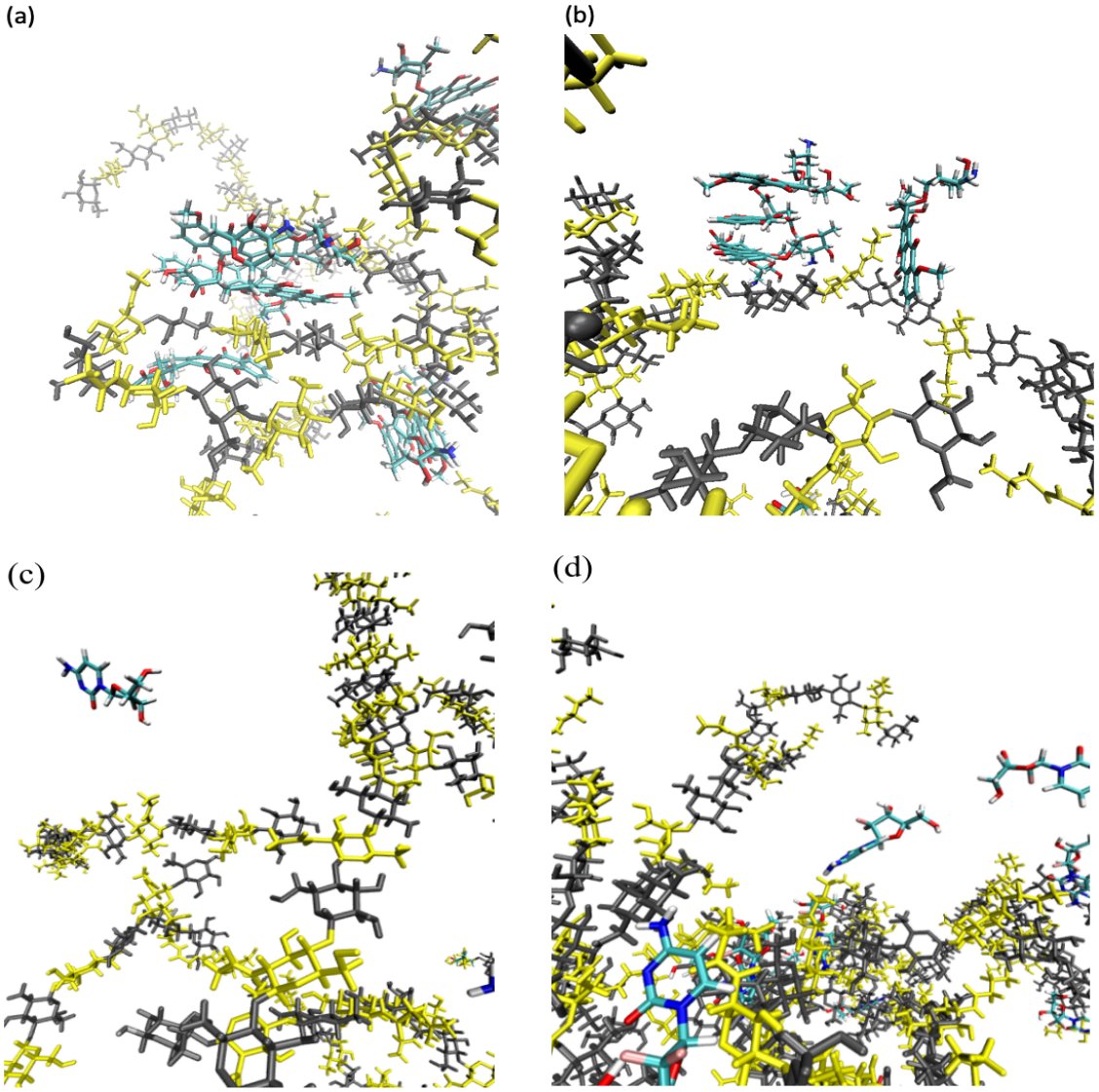

Figure 5.1: All-atom simulations depicting the interactions between the interactions between DOX and GEM (red for oxygen, blue for nitrogen, fluorine for pink and white for hydrogen) and chitosan (grey:Glucosamine and yellow: N-acyl-glucosamine) for (a) acetyl modified chitosan with DOX, (b) butanoyl modified chitosans with DOX, (c) acetyl modified chitosan with GEM, and (d) butanoyl modified chitosans with GEM.

bone or modification as shown in Figure 5.1c and d) and doesnot result in multiple hydrogen bond as well. As the χ of acetylation increases from 16% to 50%, the number of contacts between the DOX and the modifications increases from 55 to 170. With butanoyl-modified chitosan, the number of non-bonded interactions between DOX and the modifications increases further to 225 at $\chi = 16\%$ and 550 at $\chi = 32$ %. The increase

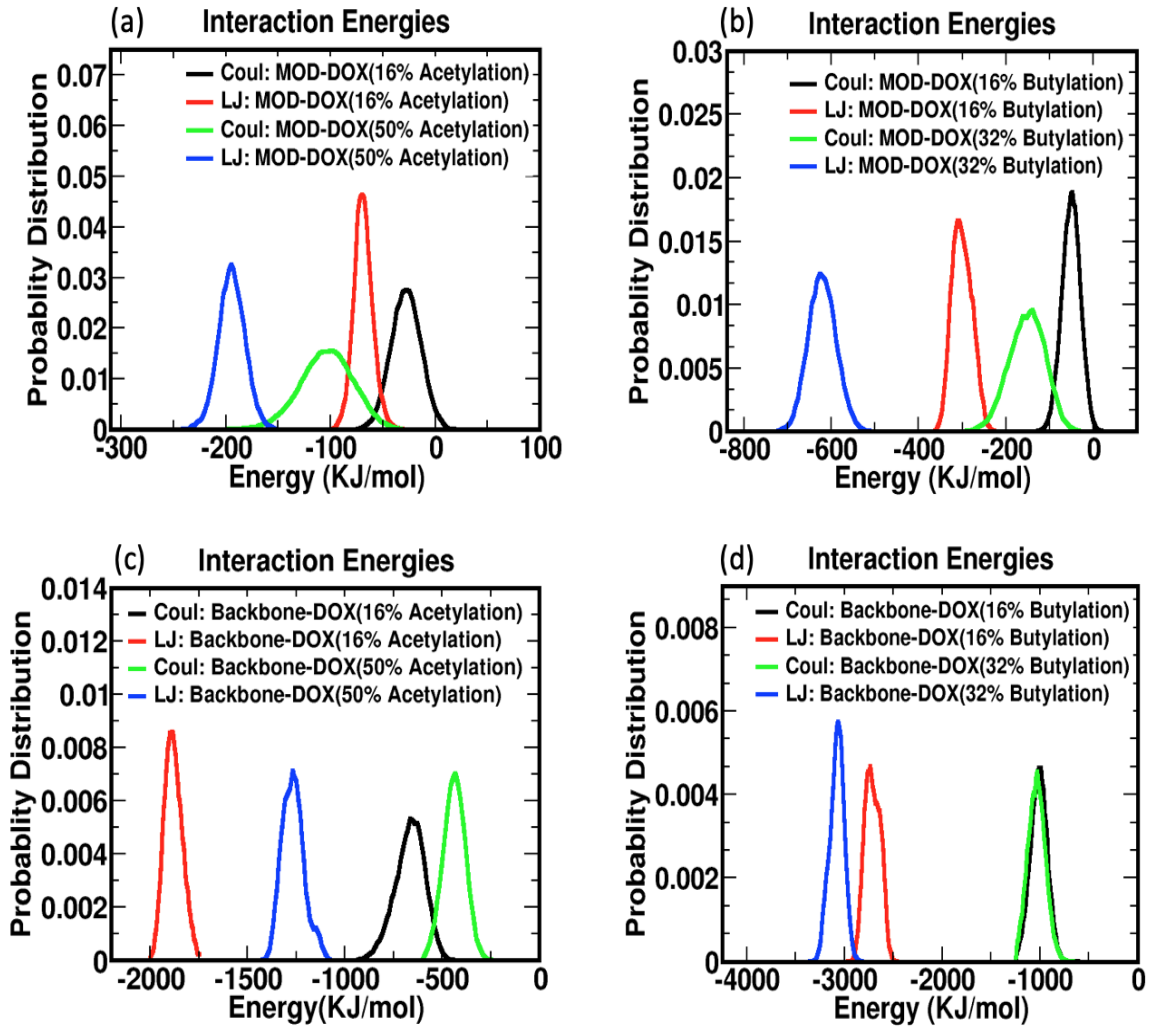

Figure 5.2: Lennard-Jones and coulombic contribution to the DOX-modification group interaction energy for (a) acetyl-chitosan and (b) butanoyl-chitosan; and Lennard-Jones and coulombic contribution to the DOX-backbone interaction energy for (c) acetyl-chitosan and (d) butanoyl-chitosans at different χ.

in the number of non-bonded interactions is reflected by the increase of interaction energy shown Figure 5.2. On the other hand, the dependence of the backbone interactions with χ is less clear. In particular, the number of non-bonded interactions decreases with χ for acetyl modifications and increases slightly for butanoyl modifications. It should be noted, however, that DOX molecules tend to aggregate into clusters(Figure 5.1a and b), thereby reducing their ability to form interactions with the backbone, especially within the timescale of the all-atom simulations, where equilibration of the aggregate size is not

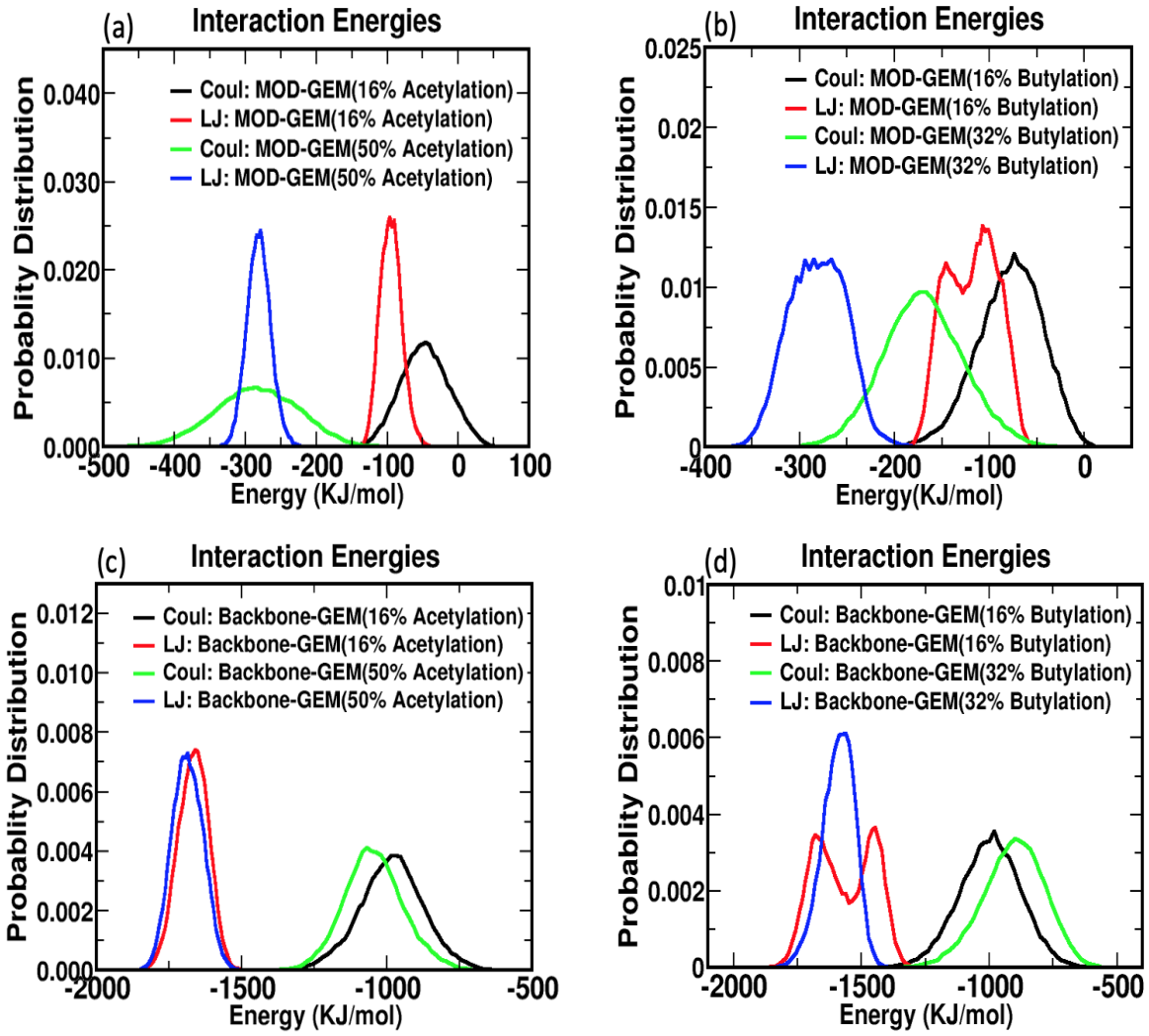

Figure 5.3: Lennard-Jones and coulombic contribution to the GEM-modification group interaction energy for (a) acetyl-chitosan and (b) butanoyl-chitosan; and Lennard-Jones and coulombic contribution to the GEM-backbone interaction energy for (c) acetyl-chitosan and (d) butanoyl-chitosans at different χ.

accessible. GEM shows overall weaker interactions with the chitosan chains as shown in Figure 5.3. The LJ contribution to the interaction energy, in fact, is about 50% of that observed with DOX, whereas the electrostatic contribution, is approximately the same for both the drugs.

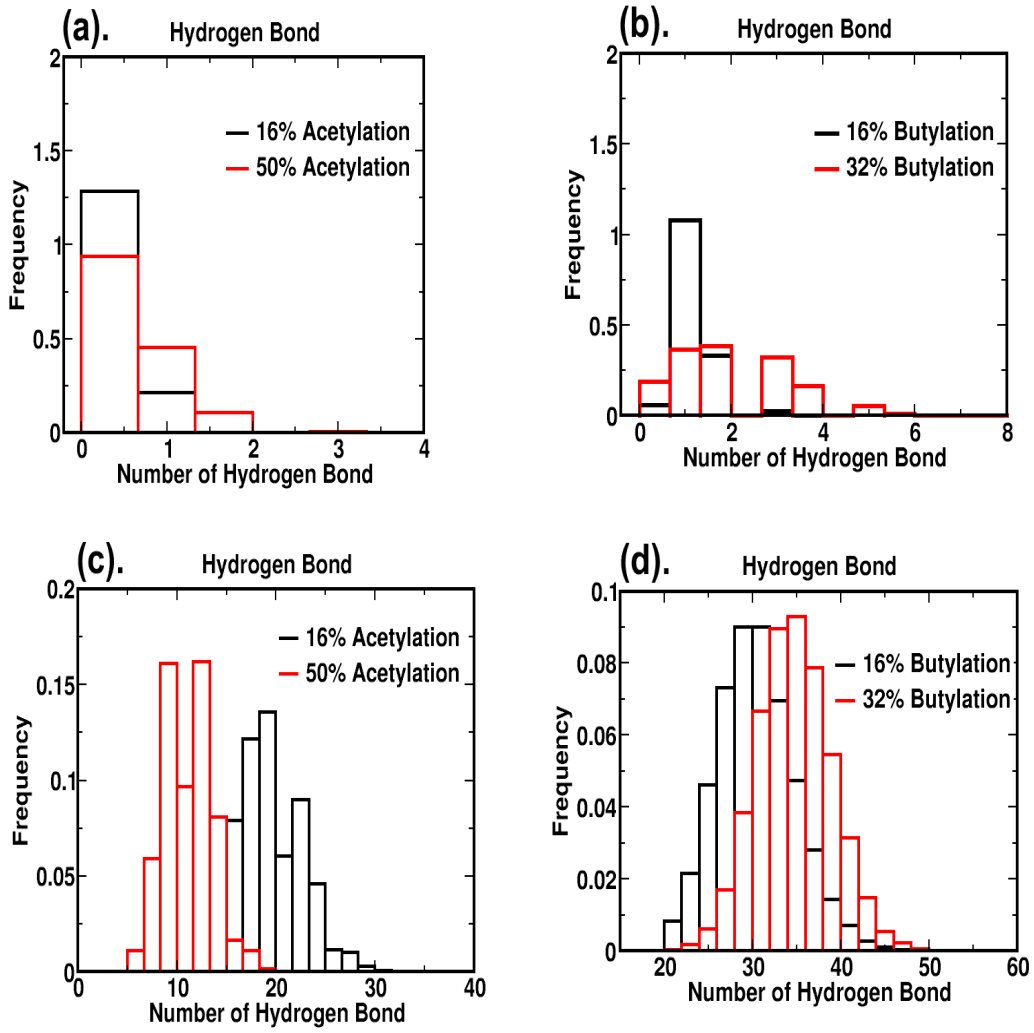

Figure 5.4: Hydrogen bond contacts for between DOX and modification groups in a (a) acetyl- modified and (b) butanoyl-modified; and hydrogen bond contacts for between DOX and the backbone in a (c) acetyl-modified and (d) butanoyl-modified chitosans at different degrees of modification.

5.3 Dynamic properties of the CG system

To be able to reliably characterize their dynamics in the CG system, the diffusion coefficients of the drug molecules were calculated from the slope of the mean-squared displacement (MSD) of the drug molecules with respect to time and compared to the all-atom dynamics as listed in Table 5.1. As expected, the dynamics in the CG system are significantly faster than in the all atom models, which is one of the factors leading to the great efficiency of CG models in general. Comparing the diffusion coefficients

for water at atomistic and at CG resolution, D^{atom} and D^{CG}, respectively, the ratio is $\tau_D = \frac{D^{CG}}{D^{atom}} = 6.4$, *i.e.* dynamics in the CG system are 6 to 7 times faster than those in the atomistic model. The value $D^{\text{atom}} = 2.74 \times 10^{-5}\text{cm}^2/\text{s}$ is in good agreement with diffusion constants reported in the literature for the TIP5P water model[82] . Using the same factor τ_D to scale the diffusion constants observed for DOX and GEM, the value obtained for DOX $D^{\text{atom}} \approx 0.1 \times 10^{-5}\text{cm}^2/\text{s}$ is in reasonable agreement with the experimentally determined value of $D^{\text{atom}} \approx 0.21 \times 10^{-5}\text{cm}^2/\text{s}$[83] . The atomistic values for DOX and GEM on the other hand are significantly lower. It is possible that the small box size and the high concentration of drug molecules contribute to this larger difference and reduce the dynamics of DOX and GEM in the atomistic systems. Thus, especially when the expected speedup in dynamics is taken into account, the CG model provides a reasonable prediction of the diffusion coefficients of the two model drugs.

system		D
water	atomistic	2.741 ± 0.164
water	CG	17.530 ± 0.733
DOX	atomistic	0.056 ± 0.0167
DOX	CG	0.625 ± 0.058
GEM	atomistic	0.143 ± 0.005
GEM	CG	3.683 ± 0.626

Table 5.1: Diffusion coefficients ($10^{-5}cm^2/s$) comparison for DOX and GEM with pure water in atomistic and CG simulation respectively.

5.4 Simulation of single drug migration through modified chitosan hydrogels: Lower drug concentration

The all-atom simulations described in section 5.1 were performed to evaluate the molecular-level interactions and elucidate the thermodynamic mechanisms by which the drugs interact with the chitosan backbone and the modification groups.

The equilibrated chitosan hydrogel structures obtained in Chapter 4, were loaded with 10 drug molecules of either DOX or GEM initially placed at random positions. The concentration of drug molecules was chosen low to avoid strong drug-drug interaction. In choosing the number of drug molecules, we also considered the trade-off between

ensuring reproducible simulations (higher drug loading) and avoiding the formation of aggregates (lower drug loading). While, in fact, an insufficient number of drug molecules can lead to poor statistical significance, especially when diffusing through structurally non-homogeneous systems, excessive drug loading results in the formation of aggregates, which would distort drug migration through the polymer network. However, similar result were obtained for loading the system with 20 drug molecules as described below in next section. Regarding the choice of distributing the drug molecules randomly across the network, we note that the diffusion constants obtained by arranging the drug molecules into different initial distributions showed the same trends and, in most cases, agreed within the fitting error.

CG simulations of 10 ns were performed and the diffusion of the drug molecules through the networks was monitored. The diffusion constants were calculated and are reported in Figure 5.5. The error bars correspond to the fitting error due to the non-linearity of MSD fitting. It should be noted that the diffusion constants did not significantly change with simulations performed at longer time scales.

As anticipated, the differences in hydrogel morphology (homogeneous vs clusters/ channels) and physicochemical properties of the drugs and the modification groups result in different trends of drug diffusion vs χ. GEM migrates through all networks with a diffusion constant similar to that of free GEM in water, indicating that there is no effect of the polymer on its diffusion (Figure 5.5 a & c). GEM molecules, which are small and hydrophilic, form a relatively low number of nonbonded interactions with the chitosan chains, irrespective of the type of modification and χ, as listed in Table 5.6. This is also consistent with the size of GEM, which has a radius of gyration of 0.33 nm. The predominant pore diameters in the uniform hydrogels is on the order of 1.2 nm, so that GEM molecules can travel easily through the pore network provided that there are no strong interactions with the polymers. Owing to the limited interaction with the polymer chains, GEM travels easily through the water-filled channels in both homogeneous and cluster/channel hydrogel morphologies. Only a slight reduction in GEM diffusion is observed in butanoyl-chitosan at higher χ.

On the other hand, DOX molecules, which are larger and more hydrophobic, show markedly different values of diffusion coefficient, and most notably, an inversion in the diffusion trend with χ between acetyl- and butanoyl- modifications. In acetylated-chitosan networks, DOX diffusion decreases at higher χ, independently of the modification pattern (Figure 5.5 b). However, the network structure and pore size distri-

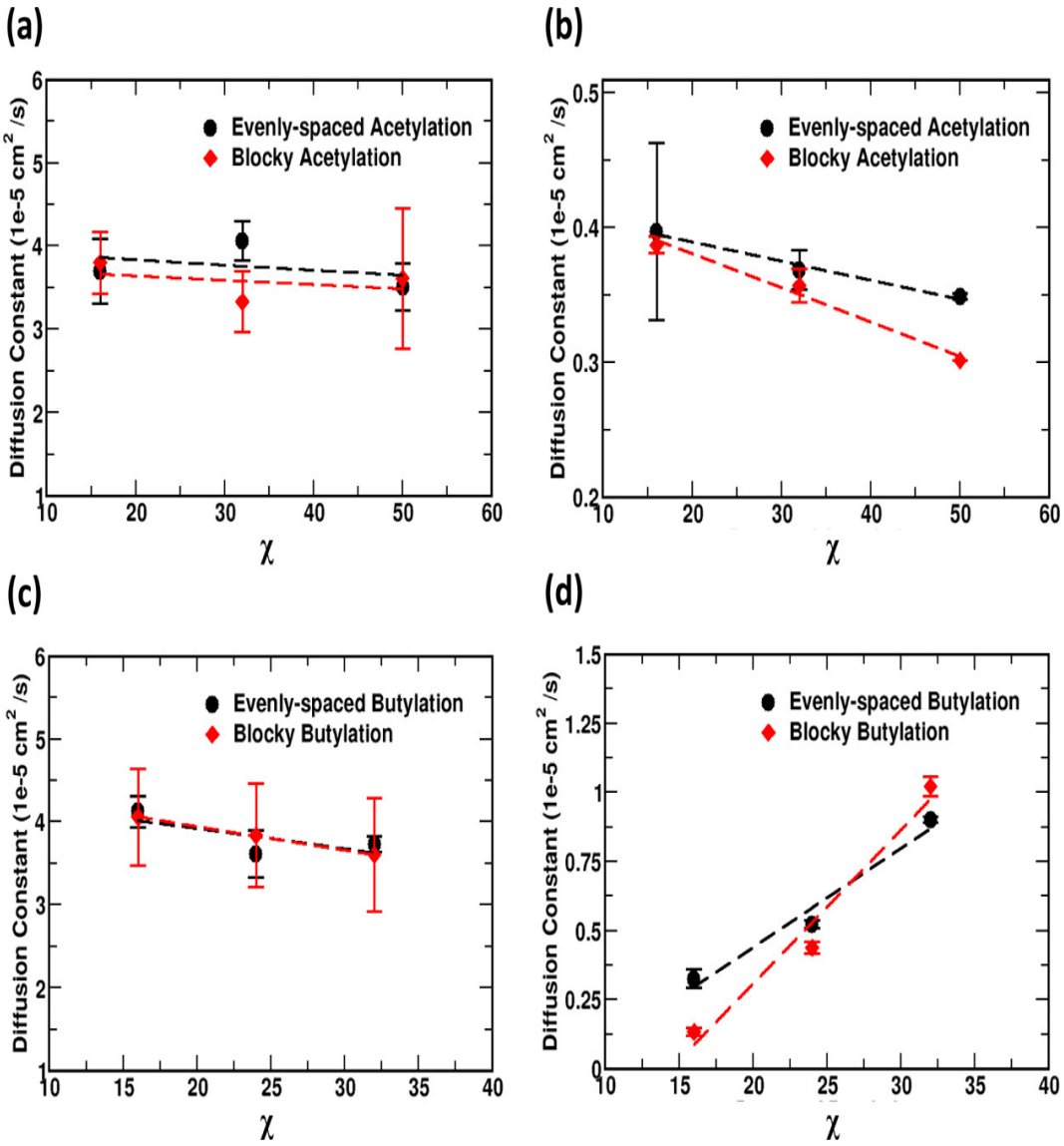

Figure 5.5: Drug diffusion constants vs. χ for single-drug migration across different chitosan networks for evenly-spaced (black) and blocky (red) modification patterns: (a) GEM and (b) DOX in acetyl-chitosan, and (c) GEM and (d) DOX in butanoyl-chitosan.

butions were found to remain unaltered with χ, both for the evenly-spaced and blocky acetylated-chitosan networks , indicating that network morphology is unlikely to be the cause of DOX decreased mobility. Rather, the decreased diffusion coefficients of DOX at larger χ can be attributed to increased number of non-bonded interactions between DOX and the modified chitosan molecules. As reported in Table 5.6, in fact, the number of non-bonded interactions between DOX and the acetyl moieties increases with χ for both modification patterns, although the number of non-bonded interactions with

Drug		Backbone, Low	Mod, Low	Backbone, High	Mod, High
DOX	Acetyl (evenly spaced)	217 ± 14 (93.5%)	15 ± 2 (6.5%)	239 ± 11 (83.9%)	46 ± 4 (16.1%)
	Acetyl (blocky)	225 ± 12 (84.9%)	40 ± 3 (15.1%)	221 ± 11 (79.8%)	56 ± 4 (20.2%)
	Butanoyl (evenly spaced)	219 ± 15 (78.5%)	60 ± 7 (21.5%)	316 ± 23 (83.6%)	62 ± 6 (16.4%)
	Butanoyl (blocky)	276 ± 13 (83.1%)	56 ± 7 (16.9%)	371 ± 18 (88.1%)	50 ± 7 (11.9%)
GEM	Acetyl (evenly spaced)	26 ± 10 (89.7%)	3 ± 1 (10.3%)	33 ± 10 (80.5%)	8 ± 3 (19.5%)
	Acetyl (blocky)	30 ± 9 (88.2%)	4 ± 2 (11.8%)	41 ± 11 (80.4%)	10 ± 4 (19.6%)
	Butanoyl (evenly spaced)	34 ± 10 (89.5%)	4 ± 2 (10.5%)	169 ± 25 (87.6%)	24 ± 7 (12.4%)
	Butanoyl (blocky)	61 ± 11 (81.3%)	14 ± 5 (18.7%)	163 ± 16 (80.3%)	40 ± 6 (19.7%)

Figure 5.6: Number and (percentage of total) of non-bonded interactions observed between drug molecules and chitosan chains (backbone and modifications) in the different chitosan networks over the drug molecules trajectories during the simulation; where DOX molecules are treated as a group so that any given chitosan or modification site can only contribute one contact. In the table, low represents $\chi = 16\%$ for both systems, and high represents $\chi = 50\%$ and 32% for acetyl-and butanoyl- modified systems, respectively

the backbone remains constant. For example, a DOX molecule forms on average of 15 $\pm$ 2 interactions with acetyl-chitosan at $\chi = 16\%$, and up to 60$\pm$ 4 interactions with acetyl-chitosan at $\chi = 50\%$ with evenly spaced pattern. This indicates that hydrophobic non-bonded interactions are the main cause of the slowed diffusion.

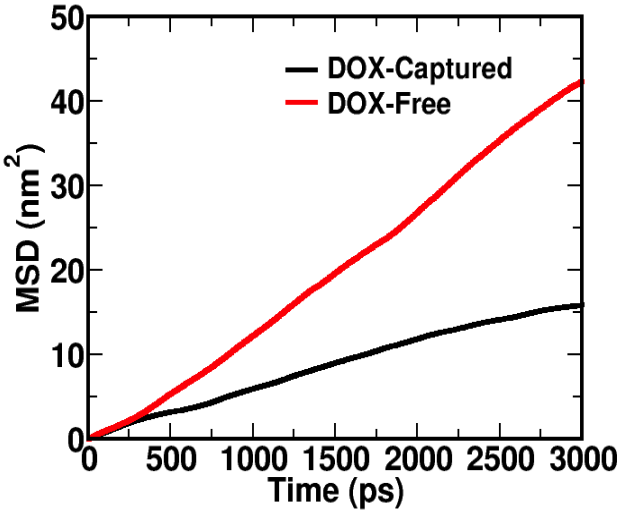

Figure 5.7: Mean-squared displacement (MSD) plot vs. time for diffusion of DOX through the blocky butyl-modified chitosan network at $\chi = 32\%$, where DOX-Captured refers to DOX that becomes entrapped within a cluster and DOX-Free refers to DOX that remains in the pores of the cluster/channel morphology during the simulation.

Inversely, DOX diffusion through butanoyl-chitosan gels increases with χ, independently of modification patterns (Figure 5.5 d). As χ increases, the butanoyl-chitosan network undergoes a transition from homogeneous to cluster/channel morphology. CG simulations of DOX migration through butanoyl-chitosan systems show dramatic differences to the fate of DOX molecules depending on the morphology of the network, i.e., homogeneous or cluster/channel. The migration of DOX through the homogeneous butanoyl-chitosan network (low χ, Figure 5.9 c) is identical to that of DOX through homogeneous acetyl-chitosan network (low and high χ, Figure 5.9 a and b). Through clustered butanoyl-chitosan, instead, DOX molecules either adsorb onto/within the chitosan clusters or travel freely through the large pores (Figure 8 d). This indicates that, as in acetyl-chitosan systems, interactions between DOX and butanoyl-chitosan at high χ occur (see Table 5.6). However, the DOX molecules freely migrating through the large pore are responsible for the increase in the overall diffusion coefficients; this is corroborated by the comparison in mean-squared displacement MSD vs. time for both adsorbed and freely migrating DOX molecules as shown in Figure 5.7. It is also crucial to note that the chitosan vs. water ratio and consequently the channel vs. cluster ratio are much higher in the experimental systems than in the simulated networks. We there-

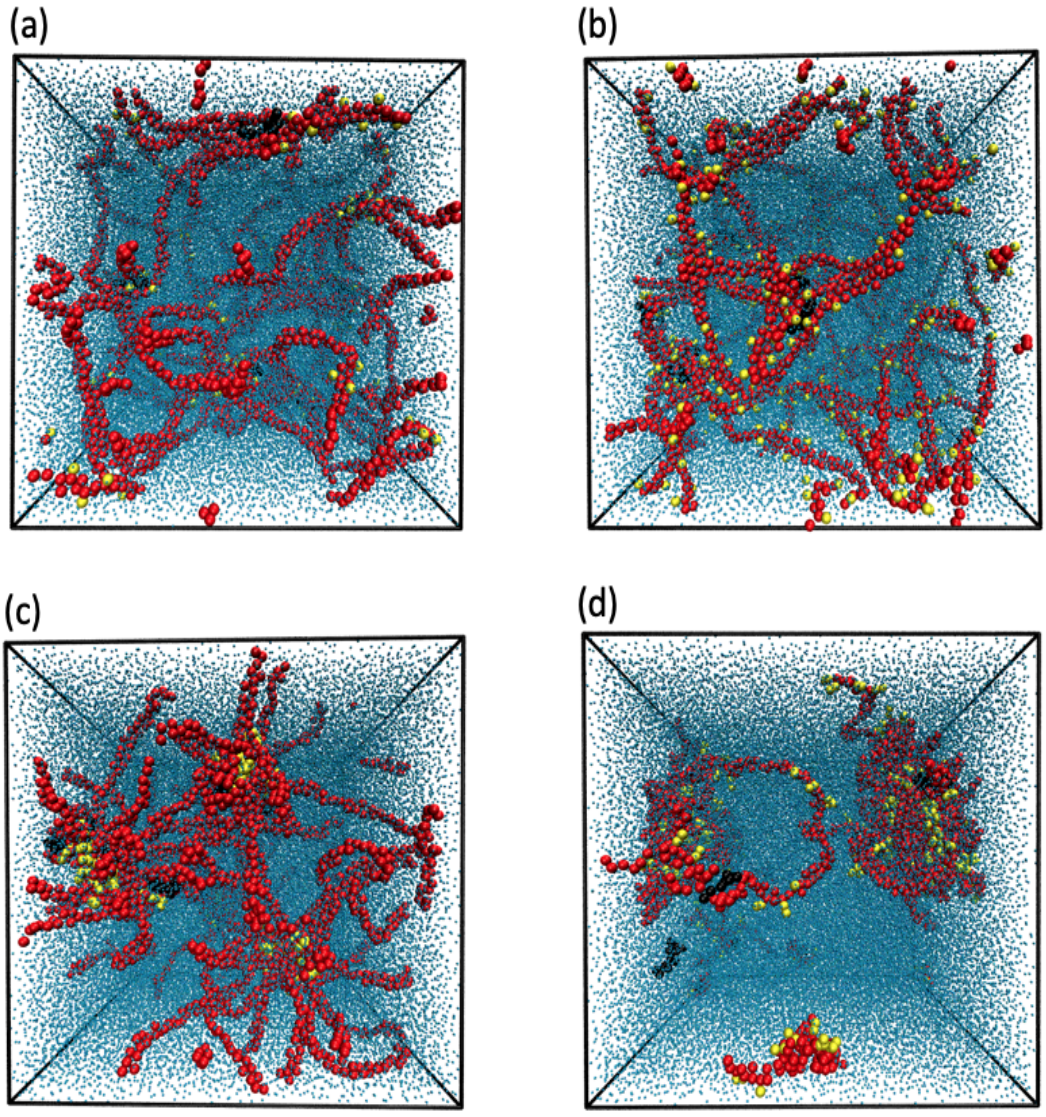

Figure 5.8: Snapshot of DOX migration through: (a) acetyl-chitosan networks at low χ (16%); (b) acetyl-chitosan networks at high χ (50%); (c) butanoyl-chitosan network at low χ (16%); (d) butanoyl-chitosan networks at high χ (32%) where the chitosan backbone is represented by red beads, modifications are represented by yellow beads, and DOX is represented by black beads

fore expect the actual hydrogel to mirror the increase in the diffusion coefficient with χ observed in the CG simulations. The diffusion and release of DOX from hydrogels with such a cluster-pore morphology will be therefore closely related to the fraction of the molecules diffusing in the pores. This is determined by the partition coefficient K^c of the molecules to the hydrophobic clusters, which is defined as $K^c = \frac{c_{cl}}{c_w} = \frac{N_{cl}}{N_w}\frac{V_w}{V_{cl}}$. Therefore,

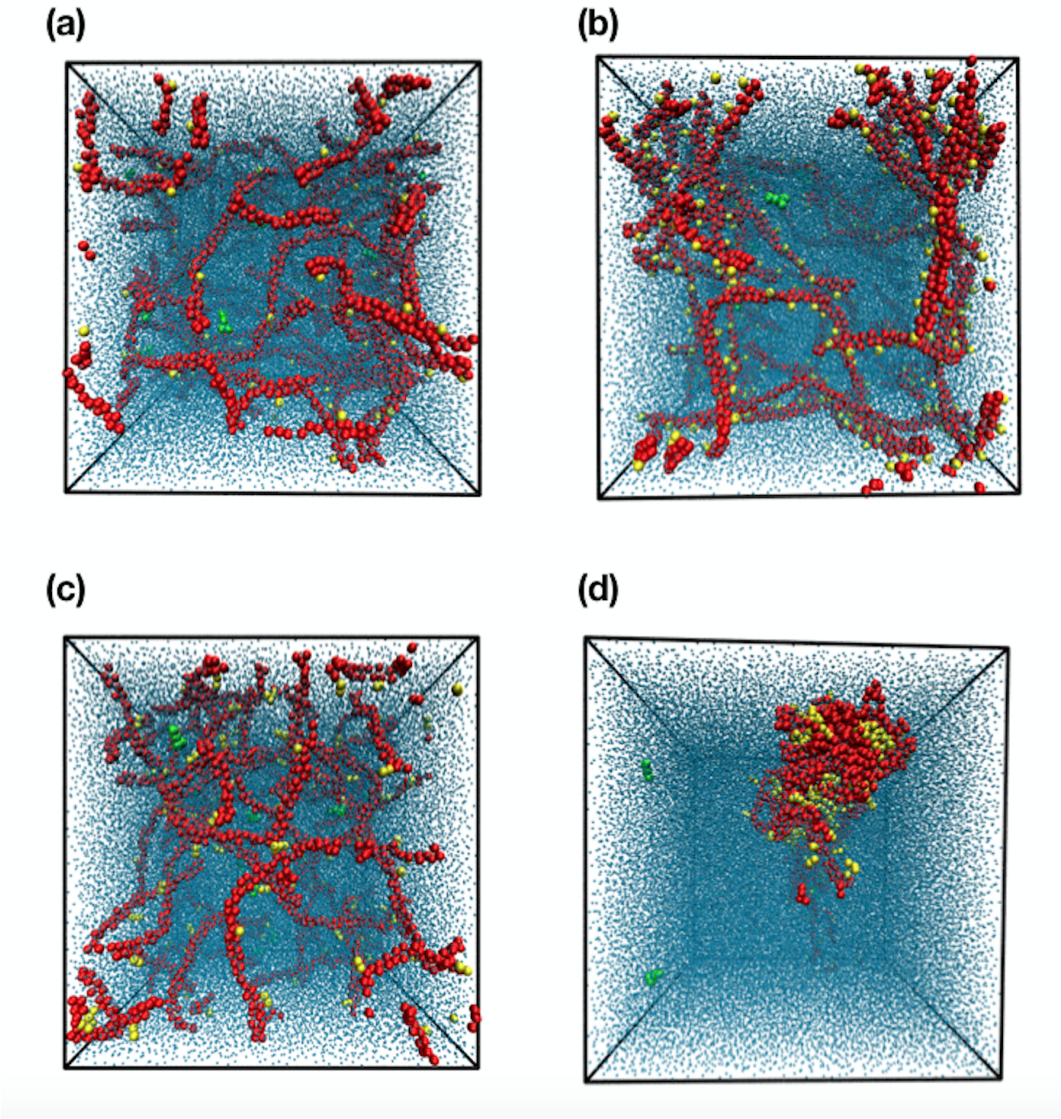

Figure 5.9: Snapshot of GEM migration through: (a) acetyl-chitosan networks at low χ (16%); (b) acetyl-chitosan networks at high χ (50%); (c) butanoyl-chitosan network at low χ (16%); (d) butanoyl-chitosan networks at high χ (32%) where the chitosan backbone is represented by red beads, modifications are represented by yellow beads, and GEM is represented by green beads

the fraction of DOX molecules stuck to the clusters is $\frac{N_{cl}}{N_w} = K^c \frac{V_{cl}}{V_w}$ and depends both on the affinity to the hydrophobic clusters, and the volume ratio of clusters and water phase. Using octanol-water partition data as a rough estimate, $\frac{N_{cl}}{N_w} \approx 4\frac{V_{cl}}{V_w}$, so that in gels with high water contents as is generally the case[84] diffusion will be dominated by molecules diffusing in the pores. Overall, the diffusion trends shows the same behavior

on compared with the experimental diffusion trends[21] .

The faster dynamics enabled by the smoother energy landscapes featured in CG simulations may introduce some error in the calculation of the diffusion constants; however, the comparison among the migration of drug molecules in different networks provides a reliable evaluation of the influence of the network morphology and physicochemical properties on drug transport. In the cluster/channel morphology, in particular, the difference between diffusional pathways of single-drug molecules becomes very pronounced, with drug molecules experiencing sharper differences in the morphology of the medium through which they diffuse. Collectively, these single-drug simulations indicate that the hydrophobicity driven morphing of the hydrogel structure affects drug diffusion by two opposing mechanisms: first, the larger pores favor the migration of the drug molecules; and second, the nesting of the modification groups within the core of the clusters is responsible for strong adsorption of the drug molecules that embed in the chitosan clusters; notably, our simulations indicate that while both DOX and GEM are affected by the first mechanism, only DOX undergoes the second mechanism. We anticipate that the high water/polymer ratio of the real chitosan hydrogels makes the first mechanism dominant over the second.

5.4.1 Effect of higher drug concentration on diffusion trends

To evaluate how the single drug diffusion trends change with high drug concentration, 20 DOX or 20 GEM molecules were inserted at random locations in the equilibrated network structures for 16% & 50% acetylation and 16% & 32% butylation and their motion through the chitosan hydrogels was analyzed. The results indicate that GEM shows same diffusion trend as observed in Section 5.3 *i.e.* with diffusion constants that are only minimally affected by interactions with the chitosan gels.

Similarly, the MSD curves for DOX shown in Figure 5.10 depend noticeably on the type and level of modification, and the diffusion is slowed down for acetylation as observed for the smaller number of DOX molecules. At $\chi = 16\%$ the MSD of DOX in the acetylated and butylated chitosan networks looks very similar, leading also to approximately the same diffusion constants (see Table 5.2). However, when the level of modification is increased, the MSD curve for 50% acetylation falls below that in 32% acetylation, meaning that DOX diffusion decreases for larger χ. Inversely the diffusion rate through 32% butylated chitosan has significantly increased, corresponding to a diffusion constant that is more than twice as large as for $\chi = 16\%$.

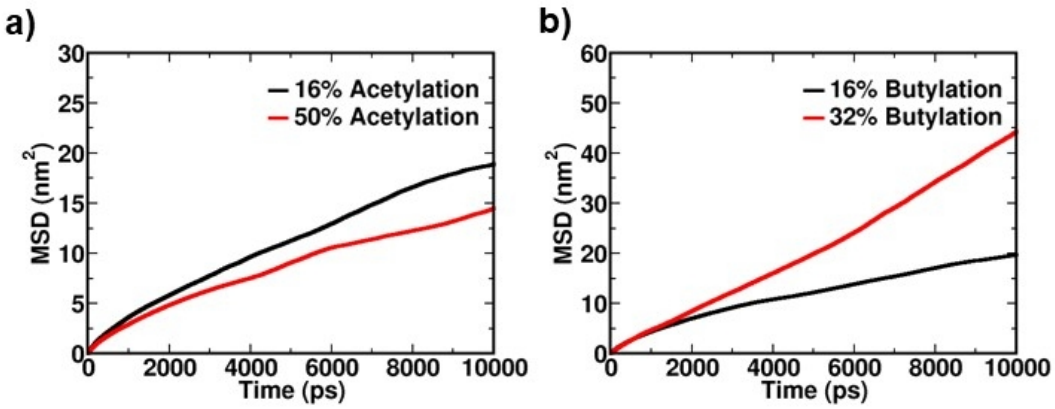

Figure 5.10: Mean-square Displacement of DOX (a) Acetylated chitosan network (b) butylated chitosan network for a uniformly-spaced modification pattern.

For further analysis the interactions between DOX molecules and the chitosan network were analyzed by counting the number of contacts within 0.6 nm. As summarized in Table 5.3 the number of interactions between DOX and the M beads increases for χ=16% have 27 ± 3 while χ=50% have 83 ± 5 average number of contacts, whereas the number of contacts with the chitosan backbone remains approximately constant at 400-420 contacts over the range of χ values. Thus the slow down of DOX diffusion through the acetylated gel was observed due to the increase in interactions with the hydrophobic modifications at higher χ, as explained in the previous section. In comparison, GEM interacts much less with the chitosan network with only about 30-40 contacts in total, consistent with its unhampered diffusion through the gel.

	DOX		**GEM**	
	Evenly-spaced	**Blocky**	**Evenly-spaced**	**Blocky**
Modification	Diffusion Const.	Diffusion Const.	Diffusion Const.	Diffusion Const.
16% Acetylation	0.268 ± 0.100	0.213 ± 0.034	3.878 ± 0.764	3.787 ± 0.422
50% Acetylation	0.161 ± 0.003	0.191 ± 0.000	3.572 ± 0.470	3.905 ± 0.150
16% Butylation	0.257 ± 0.042	0.150 ± 0.050	3.906 ± 0.149	3.588 ± 0.464
32% Butylation	0.827 ± 0.039	0.550 ± 0.082	3.078 ± 0.126	3.16 ± 0.30

Table 5.2: Diffusion constant ($10^{-5} cm^2/s$) for DOX and GEM for acetylation and butylation at different degree of modification.

However, the contact data presented in Table 5.3 shows that DOX still forms a large number of contacts with the chitosan network. Going from 16% to 32% butylation,

	DOX		GEM	
	Evenly-spaced	**Blocky**	**Evenly-spaced**	**Blocky**
Modification	Avg. Contacts	Avg. Contacts	Avg. Contacts	Avg. Contacts
16% Acetylation	27 ± 3	52 ± 4	6 ± 2	7 ± 3
50% Acetylation	83 ± 5	98 ± 5	18 ± 4	21 ± 5
16% Butylation	50 ± 5	96 ± 19	7 ± 3	34 ± 8
32% Butylation	89 ± 9	124 ± 10	58 ± 10	80 ± 18

Table 5.3: Average number of contacts for DOX and GEM for acetylation and butylation at different degree of modification.

especially the number of interactions with the polymer backbone increases, following same trends as shown by the low drug concentration diffusion trends. Overall, diffusion trends remain consistent with the previous study[21] . The trends for both the drugs are independent of the drug concentration.

5.5 Simulation of dual drug migration through modified chitosan hydrogels

We finally sought to understand how the combination of multiple drugs affects the molecular interactions and diffusion through the networks for different types and degrees of modification. Such understanding is needed to gain control over the kinetics and molar ratio of release when using synergistic drug combinations. While some in silico models have been developed to simulate the migration of single drugs through polymer hydrogel networks[85,86] models for multiple drugs are much less common. Combining drugs, especially with different physio-chemical properties, in fact, introduces considerable complexity related to drug-drug interactions and their outcome on drug-polymer interactions. The combination of DOX and GEM has been proven to be a highly effective drug regimen. Both are FDA- approved chemotherapeutics and have been studied in a variety of drug delivery vehicles, such as micellar nanoparticles, PDCs, polymersomes, mesoporous silica nanoparticles, and nanostructured lipid carriers[87,88,89,90] .

Following the same procedure as for the single drug, we performed CG simulations of equimolar GEM and DOX migration through the different chitosan networks, and calculated the diffusion constants for both drugs. Notably, the values derived from dual-drug release (Figure 5.11) show rather different trends from those obtained with single

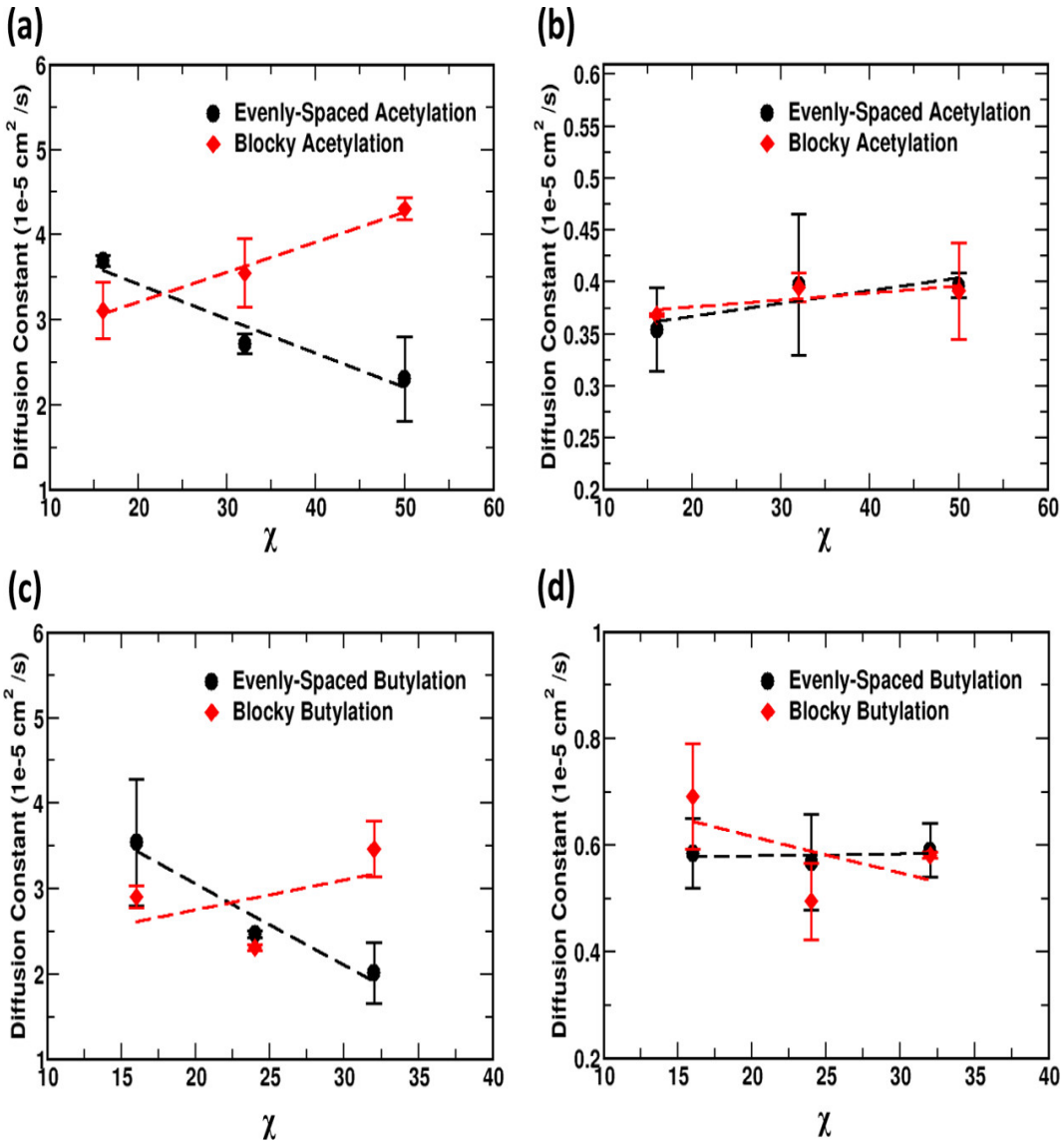

Figure 5.11: Drug diffusion constants vs. χ for dual-drug migration across different chitosan networks: (a) GEM in acetyl-chitosan, (b) DOX in acetyl-chitosan, (c) GEM in butanoyl-chitosan, and (d) DOX in butanoyl-chitosan.

drugs (Figure 5.5). In particular, the diffusion of DOX now remains almost constant across the entire range of χ for both acetyl- and butanoyl-chitosan. The diffusion of GEM is also markedly different. For alternated modification patterns, GEM diffusion decreases with χ through both acetyl- and butanoyl-chitosan. For blocky modification patterns, instead, GEM diffusion increases with χ through acetyl-chitosan and is almost constant with χ through butanoyl-chitosan.

These differences indicate that drug-drug interactions affect significantly their inter-

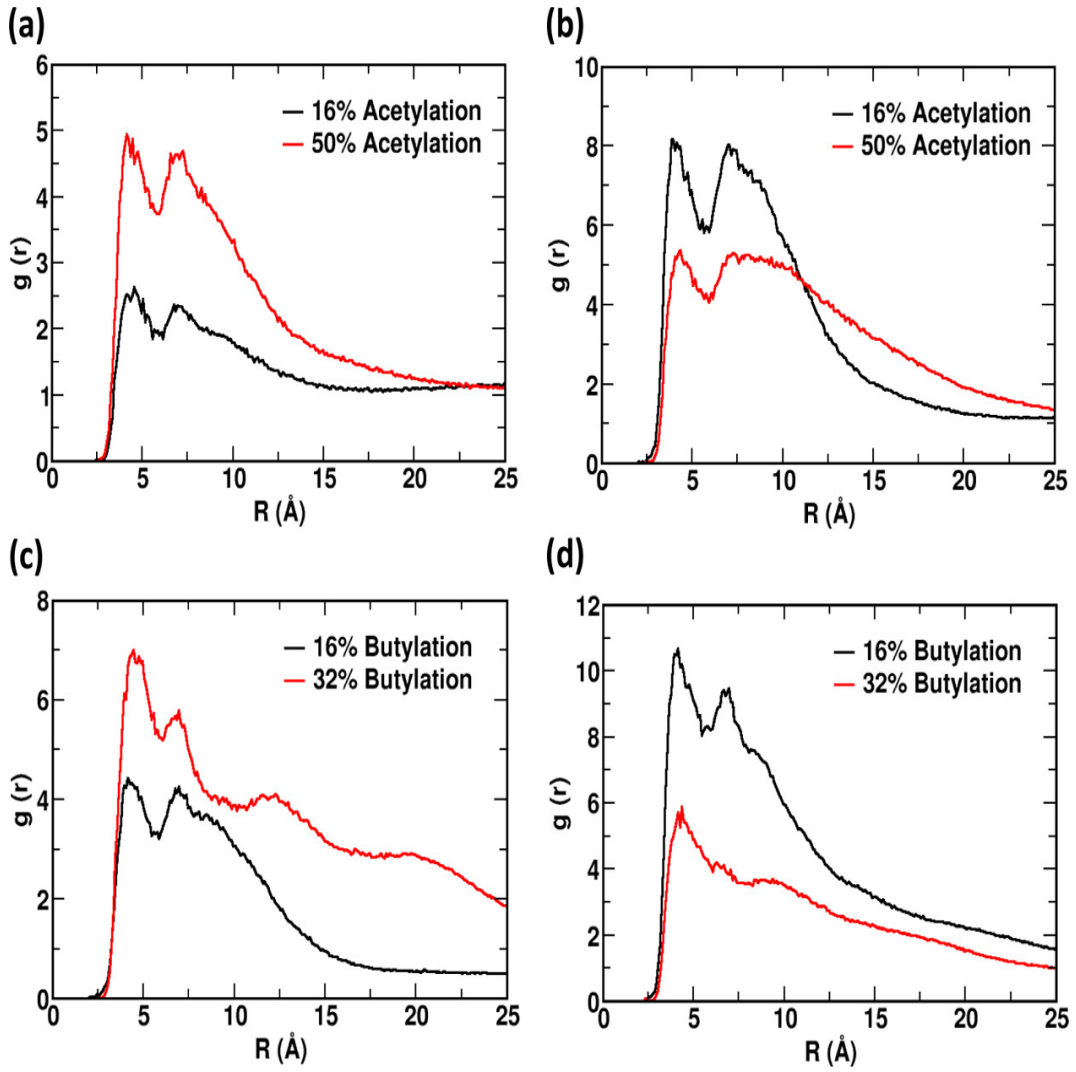

Figure 5.12: Radial distribution functions of GEM around the center of mass of DOX in acetyl-chitosan networks with (a) evenly-spaced and (b) blocky modification, and butanoyl-chitosan networks with (c) evenly-spaced and (d) blocky modification.

actions with the network. This is confirmed by the radial distribution functions of GEM around DOX molecules, which indicate a strong tendency of the two drug molecules to aggregate. As can be seen from the double-peak shape of the curves in Figure 5.12, in fact, clusters of GEM around DOX and values < 1 out to large distances are frequently formed for both modification types, the trends of the drug-drug interaction with increasing χ are reversed for the blocky pattern.

5.6 Conclusion

Hydrogels constructed with native or modified polysaccharides and loaded with chemotherapeutic drugs have been extensively studied, and a conspicuous number of them have entered the clinical pipeline through the last decade[91,92,93,94] A growing segment in this field is represented by polymer conjugates and hydrogels that deliver synergistic combinations of drugs. In developing these systems for a given drug combination, the choice of the modification groups, degree of modification, and initial drug loading are crucial to ensure the therapeutic efficacy of the formulation. Empirical exploration of such wide design space, however, is cumbersome. In this chapter, we have described the development of a computational model that could serve as a powerful guide to pharmaceutical chemists in the identification of the design parameters that afford a schedule and a ratio of drug release that ensure a successful therapeutic outcome. The proposed model has been validated by comparison to experimental data by closely corresponding systems and managed to accurately predict complex phenomena, such as the different microscale morphologies present in hydrogels constructed with different types and degrees of modification, and the migration of not only one, but also two drugs through these modified polymer networks. While focusing on hydrophobically modified chitosan hydrogels and the GEM-DOX drug pair, this method is applicable to other polymer substrates, modification moiety, and therapeutic payload.

Chapter 6

Conclusion

In this thesis, self-assembly of glucose and chitosan-based polysaccharides were studied using atomistic and coarse-grained molecular dynamics simulation. In chapter 2, all-atom simulations showed the effect of linkage, type, and various substitutions on the flexibility of the polymer. The effect of the modification pattern on the molecules flexibility was shown. To study these polymer systems at larger length and time scales, coarse-grained models for each molecules were developed. The CG models were used to study polymer aggregation for cellulose and chitosan based oligomers. The CG model was able to predict fibril formation for cellulose and chitin. For methylated and fluorinated cellulose molecules, vastly different structures were observed, depending on the pattern of modification. Whereas for methylated cellulose with alternate pattern and fluorinated cellulose with blockwise pattern showed polymer aggregation in water while, methylated cellulose with blockwise pattern and fluorinated cellulose with alternate pattern were soluble in water. These results were verified experimentally and could be explained based on the changed flexibility of the molecules and interactions of the modifications.

In chapter 3, a CG force-field was developed. The transferability of the obtained model corresponding to the degree of polymerization, degree of modification, and different solute concentrations were demonstrated. Chapter 5 showed the diffusion of two anti-cancer drugs namely DOX and GEM through the different networks. GEM diffuses through the polymer networks similarly as through water. Its diffusion is independent of the type and degree of modification. In the case of DOX, however opposing diffusion trends with respect to the degree of modification are found for acetyl and butyl. Finally, simulation with both types of drug showed different irregular diffusion trends as com-

pared to the single drug diffusion trends. Overall, the proposed combination of all-atom and CG simulation as used here has demonstrated good predictive power and represents a reliable and predictive toolbox for understanding and predicting the properties of carbohydrate aggregates, as can be used for example in pharmaceutical applications.

List of Figures

List of Tables

Bibliography

[1] Lois M Crowe, Robert Mouradian, John H Crowe, Susan A Jackson, and Christopher Womersley. Effects of carbohydrates on membrane stability at low water activities. *Biochimica et Biophysica Acta (BBA)-Biomembranes*, 769(1):141–150, 1984.

[2] R James Stubbs, AM Prentice, and WP James. Carbohydrates and energy balance. *Annals of the New York Academy of Sciences*, 819:44–69, 1997.

[3] Max Kleiber et al. The fire of life. an introduction to animal energetics. *The fire of life. An introduction to animal energetics.*, 1961.

[4] Paul R Crocker and Ten Feizi. Carbohydrate recognition systems: functional triads in cell—cell interactions. *Current opinion in structural biology*, 6(5):679–691, 1996.

[5] Akiko Takada, Katsuyuki Ohmori, Naofumi Takahashi, Kiyotaka Tsuyuoka, Akihiro Yago, Koichi Zenita, Akira Hasegawa, and Reiji Kannagi. Adhesion of human cancer cells to vascular endothelium mediated by a carbohydrate antigen, sialyl lewis a. *Biochemical and biophysical research communications*, 179(2):713–719, 1991.

[6] Klaus N Englyst and Hans N Englyst. Carbohydrate bioavailability. *British Journal of Nutrition*, 94(1):1–11, 2005.

[7] Artur Cavaco-Paulo. Mechanism of cellulase action in textile processes. *Carbohydrate Polymers*, 37(3):273–277, 1998.

[8] Zhijun Shi, Yue Zhang, Glyn O Phillips, and Guang Yang. Utilization of bacterial cellulose in food. *Food hydrocolloids*, 35:539–545, 2014.

[9] Robert L Barcus and David W Bjorkquist. Fibers and pulps for papermaking based on chemical combination of poly (acrylate-co-itaconate), polyol and cellulosic fiber, November 3 1992. US Patent 5,160,789.

[10] Hongli Zhu, Wei Luo, Peter N Ciesielski, Zhiqiang Fang, JY Zhu, Gunnar Henriksson, Michael E Himmel, and Liangbing Hu. Wood-derived materials for green electronics, biological devices, and energy applications. *Chemical Reviews*, 116(16):9305–9374, 2016.

[11] Yang Yu, Theodore Tyrikos-Ergas, Yuntao Zhu, Giulio Fittolani, Vittorio Bordoni, Ankush Singhal, Richard J Fair, Andrea Grafmüller, Peter H Seeberger, and Martina Delbianco. Systematic hydrogen-bond manipulations to establish polysaccharide structure–property correlations. *Angewandte Chemie*, 131(37):13261–13266, 2019.

[12] Stephen C Fry. The structure and functions of xyloglucan. *Journal of Experimental Botany*, 40(1):1–11, 1989.

[13] Hale Cigdem Arca, Laura I Mosquera-Giraldo, Vivian Bi, Daiqiang Xu, Lynne S Taylor, and Kevin J Edgar. Pharmaceutical applications of cellulose ethers and cellulose ether esters. *Biomacromolecules*, 19(7):2351–2376, 2018.

[14] Per M Claesson and Barry W Ninham. ph-dependent interactions between adsorbed chitosan layers. *Langmuir*, 8(5):1406–1412, 1992.

[15] Levan Tsereteli and Andrea Grafmüller. An accurate coarse-grained model for chitosan polysaccharides in aqueous solution. *PloS one*, 12(7):e0180938, 2017.

[16] Claire Chatelet, Odile Damour, and Alain Domard. Influence of the degree of acetylation on some biological properties of chitosan films. *Biomaterials*, 22(3):261–268, 2001.

[17] Steven W Benner, Vijay T John, and Carol K Hall. Simulation study of hydrophobically modified chitosan as an oil dispersant additive. *The Journal of Physical Chemistry B*, 119(23):6979–6990, 2015.

[18] Yunqiang Chen, Libin Chen, Hua Bai, and Lei Li. Graphene oxide–chitosan composite hydrogels as broad-spectrum adsorbents for water purification. *Journal of Materials Chemistry A*, 1(6):1992–2001, 2013.

[19] Hiroshi Ueno, Takashi Mori, and Toru Fujinaga. Topical formulations and wound healing applications of chitosan. *Advanced drug delivery reviews*, 52(2):105–115, 2001.

[20] Narayan Bhattarai, Jonathan Gunn, and Miqin Zhang. Chitosan-based hydrogels for controlled, localized drug delivery. *Advanced drug delivery reviews*, 62(1):83–99, 2010.

[21] John D Schneible, Ankush Singhal, Radina L Lilova, Carol K Hall, Andrea Grafmuller, and Stefano Menegatti. Tailoring the chemical modification of chitosan hydrogels to fine-tune the release of a synergistic combination of chemotherapeutics. *Biomacromolecules*, 20(8):3126–3141, 2019.

[22] Todd R Hoare and Daniel S Kohane. Hydrogels in drug delivery: Progress and challenges. *Polymer*, 49(8):1993–2007, 2008.

[23] Yong Qiu and Kinam Park. Environment-sensitive hydrogels for drug delivery. *Advanced drug delivery reviews*, 53(3):321–339, 2001.

[24] Paul Tangney and Sandro Scandolo. An ab initio parametrized interatomic force field for silica. *The Journal of chemical physics*, 117(19):8898–8904, 2002.

[25] Luca Monticelli, Senthil K Kandasamy, Xavier Periole, Ronald G Larson, D Peter Tieleman, and Siewert-Jan Marrink. The martini coarse-grained force field: extension to proteins. *Journal of chemical theory and computation*, 4(5):819–834, 2008.

[26] Karl N Kirschner, Austin B Yongye, Sarah M Tschampel, Jorge González-Outeiriño, Charlisa R Daniels, B Lachele Foley, and Robert J Woods. Glycam06: a generalizable biomolecular force field. carbohydrates. *Journal of computational chemistry*, 29(4):622–655, 2008.

[27] Jörg Sauter and Andrea Grafmüller. Procedure for transferable coarse-grained models of aqueous polysaccharides. *Journal of chemical theory and computation*, 13(1):223–236, 2016.

[28] Martin Lısal, Jiřı Kolafa, and Ivo Nezbeda. An examination of the five-site potential (tip5p) for water. *The Journal of chemical physics*, 117(19):8892–8897, 2002.

[29] Jorg Sauter and Andrea Grafmuller. Solution properties of hemicellulose polysaccharides with four common carbohydrate force fields. *Journal of chemical theory and computation*, 11(4):1765–1774, 2015.

[30] Sergei Izvekov and Gregory A Voth. A multiscale coarse-graining method for biomolecular systems. *The Journal of Physical Chemistry B*, 109(7):2469–2473, 2005.

[31] Dirk Reith, Mathias Pütz, and Florian Müller-Plathe. Deriving effective mesoscale potentials from atomistic simulations. *Journal of computational chemistry*, 24(13):1624–1636, 2003.

[32] William George Noid, Jhih-Wei Chu, Gary S Ayton, Vinod Krishna, Sergei Izvekov, Gregory A Voth, Avisek Das, and Hans C Andersen. The multiscale coarse-graining method. i. a rigorous bridge between atomistic and coarse-grained models. *The Journal of chemical physics*, 128(24):244114, 2008.

[33] Siewert J Marrink, Alex H De Vries, and Alan E Mark. Coarse grained model for semiquantitative lipid simulations. *The Journal of Physical Chemistry B*, 108(2):750–760, 2004.

[34] Mark Bathe, Gregory C Rutledge, Alan J Grodzinsky, and Bruce Tidor. A coarse-grained molecular model for glycosaminoglycans: application to chondroitin, chondroitin sulfate, and hyaluronic acid. *Biophysical journal*, 88(6):3870–3887, 2005.

[35] Karim Mazeau, Serge Pérez, and Marguerite Rinaudo. Predicted influence of n-acetyl group content on the conformational extension of chitin and chitosan chains. 2000.

[36] Pu Liu, Sergei Izvekov, and Gregory A Voth. Multiscale coarse-graining of monosaccharides. *The Journal of Physical Chemistry B*, 111(39):11566–11575, 2007.

[37] Jörg Sauter and Andrea Grafmüller. Efficient osmotic pressure calculations using coarse-grained molecular simulations. *Journal of chemical theory and computation*, 14(3):1171–1176, 2018.

[38] Steven W Benner and Carol K Hall. Development of a coarse-grained model of chitosan for predicting solution behavior. *The Journal of Physical Chemistry B*, 120(29):7253–7264, 2016.

[39] Peter H Seeberger. The logic of automated glycan assembly. *Accounts of chemical research*, 48(5):1450–1463, 2015.

[40] Oliviana Calin, Steffen Eller, and Peter H Seeberger. Automated polysaccharide synthesis: assembly of a 30mer mannoside. *Angewandte Chemie International Edition*, 52(22):5862–5865, 2013.

[41] MJ Abraham, D van der Spoel, E Lindahl, and B Hess. Gromacs user manual, version 5.1. 2; gromacs development team, 2016. *There is no corresponding record for this reference.*

[42] DA Case, TA Darden, TE Cheatham III, CL Simmerling, J Wang, RE Duke, R Luo, RC Walker, W Zhang, KM Merz, et al. Amber 12; university of california: San

francisco, 2012. *There is no corresponding record for this reference*, pages 1–826, 2010.

[43] Eric J Sorin and Vijay S Pande. Exploring the helix-coil transition via all-atom equilibrium ensemble simulations. *Biophysical journal*, 88(4):2472–2493, 2005.

[44] Marko Wehle, Ivan Vilotijevic, Reinhard Lipowsky, Peter H Seeberger, Daniel Varon Silva, and Mark Santer. Mechanical compressibility of the glycosylphosphatidylinositol (gpi) anchor backbone governed by independent glycosidic linkages. *Journal of the American Chemical Society*, 134(46):18964–18972, 2012.

[45] Sander Pronk, Szilárd Páll, Roland Schulz, Per Larsson, Pär Bjelkmar, Rossen Apostolov, Michael R Shirts, Jeremy C Smith, Peter M Kasson, David Van Der Spoel, et al. Gromacs 4.5: a high-throughput and highly parallel open source molecular simulation toolkit. *Bioinformatics*, 29(7):845–854, 2013.

[46] Junmei Wang, Romain M Wolf, James W Caldwell, Peter A Kollman, and David A Case. Development and testing of a general amber force field. *Journal of computational chemistry*, 25(9):1157–1174, 2004.

[47] Christopher I Bayly, Piotr Cieplak, Wendy Cornell, and Peter A Kollman. A well-behaved electrostatic potential based method using charge restraints for deriving atomic charges: the resp model. *The Journal of Physical Chemistry*, 97(40):10269–10280, 1993.

[48] Tom Darden, Darrin York, and Lee Pedersen. Particle mesh ewald: An n log (n) method for ewald sums in large systems. *The Journal of chemical physics*, 98(12):10089–10092, 1993.

[49] Berk Hess, Henk Bekker, Herman JC Berendsen, and Johannes GEM Fraaije. Lincs: a linear constraint solver for molecular simulations. *Journal of computational chemistry*, 18(12):1463–1472, 1997.

[50] Shuichi Miyamoto and Peter A Kollman. Settle: An analytical version of the shake and rattle algorithm for rigid water models. *Journal of computational chemistry*, 13(8):952–962, 1992.

[51] Shuichi Nosé. S. nosé, j. chem. phys. 81, 511 (1984). *J. Chem. Phys.*, 81:511, 1984.

[52] William G Hoover. Canonical dynamics: Equilibrium phase-space distributions. *Physical review A*, 31(3):1695, 1985.

[53] Michele Parrinello and Aneesur Rahman. Polymorphic transitions in single crystals: A new molecular dynamics method. *Journal of Applied physics*, 52(12):7182–7190, 1981.

[54] Shuichi Nosé and ML Klein. Constant pressure molecular dynamics for molecular systems. *Molecular Physics*, 50(5):1055–1076, 1983.

[55] Ilario G Tironi, René Sperb, Paul E Smith, and Wilfred F van Gunsteren. A generalized reaction field method for molecular dynamics simulations. *The Journal of chemical physics*, 102(13):5451–5459, 1995.

[56] Wilfred F Van Gunsteren and Herman JC Berendsen. A leap-frog algorithm for stochastic dynamics. *Molecular Simulation*, 1(3):173–185, 1988.

[57] Supriyo Bhattacharya and Keith E Gubbins. Fast method for computing pore size distributions of model materials. *Langmuir*, 22(18):7726–7731, 2006.

[58] Franz Kappel and Alexei V Kuntsevich. An implementation of shor's r-algorithm. *Computational Optimization and Applications*, 15(2):193–205, 2000.

[59] Victor Ruhle, Christoph Junghans, Alexander Lukyanov, Kurt Kremer, and Denis Andrienko. Versatile object-oriented toolkit for coarse-graining applications. *Journal of chemical theory and computation*, 5(12):3211–3223, 2009.

[60] SY Mashayak, Mara N Jochum, Konstantin Koschke, Narayana R Aluru, Victor Rühle, and Christoph Junghans. Relative entropy and optimization-driven coarse-graining methods in votca. *PLoS one*, 10(7):e0131754, 2015.

[61] Gregg T Beckham and Michael F Crowley. Examination of the α-chitin structure and decrystallization thermodynamics at the nanoscale. *The Journal of Physical Chemistry B*, 115(15):4516–4522, 2011.

[62] Eduardo F Franca, Roberto D Lins, Luiz CG Freitas, and TP Straatsma. Characterization of chitin and chitosan molecular structure in aqueous solution. *Journal of Chemical Theory and Computation*, 4(12):2141–2149, 2008.

[63] Wesley K Lay, Mark S Miller, and Adrian H Elcock. Optimizing solute–solute interactions in the glycam06 and charmm36 carbohydrate force fields using osmotic pressure measurements. *Journal of chemical theory and computation*, 12(4):1401–1407, 2016.

[64] Jodi A Hadden, Alfred D French, and Robert J Woods. Unraveling cellulose microfibrils: a twisted tale. *Biopolymers*, 99(10):746–756, 2013.

[65] Liming Hu, Yun Sun, and Yan Wu. Advances in chitosan-based drug delivery vehicles. *Nanoscale*, 5(8):3103–3111, 2013.

[66] Raphaël Riva, Heloise Ragelle, Anne des Rieux, Nicolas Duhem, Christine Jérôme, and Véronique Préat. Chitosan and chitosan derivatives in drug delivery and tissue engineering. In *Chitosan for biomaterials II*, pages 19–44. Springer, 2011.

[67] Mokhamad Nur and Todor Vasiljevic. Can natural polymers assist in delivering insulin orally? *International journal of biological macromolecules*, 103:889–901, 2017.

[68] Seong-Chul Hong, Seung-Yup Yoo, Hyeongmin Kim, and Jaehwi Lee. Chitosan-based multifunctional platforms for local delivery of therapeutics. *Marine drugs*, 15(3):60, 2017.

[69] PL Lam and Roberto Gambari. Advanced progress of microencapsulation technologies: In vivo and in vitro models for studying oral and transdermal drug deliveries. *Journal of controlled release*, 178:25–45, 2014.

[70] Jorg Sauter and Andrea Grafmuller. Predicting the chemical potential and osmotic pressure of polysaccharide solutions by molecular simulations. *Journal of chemical theory and computation*, 12(9):4375–4384, 2016.

[71] Ornella Ortona, Gerardino D'Errico, Gaetano Mangiapia, and Donato Ciccarelli. The aggregative behavior of hydrophobically modified chitosans with high substitution degree in aqueous solution. *Carbohydrate polymers*, 74(1):16–22, 2008.

[72] Gang-Biao Jiang, Daping Quan, Kairong Liao, and Haihua Wang. Preparation of polymeric micelles based on chitosan bearing a small amount of highly hydrophobic groups. *Carbohydrate Polymers*, 66(4):514–520, 2006.

[73] M Rinaudo, R Auzely, C Vallin, and I Mullagaliev. Specific interactions in modified chitosan systems. *Biomacromolecules*, 6(5):2396–2407, 2005.

[74] Sei-ichi Aiba. Studies on chitosan: 3. evidence for the presence of random and block copolymer structures in partially n-acetylated chitosans. *International journal of biological macromolecules*, 13(1):40–44, 1991.

[75] Keisuke Kurita, Takanori Sannan, and Yoshio Iwakura. Studies on chitin, 4. evidence for formation of block and random copolymers of n-acetyl-d-glucosamine and d-glucosamine by hetero-and homogeneous hydrolyses. *Die Makromolekulare Chemie: Macromolecular Chemistry and Physics*, 178(12):3197–3202, 1977.

[76] Mette H Ottey, Kjell M Vårum, and Olav Smidsrød. Compositional heterogeneity of heterogeneously deacetylated chitosans. *Carbohydrate Polymers*, 29(1):17–24, 1996.

[77] Jérôme Berger, Marianne Reist, Joachim M Mayer, Olivia Felt, NA Peppas, and Robert Gurny. Structure and interactions in covalently and ionically crosslinked chitosan hydrogels for biomedical applications. *European Journal of Pharmaceutics and Biopharmaceutics*, 57(1):19–34, 2004.

[78] Simon M Iveson, James D Litster, Karen Hapgood, and Bryan J Ennis. Nucleation, growth and breakage phenomena in agitated wet granulation processes: a review. *Powder technology*, 117(1-2):3–39, 2001.

[79] Min Mu, Xiaoling Li, Aiping Tong, and Gang Guo. Multi-functional chitosan-based smart hydrogels mediated biomedical application. *Expert opinion on drug delivery*, 16(3):239–250, 2019.

[80] Michelly CG Pellá, Michele K Lima-Tenório, Ernandes T Tenório-Neto, Marcos R Guilherme, Edvani C Muniz, and Adley F Rubira. Chitosan-based hydrogels: From preparation to biomedical applications. *Carbohydrate Polymers*, 196:233–245, 2018.

[81] Ecaterina Stela Dragan and Maria Valentina Dinu. Polysaccharides constructed hydrogels as vehicles for proteins and peptides. a review. *Carbohydrate polymers*, page 115210, 2019.

[82] Michael W Mahoney and William L Jorgensen. Diffusion constant of the tip5p model of liquid water. *The Journal of Chemical Physics*, 114(1):363–366, 2001.

[83] Marco Biondi, Sabato Fusco, Andrew L Lewis, and Paolo A Netti. New insights into the mechanisms of the interactions between doxorubicin and the ion-exchange hydrogel

dc bead^{TM} for use in transarterial chemoembolization (tace). *Journal of Biomaterials Science, Polymer Edition*, 23(1-4):333–354, 2012.

[84] Cary T Chiou, David W Schmedding, and Milton Manes. Partitioning of organic compounds in octanol-water systems. *Environmental Science & Technology*, 16(1):4–10, 1982.

[85] Suvakanta Dash, Padala Narasimha Murthy, Lilakanta Nath, Prasanta Chowdhury, et al. Kinetic modeling on drug release from controlled drug delivery systems. *Acta Pol Pharm*, 67(3):217–23, 2010.

[86] T Higuchi. Mechanism of sustained-action medication. theoretical analysis of rate of release of solid drugs dispersed in solid matrices. *Journal of pharmaceutical sciences*, 52(12):1145–1149, 1963.

[87] Kathryn M Camacho, Stefano Menegatti, Douglas R Vogus, Anusha Pusuluri, Zoë Fuchs, Maria Jarvis, Michael Zakrewsky, Michael A Evans, Renwei Chen, and Samir Mitragotri. Dafodil: a novel liposome-encapsulated synergistic combination of doxorubicin and 5fu for low dose chemotherapy. *Journal of Controlled Release*, 229:154–162, 2016.

[88] Dechun Liu, Yanbin Chen, Xiaoshan Feng, Miao Deng, Gangqiang Xie, Jianguang Wang, Like Zhang, Qipeng Liu, and Pengfei Yuan. Micellar nanoparticles loaded with gemcitabine and doxorubicin showed synergistic effect. *Colloids and Surfaces B: Biointerfaces*, 113:158–168, 2014.

[89] Twan Lammers, Vladimir Subr, Karel Ulbrich, Peter Peschke, Peter E Huber, Wim E Hennink, and Gert Storm. Simultaneous delivery of doxorubicin and gemcitabine to tumors in vivo using prototypic polymeric drug carriers. *Biomaterials*, 30(20):3466–3475, 2009.

[90] Shuqin Ni, Lei Qiu, Guodong Zhang, Haiyan Zhou, and Yong Han. Lymph cancer chemotherapy: delivery of doxorubicin–gemcitabine prodrug and vincristine by nanostructured lipid carriers. *International journal of nanomedicine*, 12:1565, 2017.

[91] Sonke Svenson, Marc Wolfgang, Jungyeon Hwang, John Ryan, and Scott Eliasof. Preclinical to clinical development of the novel camptothecin nanopharmaceutical crlx101. *Journal of controlled release*, 153(1):49–55, 2011.

[92] Thomas Schluep, Jungyeon Hwang, Isabel J Hildebrandt, Johannes Czernin, Chung Hang J Choi, Christopher A Alabi, Brendan C Mack, and Mark E Davis. Pharmacokinetics and tumor dynamics of the nanoparticle it-101 from pet imaging and tumor histological measurements. *Proceedings of the National Academy of Sciences*, 106(27):11394–11399, 2009.

[93] Glen J Weiss, Joseph Chao, Jeffrey D Neidhart, Ramesh K Ramanathan, Dawn Bassett, James A Neidhart, Chung Hang J Choi, Warren Chow, Vincent Chung, Stephen J Forman, et al. First-in-human phase 1/2a trial of crlx101, a cyclodextrin-containing polymer-camptothecin nanopharmaceutical in patients with advanced solid tumor malignancies. *Investigational new drugs*, 31(4):986–1000, 2013.

[94] Andrew J Clark, Devin T Wiley, Jonathan E Zuckerman, Paul Webster, Joseph Chao, James Lin, Yun Yen, and Mark E Davis. Crlx101 nanoparticles localize in human tumors and not in adjacent, nonneoplastic tissue after intravenous dosing. *Proceedings of the National Academy of Sciences*, 113(14):3850–3854, 2016.